Analysis of the rare decay B0 ->K*0 e+e- at LHCb

M. Nicol

LAL 12-436
5 December 2012

Université Paris-Sud 11

Ecole Doctorale Particules, Noyaux et Cosmos- ED 517
Laboratoire de l'Accélérateur Linéaire - UMR 8607

Discipline : Physique des particules

THÈSE DE DOCTORAT

preséntée par

Michelle NICOL

Analysis of the rare decay $B^0 \to K^{*0} e^+ e^-$ at LHCb

Analyse de la désintégration rare $B^0 \to K^{*0} e^+ e^-$ dans l'expérience LHCb

Soutenue le 5 december 2012 devant le Jury composé de :

M.	D. Bečirević	Examinateur
M.	O. Deschamps	Rapporteur
M.	U. Egede	Examinateur
Mme.	M.-H. Schune	Directrice de thèse
M.	A. Stocchi	Examinateur
M.	P. Urquijo	Rapporteur

Dedicated to my mother,
and written in memory of
Simon McKernan (1986-2008)
and Adriaan Mulder (1990-2012).

Contents

Résumé

Grâce à la grande section efficace de production de paires $b\bar{b}$, LHC offre une excellente occasion de faire des études de courants neutre changeant la saveur. Ces transitions sont sensibles aux effets de nouvelle physique. Cette thèse porte sur l'analyse des événements $B^0 \to K^{*0}e^+e^-$ qui permettent de mesurer la fraction de photon avec une polarisation droite et donc de rechercher des signaux de nouvelle physique émis dans la transition $b \to s\gamma$. En effet, dans le Modèle Standard, la polarisation des photons est gauche. La paire e^+e^-, lors que la masse invariante de la paire de leptons est basse, provient d'un photon virtuel et permet donc de sonder la polarisation de celui-ci. Cette mesure se fait grâce à l'étude des distribution angulaires de cette désintégration á quatre corps.

Une première ètape est la mesure du rapport d'embranchement dans le domaine de masse 30-1000 MeV/c^2. En effet, cette désintégration n'a jamais été observée dans cette région, y compris auprès des usines à B à cause du très faible rapport d'embranchement.

Cette analyse comportant des électrons de basse impulsion transverse est expérimentalement complexe dans un environnement tel que celui du LHC. La mesure est faite relativement au rapport d'embranchement de la désintégration $B^0 \to J/\psi(e^+e^-)K^{*0}$. En effet, cela permet de s'affranchir de nombreux effets expérimentaux ainsi que de la détermination absolue des efficacités.

Le résultat, repose sur les données collectées par LHCb en 2011 et correspondant à une luminosité intégrée de 1 fb^{-1}:

$$\mathcal{B}(B^0 \to K^{*0}e^+e^-)^{30-1000\,\mathrm{MeV}/c^2} = (3.19^{+0.75}_{-0.68}(\mathrm{stat}) \pm 0.22(\mathrm{syst}) \pm 0.15(\mathrm{PDG})) \times 10^{-7}$$

en utilisant la valeur PDG pour le rapport d'embranchement de la désintégration $B^0 \to J/\psi(e^+e^-)K^{*0}$.

La dernière partie de la thèse porte sur des études Monte Carlo qui montrent

que la précision sur la fraction de photon avec une polarisation droite que l'on peut espérer obtenir avec l'inclusion des données de 2012 est d'environ 0.1, comparable à la moyenne mondiale obtenue avec des méthodes différentes.

Mots clés: Physique des particules, Grand Collisionneur de Hadrons, LHC, LHCb, désintégration de méson-B, polarisation de photon, pingouin electrofaible, Modéle Standard, courant neutre changeant la saveur.

Abstract

The high $b\bar{b}$ cross section produced by the LHC offers an excellent opportunity for the study of flavour changing neutral current B decays, where the effects of new physics can be probed. This thesis presents an analysis of the rare decay $B^0 \to K^{*0}e^+e^-$, which can be used to measure the polarisation of the photon in the $b \to s\gamma$ transition. When the dilepton mass is low, the e^+e^- pair comes predominantly from a virtual photon, and the polarisation can be accessed via an angular analysis. It is predicted to be predominantly left handed in the Standard Model, and therefore an enhanced right handed amplitude would be a sign of new physics.

A first step is to measure the branching fraction in the dilepton mass range, 30 MeV/c^2 to 1 GeV. This decay has not yet been observed in this region, due to its small branching ratio.

The analysis involves electrons with low transverse momentum, and is thus experimentally complex in the hadronic environment at the LHC. The branching ratio is measured relative to that of $B^0 \to J/\psi\,(e^+e^-)K^{*0}$, which eliminates both certain experimental effects, and the need to determine absolute efficiencies.

The result is obtained with an integrated luminosity of 1 fb^{-1} of pp collisions, collected by LHCb during 2011 and is found to be:

$$\mathcal{B}(B^0 \to K^{*0}e^+e^-)^{30-1000\,\mathrm{MeV}/c^2} = (3.19^{+0.75}_{-0.68}(\mathrm{stat}) \pm 0.21(\mathrm{syst}) \pm 0.15(\mathrm{PDG})) \times 10^{-7}$$

when using the PDG value for the $B^0 \to J/\psi\,(e^+e^-)K^{*0}$ branching ratio.

The last part of the thesis presents Monte Carlo studies, showing that with the inclusion of the 2012 data sample, the expected sensitivity on the fraction of right handed polarisation is approximately 0.1, which is comparable with the world average obtained with different methods.

Key words: Particle physics, Large Hadron Collider, LHC, LHCb, B decays, photon polarisation, electroweak penguin, Standard Model, flavour changing neutral current.

Synthèse

Introduction

Le Modèle Standard (MS) de la physique des particules décrit les constituants fondamentaux de la matière (Fig. 1.) Il permet d'expliquer les résultats d'un grand

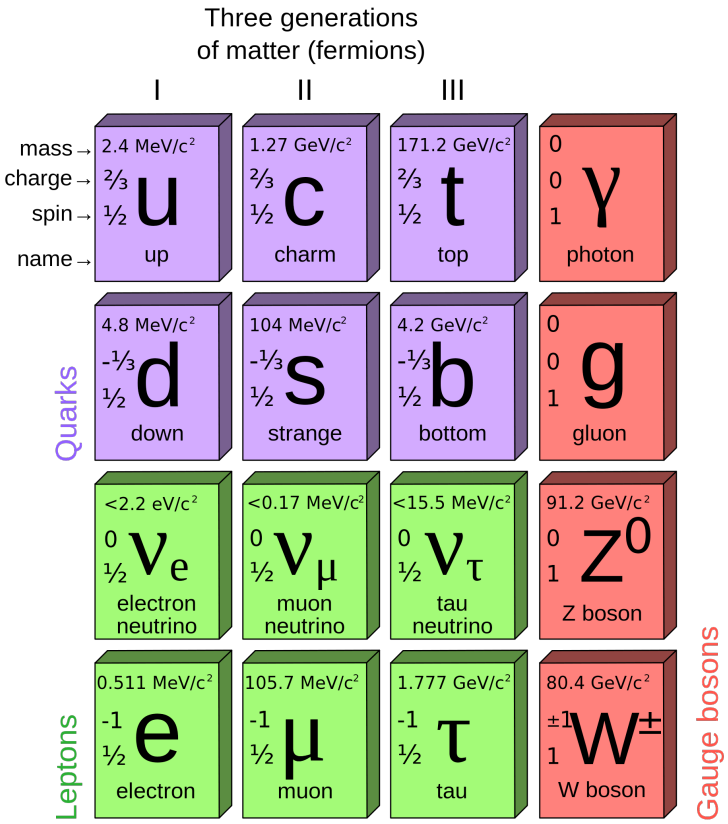

Figure 1: Des particules fondamentales du MS, rangés selon la generation et leur masse. Le boson de Higgs, recemment observé mais dont la caractère standard n'est pas encore confirmé, a été omis.)

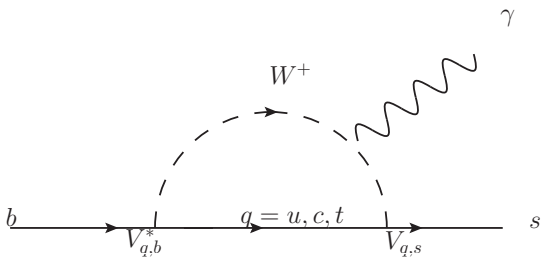

Figure 2: Diagramme en boucle de la transition $b \to s\gamma$.

nombre d'expériences, surtout dans le secteur électrofaible, et ainsi de faire des prédictions. Malgré son succès, un certain nombre de questions restent ouverts. Par exemple, il ne comprend que trois des quatre forces fondamentales, n'offrant pas de description de la gravité. Il n'explique pas également, la grande asymétrie entre matière et anti-matière dans notre univers, la nature de la matière noire, et il possède 19 paramètres libres, un grand nombre pour une théorie fondamentale. Pour ces raisons, entre autres, on pense qu'il existe une Nouvelle Physique (NP), qui se manifesterait à haut énergie.

Le LHC a été construit pour tester le SM et rechercher des signes de NP. Le démarrage du LHC a marqué le début des recherches à une luminosité instantanée et une énergie dans le centre de masse, sans précédent. Cela permet des recherches directes de nouvelles particules, tel que réalisé par ATLAS et CMS, ainsi que des recherches indirectes en recherchant les effets de NP dans les désintégrations de hadrons beaux ou charmés. Le détecteur LHCb suit cette approche. Le programme d'étude des désintégrations rare à LHCb se concentre principalement sur l'analyse des courants neutres changeant la saveur. Ces désintégrations sont fortement supprimées dans le MS, car elles sont interdites au niveau de l'arbre, et procédent uniquement par des diagrammes d'ordre supérieur. Donc, elles sont sensibles aux effets de nouvelle physique, car des nouvelles particules massives peuvent participer aux boucles virtuelles. $b \to s\gamma$ est un courant neutre changeant la saveur (voir Fig. 2), et en particulier, la polarisation du photon virtuel dans cette transition est une observable sensible aux effets de NP, le MS prédisant une hélicité très majoritairement gauche. On peut mesurer la fraction de photon avec une polarisation

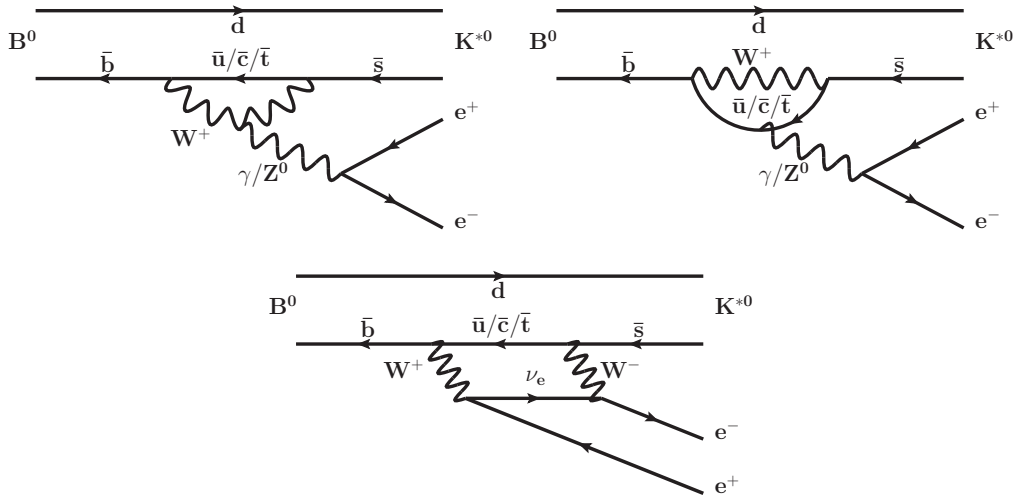

Figure 3: Les diagrammes de Feynman dominants dans ls désintégration $B^0 \to K^{*0}e^+e^-$.

droite par l'analyse des événtements $B^0 \to K^{*0}e^+e^-$. Les diagrammes de Feynman dominants sont illustrés dans la Fig. 3, et la contribution de chacun dépend de la masse invariante de la paire de leptons. Lors que cette masse est basse, la paire e^+e^- provient d'un photon virtuel et permet donc de sonder la polarisation de celui-ci. Cette mesure se fait grâce à l'étude des distributions angulaires de cette désintégration à quatre corps, et en particulier par la mesure de l'angle ϕ, illustré dans la Fig. 4.

Le détecteur LHCb

LHCb est dédiée à l'étude de la violation de CP et à la recherche de désintégrations rares des mésons B. Le mécanisme de production dominant des mésons B dans des collisions proton-proton est la fusion gluon-gluon. À haute énergie, les paires $b\bar{b}$ sont produites dans la même direction, vers l'avant ou vers l'arrière, dans un cône faisant un faible angle avec le faisceau de protons (voir Fig. 5). Par conséquent, le choix naturel de détecteur est un spectromètre à un bras dirigé vers l'avant, avec une couverture angulaire limitée de 10 mrad à 300 mrad pour le plan horizontal et de 10 mrad à 250 mrad pour le plan vertical. Il comprend plusieurs sous-détecteurs, illustrés dans la Fig. 6. Par ordre croissant de z du point d'interaction, ce sont:

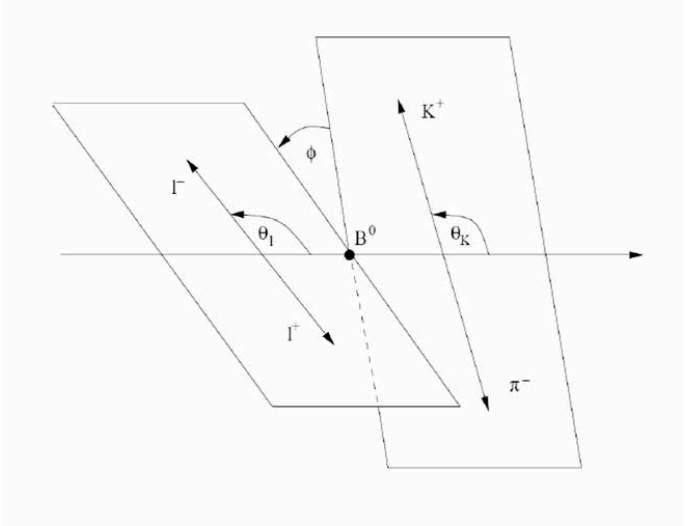

Figure 4: Définition des angles ϕ, θ_K and θ_L dans la désintégration $B \to K^* l^+ l^-$.

- Le Vertex Locater (VELO): le détecteur situé le plus près du faisceau de proton. Il fournit des mesures précises des vertex de production et de désintegration des mésons B et permet donc de les identifier.
- Le détecteur Ring Imaging Cherenkov (RICH1): pour fournir l'identification des particules dont la gamme d'impulsion est comprise entre [1-40] GeV/c.
- Trigger Tracker (TT): un détecteur silicium, fournissant une reconstruction rapide des trajectoires des particules chargées.
- L'aimant:un aimant dipolaire qui fournit un champ magnétique 4Tm.
- Les stations de tracking (T1-T3): détecteurs siliciums situés aprés l'aimant, et qui gèrent la majeure partie de la reconstruction des traces.
- RICH2: pour fournir l'identification des particules dont la gamme d'impulsion est comprise entre [15-100] GeV/c.
- Le système de calorimètres: pour faire la distinction entre des électrons, des photons et des hadrons, et mesurer leur énergie et leur position. Il consiste du Scintillator Pad Detector (SPD), du PreShower (PS), du calorimetre électromagnetique (ECAL) et du colorimetre hadronique (HCAL). Il est un des ingrédients essentiels du trigger de premier niveau.

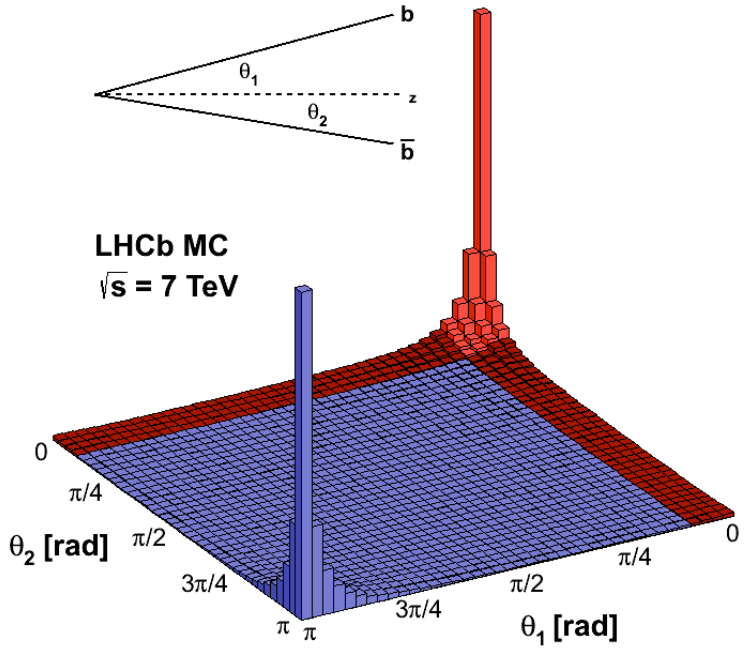

Figure 5: Corrélation entre les quarks b et $\overline{b}$ produites au LHC avec une energie dans le centre de masseénergie, $s = \sqrt{7}$ TeV (géenérée par PYTHIA 8.

- Le détecteur à muons: permet d'identifier une trace comme étant celle d'un muon et constitue l'autre partie dy trigger de premier niveau.

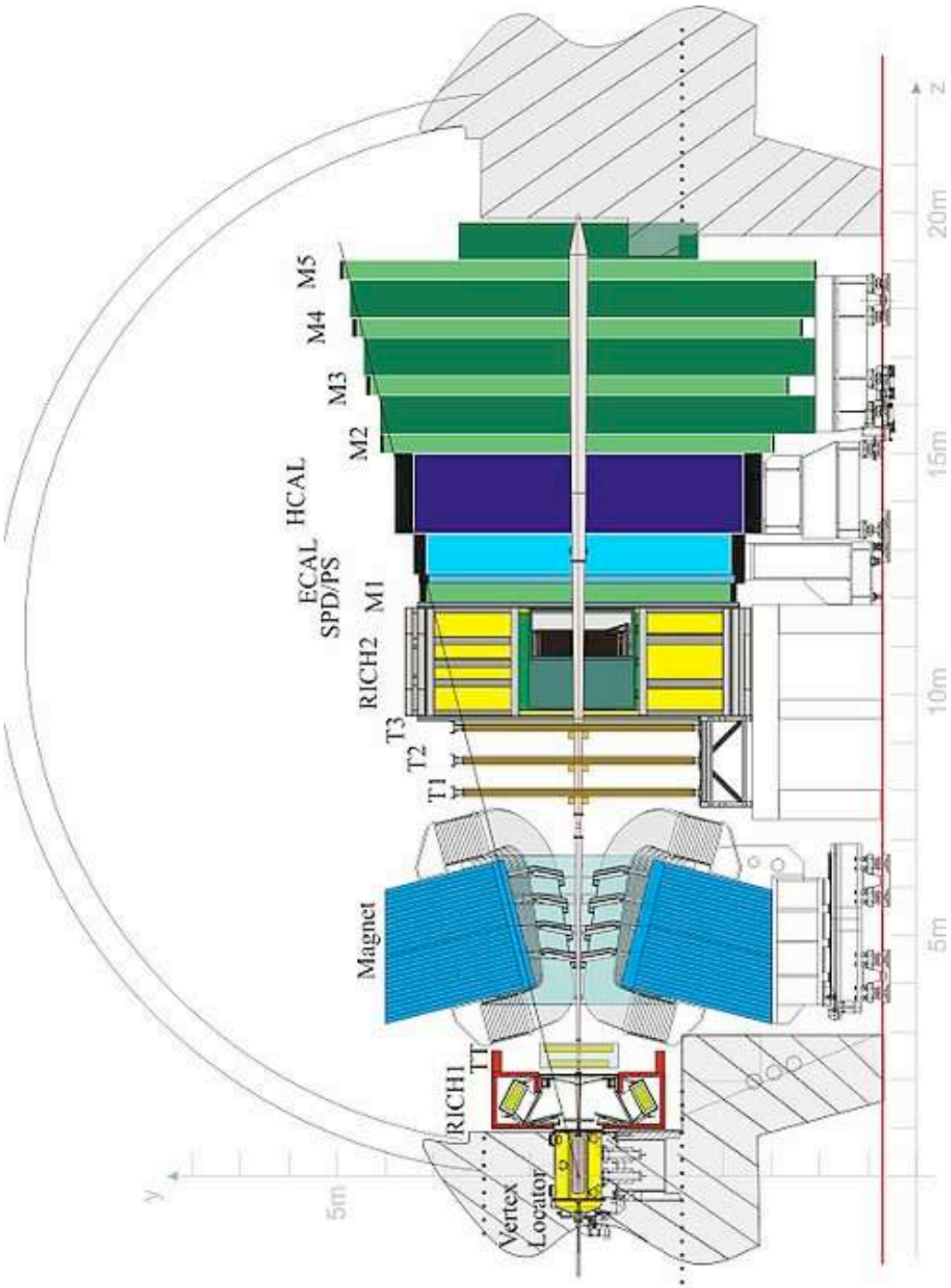

Figure 6: Vue générale du détecteur LHCb.

La mesure du rapport d'embranchement $B^0 \to K^{*0}e^+e^-$

Durant lannée 2011, LHCb a enregistré plus de 90% des collisions délivrées par le LHC, en atteint une luminosité intégrée de 1 fb^{-1}. L'analyse de $B^0 \to K^{*0}e^+e^-$ comportant des electrons de basse impulsion transverse est experimentalement complexe dans un environment tel que celui du LHC. Malgré cela, avec les données collectées par LHCb en 2011, on peut mesurer le rapport d'embranchement dans le domaine de masse 30-1000 MeV/c^2, qui constite une premiére ètape vers l'analyse angulaire. La prédiction théorique dans cette domaine est d'environ:

$$\mathcal{B}_{\text{Vis}}(B^0 \to K^{*0}e^+e^-)^{30-1000\,\text{MeV}/c^2} = 2.9 \times 10^{-7}$$

Cette désintégration n'a jamais été observée dans cette région à cause de ce très faible rapport d'embranchement. L'état des lieux des mesures dans autres domaine de masse faites par les usines à B est résumé dans Table 1.

Experiment	Decay mode	q^2 (GeV^2/c^4)	N_s	$\mathcal{B}(10^{-7})$
BaBar	$B^0 \to K^{*0}\ell^+\ell^-$	total	NA	$10.2^{+1.4}_{-1.3} \pm 0.5$
	$B^0 \to K^{*0}\ell^+\ell^-$	0.10-2.00	$26.0^{+7.1}_{-6.4}$	$1.89^{+0.52}_{-0.46} \pm 0.06$
Belle	$B^0 \to K^{*0}e^+e^-$	total	NA	$11.8^{+2.7}_{-2.2} \pm 0.9$
	$B^0 \to K^{*0}\ell^+\ell^-$	0.00-2.00	$27.4^{+7.4}_{-6.6}$	$1.46^{+0.40}_{-0.35} \pm 0.11$

Table 1: Résumé des resultats des usines à B.

La mesure de cette thèse est faite relativement au rapport d'embranchement de la désintégration $B^0 \to J/\psi\,(e^+e^-)K^{*0}$. En effet, cela permet de s'affranchir de nombreux effets expérimentaux ainsi que de la determination absolute des efficacités.

L'échantillon de données est séparé en trois catégories basées sur les différents voies pertinentes de déclenchement. Le signal est recherché dans chacune des trois catégories en appliquant une sélection serrée construite sur une approche multivariable, qui réduit le bruit de fond combinatoire. Des critères supplémentaires sont developpés pour rejeter des sources de bruits de fond spécifiques. En particulier, la contamination du signal due aux désintégrations radiatives $B^0 \to K^{*0}\gamma$ où le photon réel se matérialise en paire e^+e^- est fortement réduite en utilisant des critères

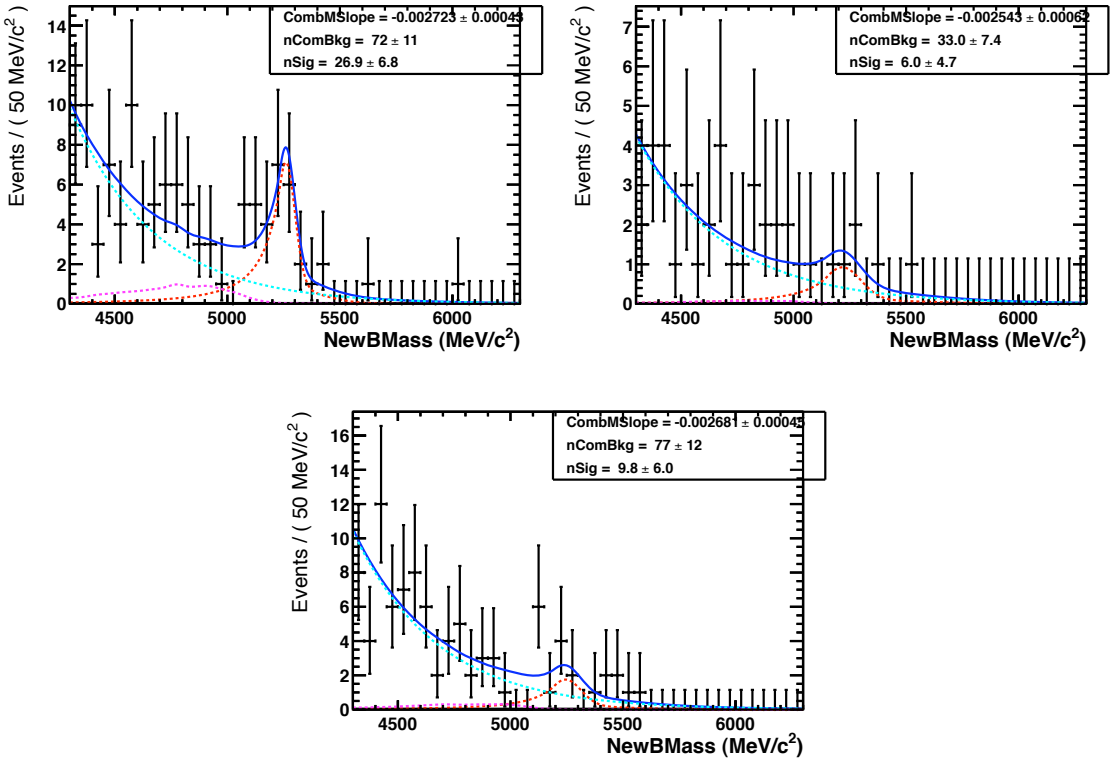

Figure 7: L'ajustement de la masse reconstruite pour chaque catégorie de déclenchement ($B^0 \to K^{*0} e^+ e^-$).

basés sur une utilisation pertinente du VELO. Le signal est extrait d'un ajustement de la distribution en masse des candidats. La forme du signal est extraite de la simulation, mais elle est corrigé pour les differences entre simulation et donnés en utilisant $B^0 \to J/\psi\,(e^+e^-)K^{*0}$. Les paramètres du bruit fond combinatoire sont laissés libres dans l'ajustement. La forme de la contribution issue de la reconstruction partielle des désintégrations des mésons beaux est fixée grâce à la simulation, et le rapport entre le nombre de ces événements et ceux du signal est mesuré grâce au $B^0 \to J/\psi\,(e^+e^-)K^{*0}$. L'ajustement de la masse reconstruite est montré dans Fig. 7 pour $B^0 \to K^{*0} e^+ e^-$ et dans Fig. 8 pour $B^0 \to J/\psi\,(e^+e^-)K^{*0}$. Un total d'une quarantaine de candidats $B^0 \to K^{*0} e^+ e^-$ sont observés. C'est déjà le plus important lot collecté par une expérience unique.

Les différentes contributions au rapport d'efficacité sont extraites soit de la simulation, soit des données elles-mêmes, et permet l'extraction du rapport

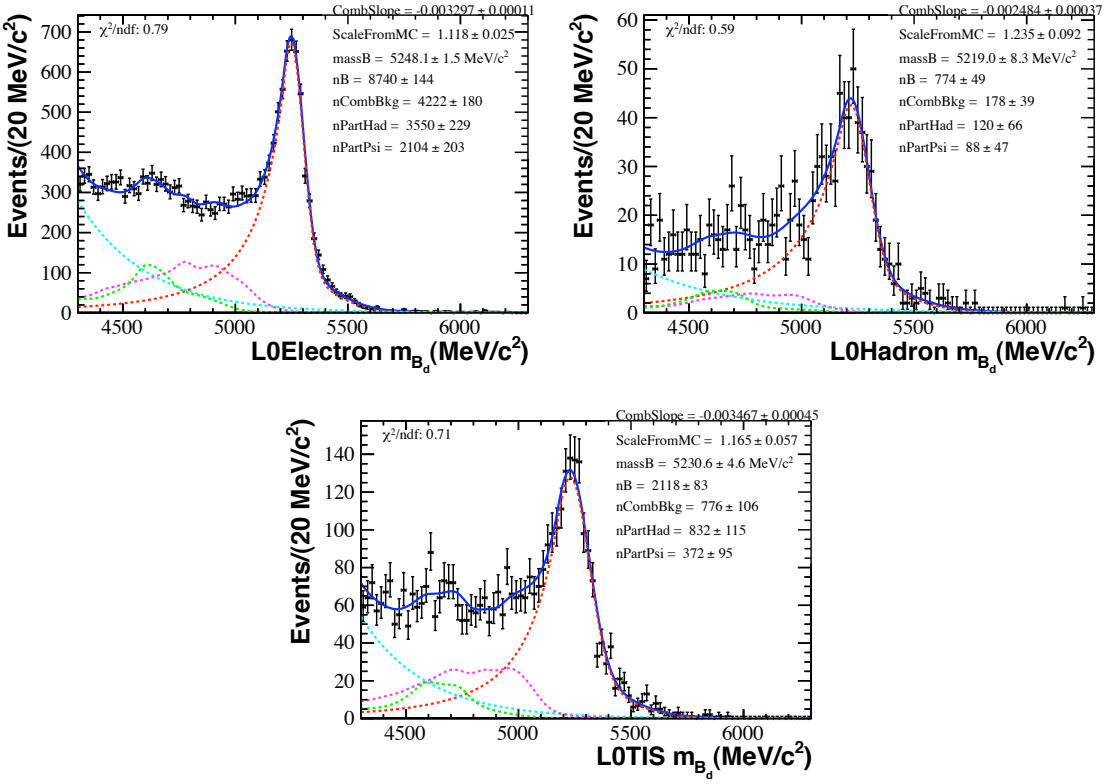

Figure 8: L'ajustement de la masse reconstruite pour chaque catégorie de déclenchement ($B^0 \to J/\psi\,(e^+e^-)K^{*0}$).

d'embranchement dans chaque catégorie de déclenchement. Les trois mesures sont combinées en donnant chacun un poids statistique pour trouver le rapport d'embrenchement moyenne:

$$\mathcal{B}(B^0 \to K^{*0}e^+e^-)^{30-1000\,\mathrm{MeV}/c^2} = (3.19^{+0.75}_{-0.68}(\mathrm{stat}) \pm 0.22(\mathrm{syst}) \pm 0.15(\mathrm{PDG})) \times 10^{-7}$$

en utilisant la valeur PDG pour le rapport d'embranchement de la désintégration $B^0 \to J/\psi\,(e^+e^-)K^{*0}$. Cette valeur est en accord avec la prédiction théorique.

Etude de sensibilité

En 2012, LHCb a enregistré une luminosité intégrée de 2 fb^{-1}. Donc, la combinaison de ceci avec l'échantillon de 2011 devrait fournir trois fois le nombre d'événements de $B^0 \to K^{*0} e^+ e^-$. Des études Monte Carlo démontre que la précision sur la fraction de photon polarisation droite devrait etre d'environ 0.1 avec 3 fb^{-1}, comparable à la moyenne mondiale obtenue avec des méthodes differentes.

Introduction

Mankind has long displayed a curiosity for understanding observations in nature, with records as far back as the last half millennium BC showing that the Babylonians had a mathematical understanding of astronomical observations [1]. Today, particle physics is the study of the interactions of, what are thought to be, the base constituents of matter. Its mathematical formulation can be written in what has come to be known as the Standard Model (SM) of particle physics.

The SM has proven to be immensely successful both in describing a varied and vast amount of experimental observations, and in its predictive powers. The only, as of yet, unconfirmed particle predicted by the SM is the Higgs boson. This year, observations have been made of a new particle with the relevant properties but further analysis is required to determine if this is indeed the SM Higgs.

However, there are several issues that are not addressed by the SM, suggesting that it may not be a complete theory. For example, it is unclear why the amount of CP violation permitted in the SM can not explain the asymmetry between matter and antimatter that is observed in the universe. Furthermore, the theory seems unnatural, requiring fine-tuning to account for hierarchy in *e.g.* why the gravitational interaction is so much weaker than the weak interaction.

Theoretical physicists have developed various extensions to the SM providing solutions to some of the issues raised. These theories agree with the SM at low energies and hence with the observations to date, but predict the existence of new particles and thus new physics (NP) at higher energies.

The purpose of the experiments at the LHC is to test the SM and to search for NP. The start of the LHC saw the beginning of searches at an unprecedented centre of mass energy and instantaneous luminosity. This allows for direct searches for new particles at high energies, as is currently being undertaken at ATLAS and CMS. An alternative method to probe NP is via indirect searches for its effects on known particles. LHCb is an experiment dedicated to the study of B mesons, primarily

focusing on the study of CP violation, and rare B decays.

The rare decay program at LHCb mainly analyses Flavour Changing Neutral Currents (FCNC). These transitions are highly suppressed in the SM and proceed only through higher order diagrams containing loops where virtual particles contribute. They are thus sensitive to the effects of NP. One such FCNC is the $b \to s\gamma$ transition, and of particular interest is the measurement of the polarisation of the photon. It is predicted to be predominantly left handed in the SM, but there exist NP models which can produce a right handed current.

One method to measure this photon polarisation is via an angular analysis of $B^0 \to K^{*0}e^+e^-$ in the dilepton mass range of [30-1000] MeV/c^2. To gain confidence in the analysis of decays containing electrons, of relatively low transverse momentum, in a challenging hadronic environment, an important first step is to measure the branching fraction in this dilepton mass range, which is the analysis carried out in this thesis.

Chapter 1, gives an overview of the key elements of the SM, along with further examples of its successes and shortcomings. A more detailed description of how to access the photon polarisation of $b \to s\gamma$ through the decay $B^0 \to K^{*0}e^+e^-$, as well as a review of other possible methods, is given in Chapter 2. Chapter 3 covers the experimental setup at the LHCb detector, giving details of the various subdetectors and their performance. The full analysis of the $B^0 \to K^{*0}e^+e^-$ branching ratio, using the 2011 dataset, is described in Chapter 4. The event selection, yield extraction, procedure for extracting the branching fraction with respect to $B^0 \to J/\psi K^{*0}$ and sources of systematical uncertainties, are discussed. Chapter 5 presents the prospects of measuring the photon polarisation using this channel when combining the 2011 and 2012 data samples, as well as the conclusions of this work.

Chapter 1

The Standard Model of particle physics

Contents

The Standard Model (SM) of particle physics sets out to describe the fundamental constituents of nature and their interactions, based on the observations made throughout the second half of the 20th century. Its theoretical formalism was completed in the 1970s, providing predictions of the existence of several, as of then, undiscovered particles. One decade after the proposal of their existence, the W and Z^0 were observed, with measured masses agreeing to great precision with the SM predictions [2],[3]. It has since been subject to intense scrutiny by the experimental high energy physics community. With the exception of neutrino masses [4],[5] no measurements have thus far been found to be in significant disagreement with the SM.

The SM is a gauge quantum field theory, describing the interaction of the matter constituents, known as fermions, via the exchange of force carrying particles, the gauge bosons. The gauge symmetry group can be written as $SU(3)_C \times SU(2)_L \times U(1)_Y$ with the first group, SU(3) [6], representing the strong interaction, and $SU(2)_L \times U(1)_Y$ describing the electroweak interaction [7].

These interactions, their mediating particles, and particles constituting matter, are described briefly in this chapter.

1.1 The fundamental particles

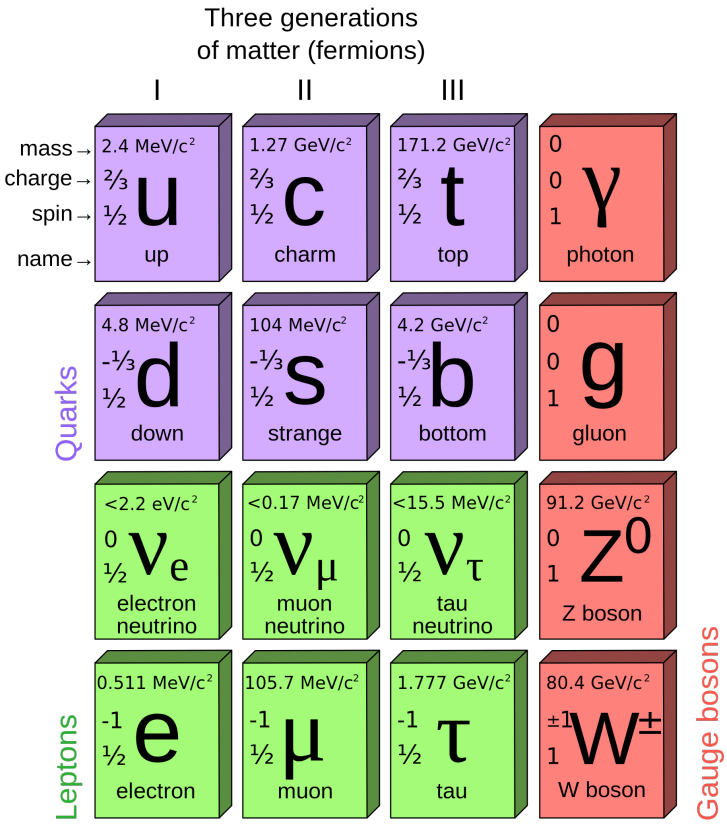

Figure 1.1: The fundamental particles of the Standard Model, according to family, generation and mass (and omitting the still unconfirmed, Higgs boson.)

As mentioned above, fermions are the elementary particles of all matter. These are spin 1/2 particles, which to date show no internal structure. Fermions can be further split into two classes, namely, quarks and leptons, of which there are 6

varieties each, and their antiparticles. Both quarks and leptons exist in three pairs, or *generations*, which differ from each other only in mass.

Each generation in the quark sector has one particle with +2/3 charge (up, charm, top), and one with charge -1/3 (down, strange, bottom). The quarks also have colour charge, (which can take three different values and thus giving 18 different quark states). They are never observed in isolation, existing only as mesons (one quark and one antiquark) or baryons (three quarks), although the extremely heavy top quark decays before hadronising.

Each generation in the lepton sector contains one charged lepton (e, μ, τ) and a corresponding neutral neutrino (ν_e, ν_μ, ν_τ).

There are four forces through which matter can interact: the strong, electromagnetic, weak and gravitational forces. All but the latter can be described in terms of quantum field theory in the SM, and so overviews of the electromagnetic, weak and strong forces alone will be given in the rest of this chapter. Each force is described by the exchange of its field quanta, giving rise to another 12 fundamental particles, the spin 1 vector gauge bosons. Namely, these are the 8 gluons for the strong force, the photon for the electromagnetic force and the neutral Z^0 and charged $W^\pm$ bosons for the weak force. The only remaining particle predicted by the SM is the gauge 0 Higgs boson, H [8](although in 2012, ATLAS and CMS independently presented discoveries of a new boson, which is consistent with being a SM Higgs, [9] and [10].) A diagram summarising the SM particles can be seen in figure 1.1.

1.2 The electromagnetic force

A gauge theory is one that is invariant under a set of local transformations. The electromagnetic (EM) force, described by Quantum Electrodynamics, affects all particles with electric charge, and is a force mediated by the exchange of virtual photons. These are the quanta of the gauge field whose existence are required to ensure the invariance of the fermion Lagrangian under local gauge transformation [11], as illustrated in the following argument.

Taking $\Psi(x)$ and $\overline{\Psi}(x)$ as the electron and positron fields with the Lagrangian density,

$$\mathcal{L} = \overline{\Psi}(i\gamma^\mu \partial_\mu - m)\Psi \tag{1.1}$$

under a local (*i.e.* space-time dependent) gauge transformation, the fields transform

as:

$$\begin{aligned}\Psi(x) \rightarrow \Psi'(x) &= e^{i\omega(x)}\Psi(x) \\ \overline{\Psi}(x) \rightarrow \Psi'(x) &= e^{i\omega(x)}\overline{\Psi}(x).\end{aligned} \tag{1.2}$$

Under these transformations, the Lagrangian density, 1.1 is not invariant due to the partial derivative between $\overline{\Psi}$ and Ψ acting on the space-time dependent term $\omega(x)$.

Gauge invariance can be restored by introducing a photon field, 'A_μ,' which interacts with the fermion fields with the interaction term:

$$-e\overline{\Psi}\gamma^\mu A_\mu \Psi \tag{1.3}$$

so that the Lagrangian density becomes:

$$\mathcal{L} = \overline{\Psi}(i\gamma^\mu(\partial_\mu + ieA_\mu) - m)\Psi. \tag{1.4}$$

For symmetry to be restored, it is also required that A_μ transforms under a gauge transformation as:

$$A_\mu \rightarrow A'_\mu = \frac{1}{e}\partial_\mu \omega(x). \tag{1.5}$$

In order to allow for the creation and annihilation operators for photons via expansion of the photon field, a kinetic term must be added. To avoid breaking the gauge invariance, this is done by introducing the electromagnetic field strength tensor:

$$F_{\mu\nu} = \partial_\mu A_\nu - \partial_\nu A_\mu \tag{1.6}$$

whose derivatives act on the A-field only. The complete Lagrangian density for EM is therefore:

$$\mathcal{L} = \overline{\Psi}(i\gamma^\mu(\partial_\mu + ieA_\mu) - m)\Psi - \frac{1}{4}F_{\mu\nu}F^{\mu\nu} \tag{1.7}$$

The Lagrangians for the other forces can be built in similar ways.

1.3 The strong force

The strong force is the SU(3) sector of the SM, and acts on quarks, being the only fermions to have colour charge, and the mediating bosons are the eight massless gluons. Two peculiar properties of the strong force are:

- **Asymptotic freedom [12],** meaning that the interactions between quarks and gluons becomes weaker at very high energies and short distances. This is in contrast to the EM force whose strength increases with decreasing distance, and arises due to the fact that the gluons themselves have colour charge, whereas photons have no electric charge.

- **Confinement.** A consequence of the increase in coupling with increasing distance is the non-existence of single quarks. In simplified terms, as two quarks are separated, it becomes more energetically favourable to create new quark-antiquark pairs. Thus, no isolated colour charges exist, with hadrons always occurring in colour-neutral states.

1.4 The weak interaction

The weak interaction affects all fermions, and is responsible for the radioactive decay of subatomic particles, with its best known effect being the β-decay.

The weak theory can be combined with the EM theory, to give the electroweak theory, based on $\mathrm{SU}(2)_L$ weak isospin symmetry and a $\mathrm{U}(1)_Y$ weak hypercharge phase symmetry. Out of all the interactions, the weak force alone allows for the changing of the flavour of quarks, and CP violation (see Section 1.5.) As the weak interaction violates parity, the fermions are split into left-handed and right-handed components. For the leptonic fields, this gives left handed doublets, with weak isospin $I = \frac{1}{2}$ and weak hypercharge $Y(L_l)$=-1 :

$$L_e = \begin{pmatrix} \nu_e \\ e^- \end{pmatrix}_L , \qquad L_\mu = \begin{pmatrix} \nu_\mu \\ \mu^- \end{pmatrix}_L , \qquad L_\tau = \begin{pmatrix} \nu_\tau \\ \tau^- \end{pmatrix}_L , \tag{1.8}$$

and right handed weak isosinglets with $Y(R_l)$=-2:

$$R_e = \ e_R \ , \qquad R_\mu = \ \mu_R \ , \qquad R_\tau = \ \tau_R \ . \tag{1.9}$$

Right handed neutrinos are not considered, as neutrinos are massless in the SM. For the quark sector, there are left handed quark doublets with weak isospin $I = \frac{1}{2}$ and

weak hypercharge $Y(L_q) = \frac{1}{3}$:

$$L_q^1 = \begin{pmatrix} u \\ d \end{pmatrix}_L \qquad L_q^2 = \begin{pmatrix} c \\ s \end{pmatrix}_L \qquad L_q^3 = \begin{pmatrix} t \\ b \end{pmatrix}_L \tag{1.10}$$

and right handed weak isoscalar quarks:

$$R_u^{(1,2,3)} = \; u_R, c_R, t_R \qquad R_d^{(1,2,3)} = \; d_R, s_R, b_R \tag{1.11}$$

with $Y(R_u) = \frac{4}{3}$ and $Y(R_d) = -\frac{2}{3}$.

As with the EM example, the invariance of the electroweak Lagrangian under local gauge transformations requires the existence of gauge particles, the $W^{\pm}$ and the Z^0, as well as the photon. However, the introduction of a mass term for these bosons in the Lagrangian, would again break the invariance, but the $W^{\pm}$ and Z^0 are indeed observed to be massive. Fermion masses are also forbidden, as e_L and e_R belong to different symmetry groups and hence transform differently.

To give the fermions and the weak bosons mass, a mechanism of spontaneous symmetry breaking, known as the Higgs mechanism [13]-[17], is introduced in the SM. The fundamental idea is to introduce a pseudo scalar field with a non-zero expectation value in the vacuum. The electroweak gauge fields then acquire mass through the interaction terms with this field, known as the Higgs field, and its associated quanta is the Higgs boson. Fermion masses also arise through interaction with the Higgs field, with masses that are proportional to the vacuum expectation value, but with values not predicted by the SM.

1.5 Symmetries, quark mixing and the CKM matrix in the SM

As already seen, symmetries are of paramount importance in particle physics, arising from conservation laws as observed in nature, as according to Noether's theorem [18], whenever a physical system is invariant under a continuous transformation, there exists a conserved quantity. Symmetries of particular interest are:

- The charge conjugation operator, C, which replaces all particles with their antiparticles so that the signs of the quantum numbers are reversed, but the momenta, masses and spins are unchanged.

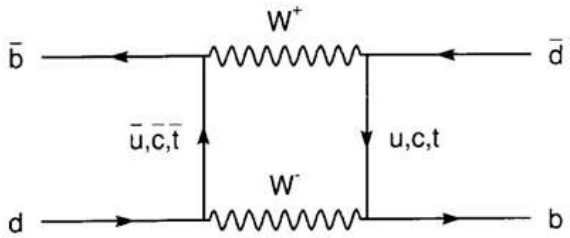

Figure 1.2: The $B^0_d \to \overline{B^0}_d$ mixing diagram.

- The parity operator, P, which changes the position vector of the particle so that it is reflected about the origin.
- The time reversal operator, T, which reverses the direction of motion by the reflection of the time axis.

CPT symmetry has always been observed to be conserved, and is an exact symmetry in any local Lagrangian field theory. C,P and T symmetries are conserved in strong and electromagnetic interactions in the Standard Model, but weak interactions violate each of them, and any combination of two, so as to conserve CPT. CP is almost exactly conserved in weak interactions, however CP violation has been observed in the neutral kaon system and more recently in the B system.

1.5.1 CP violation in the B meson system

CP violation processes can be classified in three ways:

- Direct CP violation
- CP violation in mixing
- CP Violation in interference

1.5.1.1 Direct CP Violation

CP is violated if the decay amplitude, A_f, for a B to its final state, f, and the complex conjugate of this process, $\overline{A}_{\overline{f}}$, have different magnitudes, resulting in the CP asymmetry:

$$\mathcal{A}_{CP} = \frac{\Gamma(\overline{B} \to \overline{f}) - \Gamma(B \to f)}{\Gamma(\overline{B} \to \overline{f}) + \Gamma(B \to f)} = \frac{1 - \left|\overline{A}_{\overline{f}}/A_f\right|^2}{1 + \left|\overline{A}_{\overline{f}}/A_f\right|^2} \tag{1.12}$$

This is the only source of CP violation for charged B mesons.

1.5.1.2 CP violation in mixing

As with neutral kaons, mixing occurs in the neutral B system due to the non-conservation of flavour in weak interactions. Hence, oscillations between $B^0_{s,d}$ and $\overline{B^0}_{s,d}$ can occur through the process shown by the box diagram in Fig. 1.2. B mesons are observed in two mass eigenstates, $|B_L\rangle$ (light) and $|B_H\rangle$ (heavy), which can be described by a linear combination of the two flavour eigenstates, B^0 and $\overline{B^0}$:

$$|B_L\rangle = p\left|B^0\right\rangle + q\left|\overline{B^0}\right\rangle \tag{1.13}$$

$$|B_H\rangle = p\left|B^0\right\rangle - q\left|\overline{B^0}\right\rangle \tag{1.14}$$

where the complex numbers p and q are normalised such that

$$|p|^2 + |q|^2 = 1 \tag{1.15}$$

CP violation occurs in mixing when $|q/p| \neq 1$, inducing an asymmetry between the transition possibilities of $B^0 \to \overline{B^0}$ and $\overline{B^0} \to B^0$

1.5.1.3 CP violation in interference

CP violation can arise when both the B^0 and $\overline{B^0}$ can decay to the same final state, due to interference between decays where mixing occurs, and those where it has not. For example, interference can occur between the decays $B^0 \to J/\psi\,\phi$ and $B^0 \to \overline{B^0} \to J/\psi\,\phi$, giving rise to a CP violating, known as ϕ_s. LHCb has made the most precise measurement to date of this parameter [19], and it is found to be in good agreement with the SM predictions [20].

1.5.2 CP violation within the Standard Model

As Cabibbo pointed out [21], quark mass eigenstates and flavour eigenstates need not be the same thing. The B mesons are produced and decay as flavour eigenstates, but

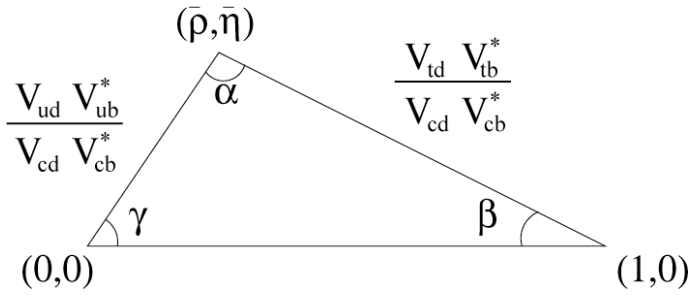

Figure 1.3: Diagram of the Unitarity Triangle with the bottom side normalised to one

propagate as mass eigenstates, written as a combination of the flavour eigenstates as in Eqs. 1.13, 1.14. Mixing occurs between the flavours, and this allows for CP violation in the Standard Model in the case of three generations of quarks. The mixing is parameterised in the Cabibbo-Kobayashi-Maskawa (CKM) matrix [22],[23], relating the weak eigenstates (d', s', b') to the mass eigenstates (d, s, b):

$$\begin{pmatrix} d' \\ s' \\ b' \end{pmatrix} = \begin{pmatrix} V_{ud} & V_{us} & V_{ub} \\ V_{cd} & V_{cs} & V_{cb} \\ V_{td} & V_{ts} & V_{tb} \end{pmatrix} \begin{pmatrix} d \\ s \\ b \end{pmatrix}$$

Of the nine parameters of the CKM matrix, five vanish by rephasing the quark fields to leave three real parameters, and one complex phase that parameterises CP violation. One way of parameterising the CKM matrix, which is useful in demonstrating the hierarchy of the elements, is the Wolfenstein parameterisation [24], which defines (with the current values determined by a fit to measurement given [25]:

$$\begin{aligned} \lambda &\approx 0.23 \\ A &\approx 0.81 \\ \rho - i\eta &\approx 0.14 - 0.35i \end{aligned} \tag{1.16}$$

and expands up to $\mathcal{O}(\lambda^3)$ to give:

$$\begin{pmatrix} 1 - \frac{1}{2}\lambda^2 & \lambda^2 & A\lambda^3(\rho - i\eta) \\ -\lambda & 1 - \frac{1}{2}\lambda^2 & A\lambda^2 \\ A\lambda^3(1 - \rho - i\eta) & -A\lambda^2 & 1 \end{pmatrix} + \mathcal{O}(\lambda^4)$$

It can now be seen that the diagonal terms are close to 1, and the complex phase only

enters at this order in transitions between the first and third generation. It is therefore surprising that LHCb has recently observed evidence for direct CP violation in D^0 mesons at $\mathcal{O}(10^{-3})$[26].

Requiring the CKM matrix to be unitary sets conditions on the matrix elements and allows for six triangles to be drawn in the complex plane due to the orthogonality between any pair of columns or any pair of rows. Two of these triangles have sides of a comparable length, and so are non degenerate as long as CP violation occurs and the complex phase exists. The one drawn from the condition

$$V_{ub}^* V_{ud} + V_{cb}^* V_{cd} + V_{tb}^* V_{td} = 0 \tag{1.17}$$

has fewer terms involving top quarks than the other, and so has sides that are experimentally easier to measure. This has become known as the Unitarity Triangle with angles α, β and γ and can be seen in Fig. 1.3 with the bottom side normalised to one. The sides of the triangle angles can be measured via the study of the decay rates of processes involving the relevant CKM elements, and the angles can be determined experimentally using measurements of CP asymmetries. Two collaborations [27],[28] currently perform fits of the CKM elements, to check for consistency across all measurements. The current experimental status of the Unitarity Triangle can be seen in Fig. 1.4. Comparing the γ angle found assuming the SM and in-

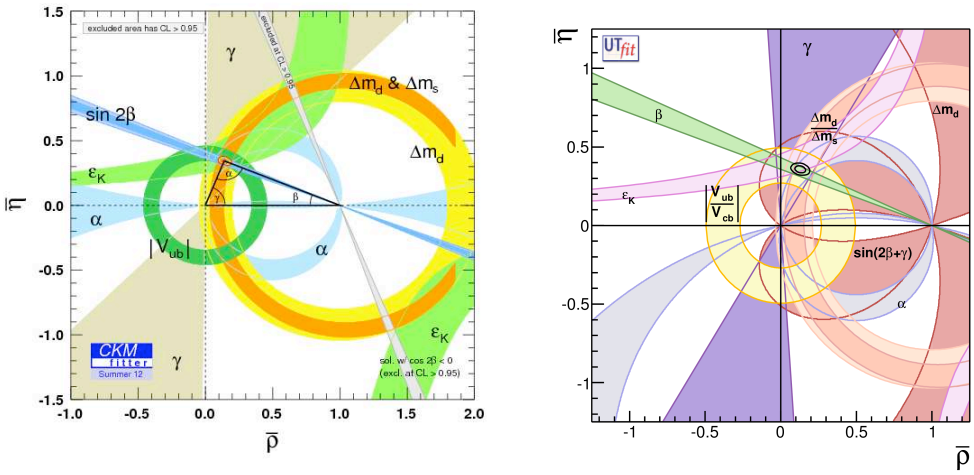

Figure 1.4: Current best fit of the Unitarity Triangle in the $(\overline{\rho}, \overline{\eta})$ plane, according to the CKM-Fitter collaboration 1.4(a) and UTFit 1.4(b).

cluding direct and indirect constraints, $(67.7^{+4.1}_{-4.3})^\circ$ [27]or $(68 \pm 3.1)^\circ$ [28], with the direct measurements $(66 \pm 12)^\circ$ or $(75.5 \pm 10.5)^\circ$, it can be seen that the results are consistent, but LHCb will provide unprecedented statistics of decays containing the suppressed $b \to u$ quark transition, which provides the sensitivity to γ. LHCb has already been able to perform its first measurement of γ, using $B^\pm \to DK^\pm$), finding [29] $\gamma = 71.1^{+16.6}_{-15.7}$. This analysis is based only on the 2011 data sample and is already comparable with the average from all other experiments to date.

1.5.3 The GIM mechanism

One feature of the CKM matrix is that Flavour Changing Neutral Currents (FCNCs) are suppressed in the SM, by what is known as the GIM mechanism, named after the proponents, Glashow, Iliopoulos, and Maiani [7]. Flavour changing charged currents arise due to the fact that the orientation of the up quark matrix is different from that of the down quark matrix. As the neutral currents couple up to up or down to down, there is no misalignment. There are hence no transitions between quarks of different flavour with the same charge at tree-level. FCNCs can therefore only occur in the SM at higher orders in perturbation theory, through loop processes such as penguin or box diagrams (see Fig. 1.5 for the loop diagram for the $b \to s\gamma$ transition.) However, this only occurs because of the mass differences between the up and down type quarks, otherwise, the unitarity requirement of the CKM matrix would cause the amplitudes to vanish. The GIM mechanism was proposed at the time when only three quarks had been discovered, but as it implied that the quarks should form doublets of the weak SU(2), it predicted the existence of the charm quark.

1.6 Challenges to the SM

Since its formulation, the SM has had immense success in describing many of the fundamental interactions observed in the universe. The electroweak sector particularly, has been subjected to many tests, all yielding experimental results that agree to a very high precision with the SM. It also predicted a wide variety of phenomena. Despite being established as a well-tested theory, there are several aspects of reality that can be observed in nature that the SM fails to provide an explanation for including:

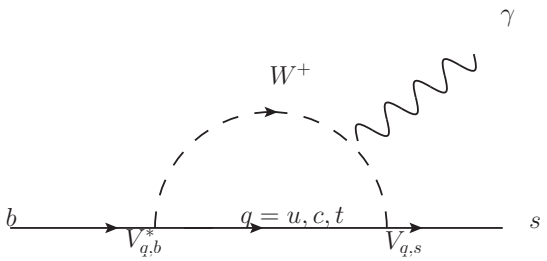

Figure 1.5: Loop diagram of the $b \to s\gamma$ transition.

- **Neutrino masses:** Neutrinos have been observed to be left-handed only, and the mass term requires fermions of opposite-handedness, they are massless in the SM. However, since the late 1990s, neutrino oscillations have been experimentally established, requiring non zero masses. An extension to the SM is required to include neutrino masses.

- **Gravity:** The gravitational force is one of the four fundamental forces of nature, but there is currently no formalism capable of describing general relativity in quantum field theory, and thus is not included in the SM.

- **Hierarchy:** The SM does not provide an explanation as to why it covers such vastly different scales, in particular, why the weak force is so much stronger than gravity. In order to obtain a Higgs boson that is at the electroweak scale rather than the Planck scale of $\approx 10^{19}$ GeV/c^2, fine tuning of the SM parameters is required, a seemingly unnatural feature of a fundamental theory.

- **Number of free parameters:** Although the gauge boson masses are related, there is no prediction for the relation of the fermion masses in the SM, leaving them free parameters of arbitrary value. There are 19 free parameters in total, again unsatisfactory for a fundamental theory.

- **Cosmology:** There exist observations in cosmology that can not be explained by the SM. For example, observations, including the rotation speeds of galaxies [30], suggest that there exists more matter than that which is accounted for by observable matter. It seems that most of the matter in the universe is of a

different nature from that described in the SM, and is primarily non-baryonic. Also, it is difficult in the SM to account for the matter-antimatter asymmetry that is observed in the universe. Sakharov pointed out [31] that there are three conditions necessary to explain the matter-antimatter asymmetry that is observed in the universe, namely the non conservation of the baryon number, B in particle interactions, deviation from thermal equilibrium and the non conservation of C-symmetry and CP-symmetry. All three of these conditions are required to occur in order to produce different amounts of matter and antimatter. The first condition is an obvious requirement to allow for the asymmetry, but has never been observed. The second requires that the rate of expansion of the universe must be less than the rate of baryon generation so that the particle and its antiparticle are not in thermal equilibrium and so cannot annihilate. CP violation, as explained in Section 1.5.2, is permitted within the Standard Model, but, without invoking new physics it is largely insufficient to explain the size of the matter-antimatter imbalance.

For reasons including those listed above, it is believed that there must exist New Physics (NP) beyond the SM. The goals of the experiments at the Large Hadron Collider at CERN include, searching for the last particle unconfirmed particle predicted by the SM, the Higgs boson, and searching for NP, perhaps providing some understanding of the unanswered issues listed above.

1.7 Beyond the Standard Model searches at LHCb

LHCb, as will be elaborated in Chapter 3.2, is a dedicated heavy flavour physics experiment. One key physics priority is to address the matter/antimatter asymmetry question listed above, by studying CP asymmetries in $B_{d,s}$ decays, and in particular, by measuring the γ angle of the Unitarity Triangle. To search for signs of NP, measurements of γ will be made from channels where Standard Model contributions dominate, and compared with channels that are sensitive to New Physics, in order to check for discrepancies. It is expected that processes that only involve tree level diagrams are well described by the Standard Model, and so will give a baseline against which to compare measurements of γ where penguin diagrams also contribute, as new physics may appear in loop processes.

As well as the CKM phases, another way to probe and constrain NP is through the measurement of FCNCs, and another key physics priority of LHCb is to exploit the high $b\bar{b}$ cross section at the LHC, to perform analysis of rare B decays proceeding in this way. One such decay, which is the subject of this thesis, is $B^0 \to K^{*0}e^+e^-$ which can be used to probe the helicity structure of NP by measuring the photon polarisation of the virtual photon in the process, predicted to be left-handed in the SM. This will be described in the following chapter.

Chapter 2

Probing the photon polarisation of $b \to s\gamma$

Contents

FCNCs are particularly sensitive to the effects of NP. They are forbidden at tree level in the SM and thus only proceeding via loop decays. Heavier NP particles can manifest in the loops and cause deviations from SM predictions. Although the branching ratio of one such FCNC, the $b \to s\gamma$ transition, has been measured to be consistent with SM predictions, [25], [32], new physics could still be present and detectable through the analysis of details of the decay process. One observable of which there is not yet a precise measurement, is the polarisation of the photon in $b \to s\gamma$, where its helicity depends on the couplings of the interactions of the particles inside the loop. As will be shown in Section 2.3 the photon polarisation is predominantly left handed in the SM. However, additional right handed currents can arise in certain new physics models, such as the Left-Right symmetric models, or in some supersymmetric models, (see for example, [33].) Therefore, the measurement of the photon polarisation can provide a probe to identify if the interactions inside

the $b \to s\gamma$ loop are SM-like.

Quark confinement prevents the direct measurement of $b \to s\gamma$, thus it is necessary to find a decay that connects experimental observations with the photon polarisation information, and is simultaneously free from large theoretical uncertainties. One available method is via an angular analysis of the decay $B \to K^* e^+ e^-$ in the region where the dilepton mass is less than 1 GeV [34]. It is shown in this reference, that in the low q^2 region, the branching ratio varies as $\frac{1}{q^2}$ where q^2 is the dielectron mass squared. The photon is the dominating contribution (diagram (f) and (g) of Fig. 2.1) in this region, and the angular distribution allows for the measurement of the photon polarisation, as:

$$\begin{aligned}\frac{d\Gamma}{d\phi} =& \frac{1}{2\pi}\Gamma(\overline{B} \to V\gamma)\left(\frac{\alpha}{2\pi}\log\frac{q^2_{max}}{(2m_e)^2}\right) \\ &\times\left\{1 - \frac{\mathrm{Re}(A_R(0)A_L^*(0))\cos 2\phi - \mathrm{Im}(A_R(0)A_L^*(0))\sin 2\phi}{|A_R(0)|^2 + |A_L(0)|^2}\right\} + ...,\end{aligned} \tag{2.1}$$

where $A_{(R,L)}(0)$ are the transverse helicity amplitudes at $q^2 = 0$, (the R and L subscripts signify the right and left handed polarisation amplitudes, respectively), and ϕ is the angle between the e^+e^- and $K\pi$ decay planes, in the rest frame of the B^0. The ellipses denote a neglected contribution from the longitudinal amplitude. It can therefore be seen, that information on the polarisation can be extracted from the ϕ dependence, due to interference between $A_{(R)}(0)$ and $A_{(L)}(0)$.

2.1 Effective Field Theories

It is useful to introduce here the effective field theories [36] to describe the decays. These are based on the principle that the dynamics at low energies do not depend on details of the dynamics at high energies. The low energy physics, where QCD is difficult to solve, can then be described with a set of variables and degrees of freedom suitable for that energy region, with high energy degrees of freedom, defined with respect to a mass scale μ, integrated out, and an effective Hamiltonian can be constructed. The framework used to achieve this is the Operator Product Expansion [37]. The effective Hamiltonian can then be parameterized as the sum of Operators, $\mathcal{O}_i$, which encode the long distance physics for interactions lower than μ, which originate to the full theory diagrams shown in Fig. 2.1, and Wilson coefficients,

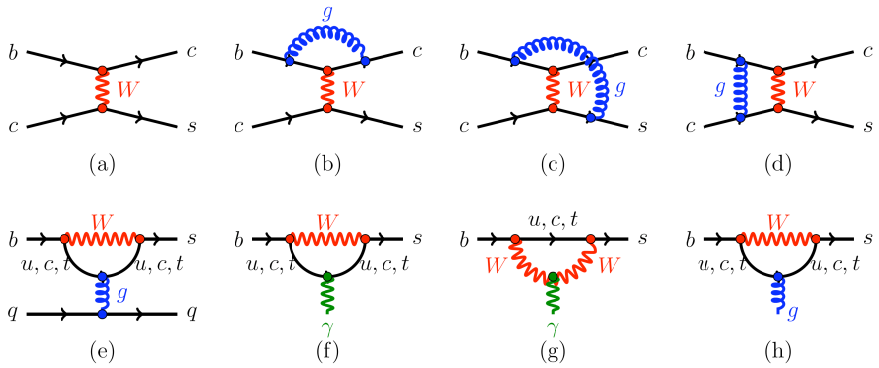

Figure 2.1: Typical diagrams from the full theory from which the operators $\mathcal{O}_i$ originate: current-current (a) with QCD corrections (b,c,d); gluon penguin (e); electromagnetic photon penguin (f, g);chromatic gluon penguin (h). Diagram taken from Ref. [35].

which are numerical coefficients and encode short distance perturbative effects. For B decays, μ is typically chosen to be $\mathcal{O}(m_b)$. The Wilson coefficients are calculated by evaluating them at a high mass scale, typically $\mu = m_W$ where perturbative calculations can be performed, a procedure known as *matching* of the full theory on to the effective theory, and then renormalisation techniques can be applied to find their values at the appropriate energy scale. The decay rates of loop processes are sensitive to the Wilson coefficients, and various observables can be constructed to test the structure of the operators, allowing for comparison with the SM.

2.2 Theoretical framework of $b \to s\ell^+\ell^-$

Following [38], the effective Hamiltonian describing the $b \to s\ell^+\ell^-$ transition, as found in $B^0 \to K^{*0}e^+e^-$, can be written as:

$$\mathcal{H}_{\text{eff}} = -\frac{4G_F}{\sqrt{2}} V_{tb}V_{ts}^* \sum_i^{10} [C_i(\mu)\mathcal{O}_i(\mu) + C_i'(\mu)\mathcal{O}_i'(\mu)] \tag{2.2}$$

where G_F is the Fermi coupling constant, and C_i' are the Wilson coefficients with reversed chirality. The first order contributions come from $\mathcal{O}_7$, which corresponds to the electromagnetic photon penguin diagrams (f) and (g) of Fig. 2.1, and $\mathcal{O}_9$ and $\mathcal{O}_{10}$, which are semileptonic operators. These operators can be written as:

$$\mathcal{O}_7 = \frac{e}{16\pi^2} m_b (\overline{s}\sigma_{\mu,\nu} P_R b) F^{\mu\nu}, \tag{2.3}$$

$$\mathcal{O}_9 = \frac{e}{16\pi^2} m (\overline{s}\gamma_\mu P_L b)(\bar{l}\gamma^\mu l), \tag{2.4}$$

$$\mathcal{O}_{10} = \frac{e}{16\pi^2} m (\overline{s}\gamma_\mu P_L b)(\bar{l}\gamma^\mu \gamma_5 l), \tag{2.5}$$

$$\tag{2.6}$$

where $P_{L,R} = \frac{(1\mp\gamma_5)}{2}$ and the mass scale $\mu = m_b$. The primed operators correspond to a right handed current.

2.3 Photon polarisation in the SM

Helicity is not conserved for massive particles, and so the $b \to s\gamma$ transition, dominated by the W exchange loop diagram, can either occur with the helicity structure, $b_R \to s_L\gamma_L$, or $b_L \to s_R\gamma_R$. As the W boson only couples with left handed fermions, the helicity flip must occur on one of the external quark legs. The helicity flip is proportional to the mass of the quark, and due to the large difference between m_b and m_s, in the SM the photon is predominantly left handed, with the amplitude or right handed polarisation over left handed polarisation, $\frac{A_R}{A_L} \approx \frac{m_s}{m_b}$. Gluon contributions to the loop can also give a small effect, leading to SM predictions of $\frac{A_R}{A_L}$= 3-4% (see Refs. [39] and [38]. Therefore, neglecting the mass of the strange quark, $\mathcal{O}_7'$ is only non-zero in certain extensions of the SM.

2.4 $B^0 \to K^{*0}e^+e^-$ as a probe to measure the photon polarisation

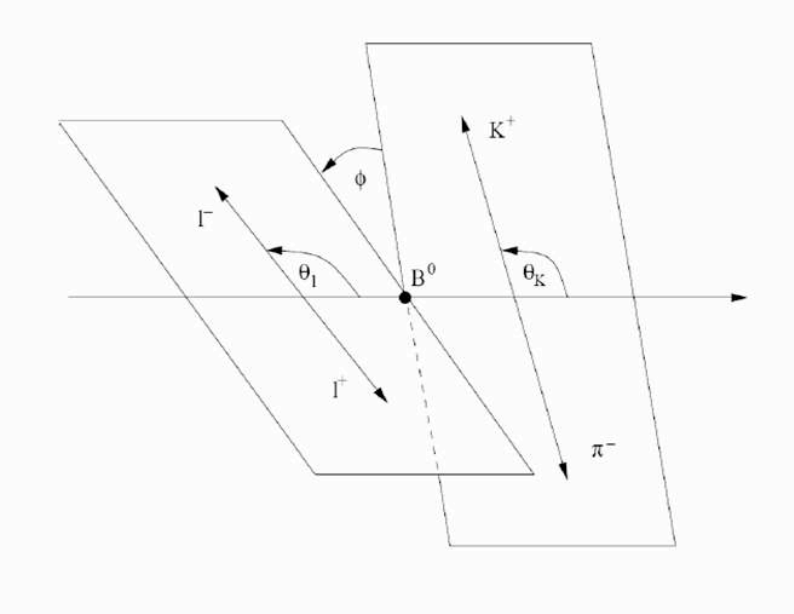

Figure 2.2: Definition of the angles ϕ, θ_K and θ_L in the decay $B \to K^* e^+ e^-$.

2.4.1 Decay Formalism

The $B^0 \to K^{*0} e^+ e^-$ decay can be completely described by four independent kinematical variables, q^2, defined as the dilepton mass squared and three angular variables, θ_L, θ_K and ϕ which are illustrated in Fig. 2.2.

The angles are defined as:

- ϕ: the angle between the planes defined by the K^* daughters and the dilepton daughters, in the rest frame of the B meson.
- θ_L: the angle between the direction vector of the e^+ (e^-) in the dilepton rest frame, and the direction of the dilepton in the B^0 ($\overline{B}^0$) rest frame
- θ_K: the angle between the direction vector of the K in the K^{*0} ($\overline{K}^{*0}$) rest frame, and the direction of the K^{*0} ($\overline{K}^{*0}$) in the B^0 ($\overline{B}^0$) rest frame.

Following the formalism as described in [38] the differential decay distribution can

then be written as:

$$\begin{aligned}\frac{d\Gamma}{dq^2 d\cos\theta_l d\cos\theta_K d\phi} = \frac{9}{32\pi}\big[&I_1(\cos\theta_K) + I_2(\cos\theta_K)\cos 2\theta_l + I_3(\cos\theta_K)\sin^2\theta_l\cos 2\phi \\ &+ I_4(\cos\theta_K)\sin 2\theta_l\cos\phi + I_5(\cos\theta_K)\sin\theta_l\cos\phi + I_6(\cos\theta_K)\cos\theta_l \\ &+ I_7(\cos\theta_K)\sin\theta_l\sin\phi + I_8(\cos\theta_K)\sin 2\theta_l\sin\phi \\ &+ I_9(\cos\theta_K)\sin^2\theta_l\sin 2\phi\big]\end{aligned} \tag{2.7}$$

where the I_i terms depend on products of the K* transversity amplitudes, which are sensitive to NP contributions, and are defined as:

$$\begin{aligned}I_1(\cos\theta_K) &= \left\{\frac{3}{4}[|A_{\perp L}|^2 + |A_{\parallel L}|^2 + |A_{\perp R}|^2 + |A_{\parallel R}|^2]\right\}\sin^2\theta_K \\ &\quad + (|A_{0L}|^2 + |A_{0R}|^2)\cos^2\theta_K \\ I_2(\cos\theta_K) &= \frac{1}{4}(|A_{\perp L}|^2 + |A_{\parallel L}|^2 + |A_{\perp R}|^2 + |A_{\parallel R}|^2)\sin^2\theta_K \\ &\quad - (|A_{0L}|^2 + A_{0R}|^2)\cos^2\theta_K \\ I_3(\cos\theta_K) &= \frac{1}{2}(|A_{\perp L}|^2 - |A_{\parallel L}|^2 + |A_{\perp R}|^2 - |A_{\parallel R}|^2)\sin^2\theta_K \\ I_4(\cos\theta_K) &= \frac{1}{\sqrt{2}}(\mathrm{Re}(A_{0L}A^*_{\parallel L}) + \mathrm{Re}(A_{0R}A^*_{\parallel R}))\sin 2\theta_K \\ I_5(\cos\theta_K) &= \sqrt{2}(\mathrm{Re}(A_{0L}A^*_{\perp L}) + \mathrm{Re}(A_{0R}A^*_{\perp R}))\sin 2\theta_K \\ I_6(\cos\theta_K) &= 2(\mathrm{Re}(A_{\parallel L}A^*_{\perp L}) + \mathrm{Re}(A_{\parallel R}A^*_{\perp R}))\sin^2\theta_K \\ I_7(\cos\theta_K) &= \sqrt{2}(\mathrm{Im}(A_{0L}A^*_{\perp L}) + \mathrm{Im}(A_{0R}A^*_{\perp R}))\sin 2\theta_K \\ I_8(\cos\theta_K) &= \frac{1}{\sqrt{2}}(\mathrm{Im}(A_{0L}A^*_{\perp L}) + \mathrm{Im}(A_{0R}A^*_{\perp R}))\sin 2\theta_K \\ I_9(\cos\theta_K) &= (\mathrm{Im}(A_{\parallel L}A^*_{\perp L}) + \mathrm{Im}(A_{\parallel R}A^*_{\perp R}))\sin^2\theta_K\end{aligned} \tag{2.8}$$

where the labels on the transversity amplitudes, L and R, refer to the chirality of the lepton current, and the lepton has been considered as massless, which is a very good approximation in the case of $B^0 \to K^{*0}e^+e^-$.

From Eq. 2.1, it can be seen that the photon polarisation can be determined from a measurement of $\cos 2\phi, \sin 2\phi$ and so, from Eq. 2.7, the sensitive terms are I_3 and I_9. The differential branching fraction can be simplified by 'folding' the

distribution, such that if $\phi < 0$, then $\phi \to \phi + \pi$.* The I_4, I_5, I_7 and I_8 terms then disappear, but without loss of sensitivity on the $\sin 2\phi$ and $\cos 2\phi$ terms.

It can be further simplified by performing a similar transformation for $\cos\theta_L$, by folding the region $(0, +\pi/2)$ over $(\pi/2, \pi)$. This cancels the I_6 term without removing sensitivity to I_3 and I_9.

Given the effective Hamiltonian, Eq. 2.2, the transversity amplitudes can be written as:

$$A_{\perp L,R} = N(q^2)\sqrt{2\lambda(q^2)}\left\{\frac{2m_b}{q^2}(C_7^{eff} + C_7^{eff'})T_1(q^2) + (C_9^{eff} \mp C_{10})\frac{V(q^2)}{m_B + m_K^*}\right\}$$

$$A_{\parallel L,R} = -N(q^2)\sqrt{2}(m_B^2 + m_{K^*}^2)\left\{\frac{2m_b}{q^2}(C_7^{eff} + C_7^{eff'})T_2(q^2) + (C_9^{eff} \mp C_{10})\frac{A_1(q^2)}{m_B + m_K^*}\right\}$$

$$A_{0L,R} = -\frac{N}{2m_{K^*}\sqrt{q^2}}\left\{2m_b(C_7^{eff} - C_7^{eff'})[(m_B^2 + 3m_{K^*}^2 - q^2)T_2(s) - \frac{\lambda(q^2)}{m_B^2 + m_{K^*}^2}]\right.$$
$$\left. + (C_9^{eff} \mp C_{10})[(m_B^2 - m_{K^*}^2 - q^2)(m_B + m_{K^*})A_1(q^2) - \lambda\frac{A_2(q^2)}{m_B + m_{K^*}}\right\}.$$

where C_i^{eff} is an effective coefficient that appears in the physical amplitude, defined by factorising the Wilson coefficients that multiply the same matrix elements, and

$$N(q^2) = V_{tb}V_{ts}^*\left[\frac{G_F^2\alpha^2}{2^{10}\pi^5 m_B^3}\frac{1}{2}q^2\sqrt{\lambda(q^2)}\right]^{1/2}, \tag{2.9}$$

$$\lambda(q^2) = \left[q^2 - (m_B + m_{K^*})^2\right]\left[q^2 - (m_B - m_{K^*})^2\right], \tag{2.10}$$

and $V(q^2), A_{0,1,2}(q^2), T_{1,2,3}(q^2)$ are the form factors that parameterise the hadronic matrix element of Eq. 2.2.

In order to separate hadronic effects present in the form factors and potential NP effects present in the Wilson coefficients, one can re-express the differential rate using the ratio of amplitudes. Several variables are proposed in the literature, but of particular interest is the expression (obtained, after the folding of ϕ and $\cos\theta_L$):

*This is possible since the acceptance is flat in ϕ.

$$\frac{1}{\Gamma'}\frac{d\Gamma}{dq^2 d\cos\theta_l^* d\cos\theta_K d\phi^*} = \frac{9}{32\pi}[I_1^{'}(\cos\theta_K) + I_2^{'}(\cos\theta_K)\cos 2\theta_l^* + I_3^{'}(\cos\theta_K)\sin^2\theta_l^*\cos 2\phi^* + I_9^{'}(\cos\theta_K)\sin^2\theta_l^*\sin 2\phi^*] \tag{2.11}$$

with

$$\begin{aligned}\Gamma^{'} &= |A_{0L}|^2 + |A_{0R}|^2 + |A_{\parallel L}|^2 + |A_{\parallel R}|^2 + |A_{\perp L}|^2 + |A_{\perp R}|^2 \\ &= |A_0|^2 + |A_\parallel|^2 + |A_\perp|^2\end{aligned} \tag{2.12}$$

and the I_i terms can be expressed as:

$$\begin{aligned}I_1^{'}(\cos\theta_K) &= \frac{3}{4}(1-\mathrm{F_L})\times(1-\cos^2\theta_\mathrm{K}) + \mathrm{F_L}\times\cos^2\theta_\mathrm{K} \\ I_2^{'}(\cos\theta_K) &= \frac{1}{4}(1-\mathrm{F_L})\times(1-\cos^2\theta_\mathrm{K}) - \mathrm{F_L}\times\cos^2\theta_\mathrm{K} \\ I_3^{'}(\cos\theta_K) &= \frac{1}{2}(1-\mathrm{F_L})\times\mathrm{A_T^{(2)}}\times(1-\cos^2\theta_\mathrm{K}) \\ I_9^{'}(\cos\theta_K) &= \frac{1}{2}(1-\mathrm{F_L})\times\mathrm{A_T^{(Im)}}\times(1-\cos^2\theta_\mathrm{K})\end{aligned} \tag{2.13}$$

where,

$$\mathrm{F_L} = \frac{|\mathrm{A_0}|^2}{|\mathrm{A_0}|^2 + |A_\perp|^2 + |A_\parallel|^2}, \tag{2.14}$$

$$\mathrm{A_T^{(2)}} = \frac{|\mathrm{A_\perp}|^2 - |\mathrm{A_\parallel}|^2}{|\mathrm{A_\perp}|^2 + |\mathrm{A_\parallel}|^2}, \tag{2.15}$$

and

$$\mathrm{A_T^{Im}} = \frac{2\Im\left[\mathrm{A_{\parallel L}A_{\perp L}^*} + \mathrm{A_{\parallel R}A_{\perp R}^*}\right]}{|\mathrm{A_\perp}|^2 + |\mathrm{A_\parallel}|^2}. \tag{2.16}$$

2.4.2 Transversity amplitudes at low q^2

The full differential decay distribution as described in Section 2.4.1 is difficult to use, for two main reasons. Firstly, the heavy-to-light transition hadronic form factors entering via the transversity amplitudes, $V(q^2), A_{0,1,2}(q^2), T_{1,2,3}(q^2)$, are difficult to calculate, and thus suffer from large theoretical uncertainties. Secondly, it is only possible to compute partial decay rates, as the form factors are q^2 dependent, and

none of the methods to compute form factors is applicable over the whole q^2 range. Furthermore, the effective Hamiltonian also does not take into account the $c\bar{c}$ resonances.

However, the transversity amplitudes can be simplified in the limit where $m_B \to \infty$ and $E_{K^*} \to \infty$, *i.e.* at low q^2 values. In this case, the seven form factors listed above can be written in terms of two universal form factors, $\xi_\perp$ and $\xi_\parallel$. The transversity amplitudes can then be rewritten, at leading order $1/m_b$ and α_s as:

$$A_{\perp L,R} = N(q^2) m_B \sqrt{2}(1-\widehat{s}) \left\{ \frac{2\widehat{m_b}}{\widehat{s}} (C_7^{eff} + C_7^{eff\prime}) + (C_9^{eff} \mp C_{10}) \right\} \xi_\perp(E_{K^*})$$
$$A_{\parallel L,R} = -N(q^2) m_B \sqrt{2}(1-\widehat{s}) \left\{ \frac{2\widehat{m_b}}{\widehat{s}} (C_7^{eff} - C_7^{eff\prime}) + (C_9^{eff} \mp C_{10}) \right\} \xi_\perp(E_{K^*})$$
$$A_{0L,R} = -\frac{N(q^2) m_B}{\widehat{K^*}\sqrt{\widehat{s}}} (1-\widehat{s})^2 \left\{ 2\widehat{m_b}(C_7^{eff} - C_7^{eff\prime}) + (C_9^{eff} \mp C_{10}) \right\} \xi_\parallel(E_{K^*})$$

where $\widehat{s} = q^2/m_B^2, \widehat{m_i} = m_i/m_B$, and terms of $\mathcal{O}$ $(\widehat{m}^2_{K^*})$ have been neglected. From these expressions, one obtains, (when $q^2 \to 0$):

$$\lim_{q^2\to 0} \mathrm{A_T^{(2)}} = \frac{2\mathrm{Re}\left[C_7^{eff} C_7^{eff\prime *}\right]}{|C_7^{eff}|^2 + |C_7^{eff\prime *}|^2}, \tag{2.17}$$

and

$$\lim_{q^2\to 0} \mathrm{A_T^{(Im)}} = \frac{2\mathrm{Im}\left[C_7^{eff} C_7^{eff\prime *}\right]}{|C_7^{eff}|^2 + |C_7^{eff\prime *}|^2}, \tag{2.18}$$

This is due to the fact that at very low q^2 the electromagnetic penguin diagram where the leptons are produced by a virtual photon is dominant. These expressions are strictly valid only at q^2=0. For a measurement in a low q^2-bin, away from any resonances and assuming OPE is valid, following Ref. [40], one can use the approximation:

$$\mathrm{A_T^{(2,Im)}}(q^2) = a_0^{(2,\mathrm{Im})} + a_1^{(2,\mathrm{Im})} q^2 + \mathcal{O}(q^4), \tag{2.19}$$

where the intercepts and slopes are:

$$a_0^{(2,\mathrm{Im})} = \lim_{q^2\to 0} \mathrm{A}_\mathrm{T}^{(2,\mathrm{Im})}(q^2), \quad a_1^{(2,\mathrm{Im})} = \left.\frac{\partial \mathrm{A}_\mathrm{T}^{(2,\mathrm{Im})}(q^2)}{\partial q^2}\right|_{q^2=0}. \tag{2.20}$$

A non zero measurement of $\mathrm{A}_\mathrm{T}^{(2)}$ at low q^2 would be a sign of new physics coming from right handed currents, and for $\mathrm{A}_\mathrm{T}^{(\mathrm{Im})}$, it would mean that there is a NP phase in C_7 or C_7' or both. Fig. 2.3, taken from Ref. [41], shows how NP phases and amplitudes can change the q^2 dependence of the asymmetries, particularly in the low q^2 region.

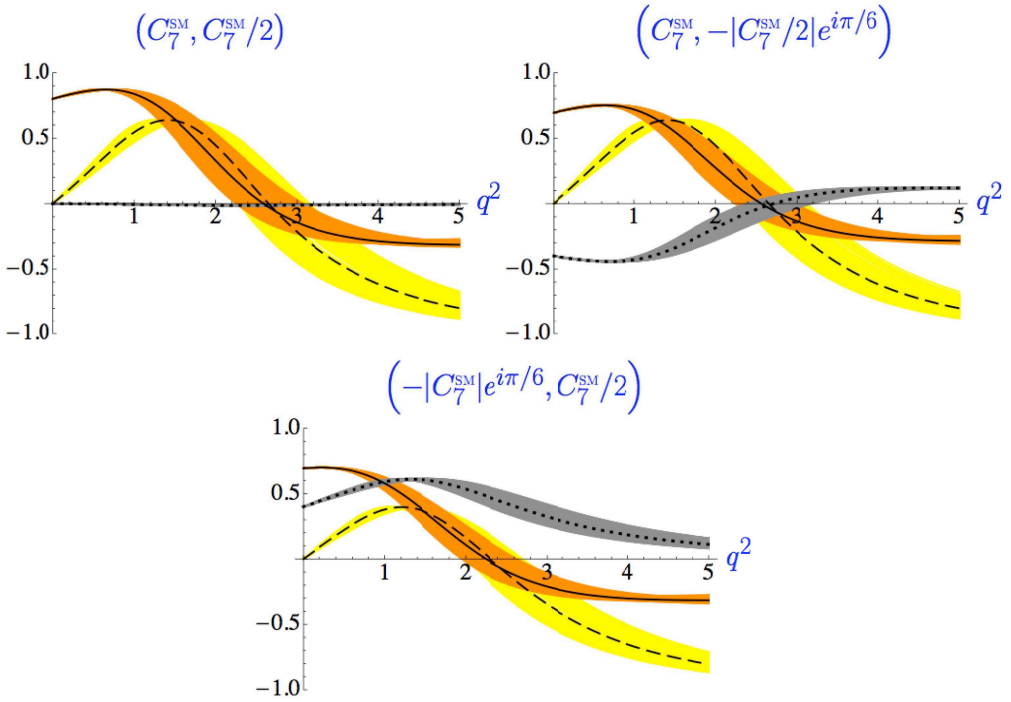

Figure 2.3: Dependence of the asymmetries $\mathrm{A}_\mathrm{T}^{(2)}$ (solid line) and $\mathrm{A}_\mathrm{T}^{(\mathrm{Im})}$(dotted line) on q^2 for different scenarios of (C_7, c_7'). The dashed line shows a similar asymmetry, $\mathrm{A}_\mathrm{T}^{(\mathrm{Re})}$, not discussed here. Diagram taken from Ref. [41].

2.4.3 Fitting procedure at LHCb

When measuring this rate at LHCb, the 3D angular acceptance, $\varepsilon\left(q^2 \cos\theta_l^*, \cos\theta_K, \phi^*\right)$ must also be taken into account. For a charge symmetric detector, and assuming that the level of direct CP violation is small, the acceptance is an even function of $\cos\theta_L$. The acceptance in ϕ is expected to be flat in restricted q^2 bins. Equation 2.7 can then be rewritten as:

$$\begin{aligned}\frac{1}{\Gamma'}\frac{d\Gamma}{dq^2 d\cos\theta_l^* d\cos\theta_K d\phi^*} = \frac{9}{32\pi}\Big[&I_1'(\cos\theta_K + I_2'(\cos\theta_K)\cos 2\theta_l^* + I_3'(\cos\theta_K)\sin^2\theta_l^*\cos 2\phi^* \\ &+ I_9'(\cos\theta_K)\sin^2\theta_l^*\sin 2\phi^*\Big] \\ &\times \varepsilon_D(q^2, \cos\theta_l^*, \cos\theta_K, \phi^*)\end{aligned} \tag{2.21}$$

As can be seen from Eq. 2.13, the sensitivity to $A_T^{(2)}$ and hence the sensitivity to NP affecting C_7' depends on knowledge of F_L, which varies with q^2, as shown in Fig. 2.4. The sensitivity is greatest at q^2=0 whereas at dilepton masses greater than 2 GeV/c^2, $F_L \approx$1, giving very low sensitivity. The analysis with muons in the final state can be done using a similar procedure, but with modifications required to the differential decay due to the non-negligible lepton mass. Including the lepton mass modifies the I_3 of Eq. 2.13 by a factor:

$$\frac{1-x}{1+\frac{x}{2}} \tag{2.22}$$

where $x = \frac{4m_l^2}{q^2}$. As I_3 is the term from which $A_T^{(2)}$ can be measured, this results in a loss of sensitivity as a function of q^2, when compared to the electron analysis. However, above a dilepton mass of $\approx 1\,\text{GeV}/c^2$, the muon mode has similar sensitivity as the electron mode, but is experimentally much easier to detect. The $B^0 \to K^{*0}e^+e^-$ analysis is therefore restricted to the region where the dilepton mass is less than 1 GeV/c^2.

A lower limit is also necessary, as the size of the opening angle between the two electrons decreases with decreasing invariant mass. This causes problems with the tracking, as hits from the electrons can be assigned to the wrong track, creating cloned tracks. Furthermore, for very small dielectron masses, multiple scattering has a major effect on the reconstruction of the dilepton decay angles and decay

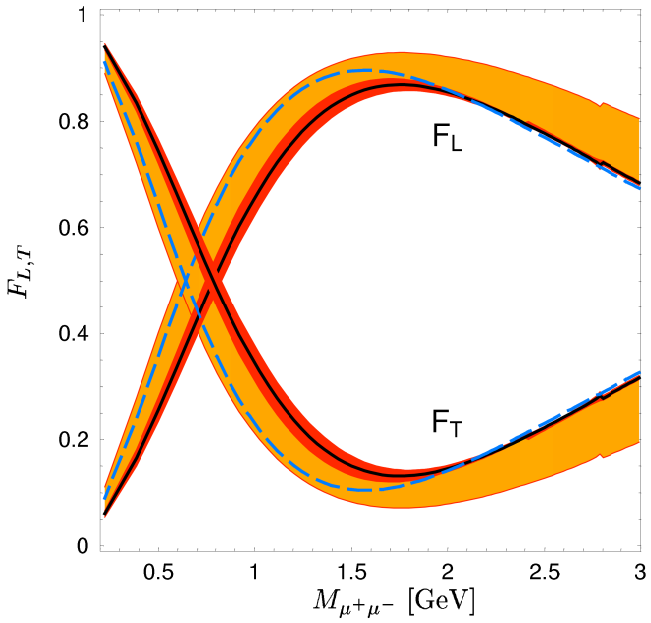

Figure 2.4: Variation of F_L with the dilepton mass according the SM. Diagram taken from Ref. [38].

plane. The RMS of the resolution of the ϕ angle for various bins of dielectron mass is shown in Figure 2.5. As can be seen, above 30 MeV/c^2, the resolution is good enough to measure $\cos 2\phi$ or $\sin 2\phi$.

Hence, the dilepton mass range chosen to carry out this analysis is [30-1000] MeV/c^2.

2.5 Other methods for measuring the photon polarisation

There have been several other methods proposed to access the photon polarisation methods, each bringing their own advantages and disadvantages. The combination of different methods can be useful in putting strong constraints on the $C_7^{(\prime)}$ coefficients, and hence on any NP models, in a model-independent manner [40]. Another method providing indirect determination of the photon polarisation comes from the study of the time-dependent CP-asymmetry in neutral B mesons decaying to a photon and a CP eigenstate, *i.e.* $B \to f^{CP}\gamma$, two examples of which are $B^0 \to K^*$ $(K_S^0\ \pi^0)\gamma$,[42],

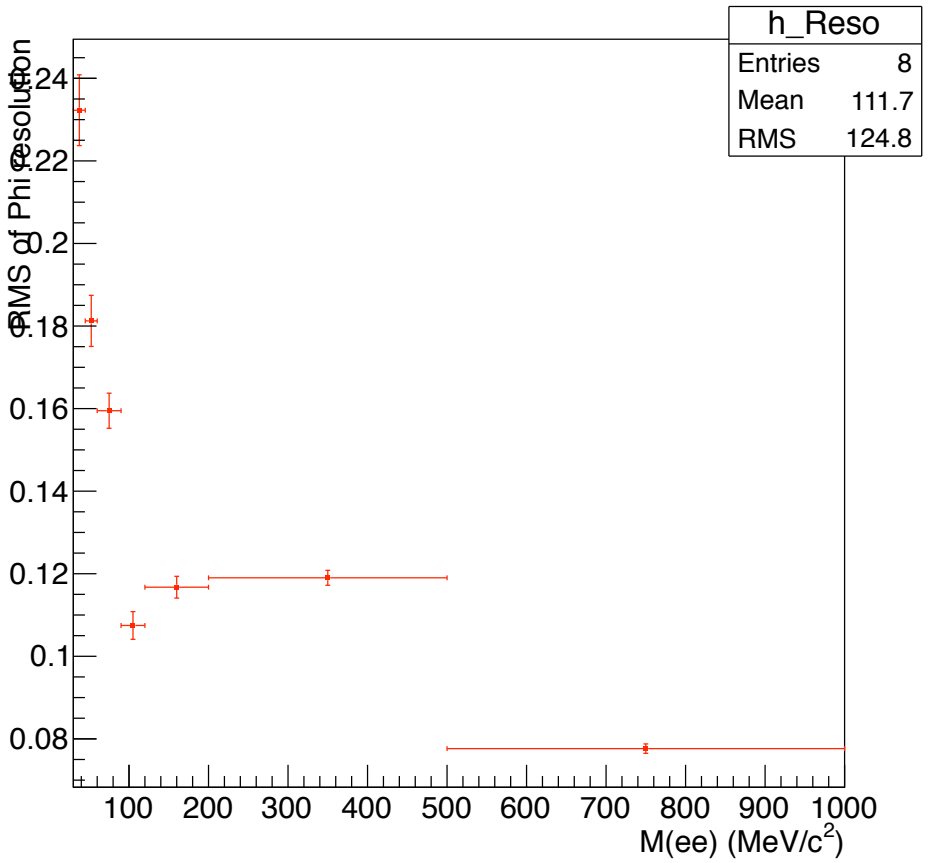

Figure 2.5: RMS of the ϕ angle resolution in bins of M(e^+e^-).

[43], [44] and $B_s^0 \to \phi\gamma$ [45]. A direct measurement can be made from the angular analysis of decays of the type $B \to P_1P_2P_3\gamma$ where P_i is are pseudoscalar mesons, pions or kaons [46], and one such method has been proposed using $B \to K_1\gamma \to (K\pi\pi)\gamma$ [47]. Each of these methods will be briefly outlined below.

2.5.1 $B^0 \to K^*\,(K^0_S\,\pi^0)\gamma$

CP asymmetry arises for decays of the type $B \to f^{CP}\gamma$, as there is interference between the decay where mixing of the B occurs and those where it does not, since the B and $\overline{B}$ both can decay to the same final state. However, as the dominant amplitudes are $B(\overline{B}) \to f^{CP}\gamma_{R(L)}$, and $B(\overline{B}) \to \overline{B}(B) \to f^{CP}\gamma_{L(R)}$, and states with different helicities can not interfere quantum-mechanically, the asymmetry is

expected to be zero in the SM, with corrections up to $\mathcal{O}\ (m_s/m_b)$. Any NP generating a sizable contribution to the wrong-helicity amplitudes can cause deviations from zero.

Following [44], for $B^0 \to K^{*0}\gamma$, neglecting direct CP violation, and the small width difference between B^0 and $\overline{B}^0$ the CP asymmetry can be written as:

$$\frac{\Gamma(\overline{B}(t) \to \overline{K}^{*0}\gamma) - \Gamma(B(t) \to K^{*0}\gamma)}{\Gamma(\overline{B}(t) \to \overline{K}^{*0}\gamma) + \Gamma(B(t) \to K^{*0}\gamma)} = S_{K^*\gamma} \sin(\Delta m t) - C_{K^*\gamma} \sin(\Delta m t). \quad (2.23)$$

where the K^{*0} and $\overline{K}^{*0}$ decay to the CP eigenstate, $K_s\pi^0$ and

$$S_{K^*\gamma} = \frac{2Im\left[\frac{q}{p}\left(A_L^*\overline{A_L} + A_R^*\overline{A_R}\right)\right]}{|A_L|^2 + |A_R|^2 + |\overline{A_L}|^2 + |\overline{A_R}|^2} \quad (2.24)$$

and

$$C_{K^*\gamma} = \frac{|A_L|^2 + |A_R|^2 - |\overline{A_L}|^2 - |\overline{A_R}|^2}{|A_L|^2 + |A_R|^2 + |\overline{A_L}|^2 + |\overline{A_R}|^2} \quad (2.25)$$

where $|\frac{q}{p}|$ =1 by neglecting CP violation in mixing of B mesons, a good approximation since all measurements to date are extremely small.

The parameter $S_{K^*\gamma}$ is highly sensitive to right handed currents, and can be written as:

$$S_{K^*\gamma} = \sin(2\psi)\sin 2\beta \quad (2.26)$$

where ψ contains the information of the amplitudes of the wrong photon polarisation such that

$$\tan\psi = \frac{A(\overline{B} \to K^{*0}\gamma_R)}{A(\overline{B} \to K^{*0}\gamma_L)} \quad (2.27)$$

and β is the angle of the Unitarity Triangle, as shown in Fig. 1.3. This method therefore only provides a measurement of the right-handed amplitude, along with the B-$\overline{B}$ mixing phase.

The current experimental precision on $S_{K^*\gamma}$ is -0.16 ± 0.22 [48], to be compared with SM predictions of -0.023 ± 0.016 [49]. This decay can not be studies at LHCb, but there are excellent prospects to improve the precision on the experimental measurement at the next generation of B Factories [50].

2.5.2 $B_s^0 \to \phi\gamma$

$B_s^0 \to \phi\gamma$ is another decay of the type $B \to f^{CP}\gamma$, and thus information on the polarisation can be extracted in a manner similar to $B^0 \to K^*$ $(K_S^0\ \pi^0)\gamma$. However, in this instance, the width difference in B_s mesons in non-negligable, and leads to one more observable. Based on MC simulation, it is shown that with an integrated luminosity of 2 fb^{-1} at the design LHC centre of mass energy, $\sqrt{s} = 14\,\text{TeV}$, LHCb can measure the ratio of right-handed photon polarisation amplitude over the left-handed photon polarisation amplitude to a precision of ≈ 0.1 [51]. However, this analysis is very sensitive to the acceptance of the decay time, and requires knowledge of the acceptance to a few percent [52].

2.5.3 $B \to P_1P_2P_3\gamma$

The photon helicity is parity odd, and as only the momenta of the photon and the final state hadrons can be measured, it is not possible to form a parity-odd hadronic quantity using $B^0 \to K^{*0}\gamma$ with the K^* decaying into πK or $K_S\pi^0$. However, for the three body decay of K_1, one can build the triple product of the three momenta. for example, with $B \to K_1\gamma \to K\pi\pi\gamma$, $\vec{p_\gamma} \cdot (\vec{p_\pi} \times \vec{p_K})$ is a pseudoscalar, and applying parity transformation yields the opposite sign for left and right-handed photons. The study of the angular polarisation allows for the extraction of the polarisation parameter [46]:

$$\lambda_\gamma = \frac{\Gamma(\overline{B} \to \overline{K_{1R}}\gamma_R) - \Gamma(\overline{B} \to \overline{K_{1L}}\gamma_L)}{\Gamma(\overline{B} \to \overline{K_1}\gamma)} \approx \frac{|C_7^{eff'}|^2 - |C_7^{eff}|^2}{|C_7^{eff'}|^2 + |C_7^{eff}|^2} \tag{2.28}$$

and can be measured via an up-down asymmetry. As can be seen, λ_γ measures the square of the right handed amplitude over the left, and thus is not very sensitive in the case where any NP contribution is small. One method to improve experimental sensitivity to λ_γ is given in [47].

Chapter 3

The LHCb Experiment at the LHC

The Large Hadron Collider (LHC) circulated its first beam in autumn 2008, and in November 2009, delivered its first proton-proton collisions, and following a smooth commissioning period, a week later began its era as the world's highest-energy particle accelerator. The 27 km circumference machine is housed in the tunnel built for CERN's previous accelerator, the Large Electron Positron collider (LEP), with the main experiments located at four of the various interaction points. CMS and ATLAS, are general purpose detectors (GPDs), whose main goals include searching for the Higgs boson, and direct searches for new physics particles, such as supersymmetric particles. ALICE is optimised to analyse lead-lead nuclei collisions, where the energy and density is expected to be large enough to observe signs of a new phase of matter where quarks and gluons are deconfined. LHCb is an experiment dedicated to the study of flavour physics, as will be detailed in Section 3.2.

3.1 LHC

As can be construed from its full name, the European Organization for Nuclear Research, CERN began as a laboratory dedicated to the study of nuclear physics, but as the understanding of physics developed, it switched emphasis to high energy physics, building its first major particle accelerator, the PS in the 1950s. The PS is still used in the chain of accelerators today, the complete diagram of which can be seen in Fig. 3.1. All protons collided in the LHC originate from a small bottle of

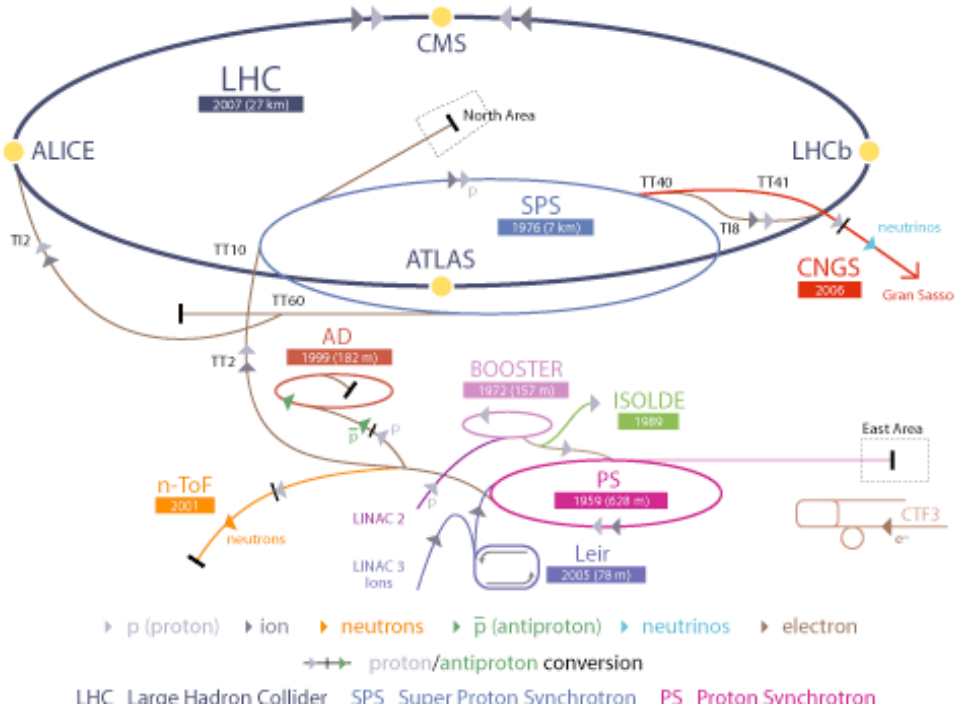

Figure 3.1: The chain of accelerators from the LINACs providing the particles, to the LHC housing the four main experiments at the interaction points.

hydrogen gas and are passed to the first stage of acceleration: a linear accelerator called the LINAC2 (50MeV). This is followed by the Proton Synchrotron Booster (PSB) (1.4 GeV), the Proton Synchrotron (PS) (26 GeV), and the Super Proton Synchrotron (SPS) (450 GeV), where they are finally transfered to the two LHC beam pipes to be accelerated independently in opposite directions to 4 TeV (3.5 TeV in 2010 and 2011, design centre of mass energy of 14 TeV).

The results presented in this thesis are based on events accumulated in 2011, when the LHC, running at a centre of mass energy,$\sqrt{s}$=7 TeV, delivered an integrated luminosity of 1.1 fb^{-1} to LHCb, which was collected with over 90% efficiency, as seen in Fig. 3.2.

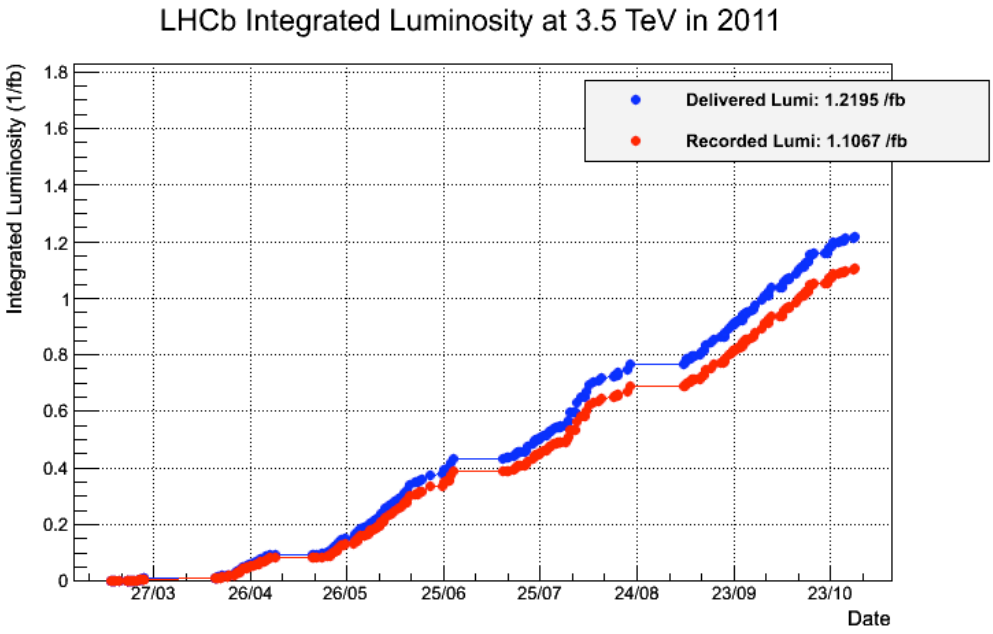

Figure 3.2: The integrated luminosity delivered by the LHC and recorded by LHCb during 2011

3.2 LHCb

With the $b\bar{b}$ cross section measured to be $\approx$ 280 μb [53] at $\sqrt{s}$=7 TeV, the LHC provides an excellent opportunity to perform studies in heavy flavour physics. In 1993, three different dedicated b physics experiments were presented to the LHC experiments Committee (LHCC): a forward Collider Beauty Experiment (COBEX) [54]), an internal Gas Jet Target experiment (GAJET) [55] and LHB, proposing a fixed target with an extracted beam [56]. It was suggested that the three collaborations merge and develop a plan for a new optimised detector, with the COBEX collider experiment being favoured over a fixed target experiment, as it resulted in a much higher ($\approx$ a factor 500) $b\bar{b}$ cross section. However, in order to benefit from this very high B meson production rate, a complex triggering system is required. The joint collaboration under the new name of LHC-B produced a Letter of Intent in 1995, [57] with the Technical Proposal following a few years later [58], and was approved in 1998 under the final collaboration name, LHCb. At this time, the B Factories were not yet in operation, and it was expected that LHCb would focus on making precision Standard Model (SM) measurements, especially in the B_s sector,

as the majority of the data collected at the B Factories was at an energy of $\Upsilon(4S)$. Since then, the B Factories have performed beyond expectations, producing many excellent results testing the SM, and the two Tevatron experiments, CDF and D0 have published many results in the B_s sector. As all parameters have, thus far, been measured to be consistent with the SM, focus at LHCb has shifted in searching for new physics (NP) beyond the SM.

The dominant production mechanism of B mesons in proton proton collisions is through gluon-gluon fusion. At LHC energies, the parton distribution functions are such that the partons interacting in the proton proton collisions have unequal energies, resulting in the $b\bar{b}$ pairs being produced in the same forward or backward cone from the interaction point, as seen in Fig. 3.3. This implies that the complete 4π coverage, required by the general purpose detectors, is unnecessary for heavy flavour physics. Instead, a more natural choice of detector layout is a forward spectrometer, as chosen for LHCb [59]. It is composed of various subdetectors laid along the direction of the beam pipe, a schematic of which can be seen in Fig. 3.4. The LHCb coordinate system is a right handed Cartesian coordinate system with the positive z axis pointing from the IP along the beamline, and the y axis pointing upwards. The direction of positive x points towards the side of the detector that is accessible in the cavern (A side) and away from the side with the LHC cryogenics (C side), *i.e* outside the LHC ring. The subdetectors, in increasing order of z from the interaction point are:

- Vertex Locater (VELO),
- Ring Imaging Cherenkov detector (RICH1).
- Trigger Tracker (TT),
- A warm dipole magnet,
- The tracking stations (T1-T3),
- RICH2,
- Calorimeters,
- Muon Stations.

More details will be given in the rest of this chapter.

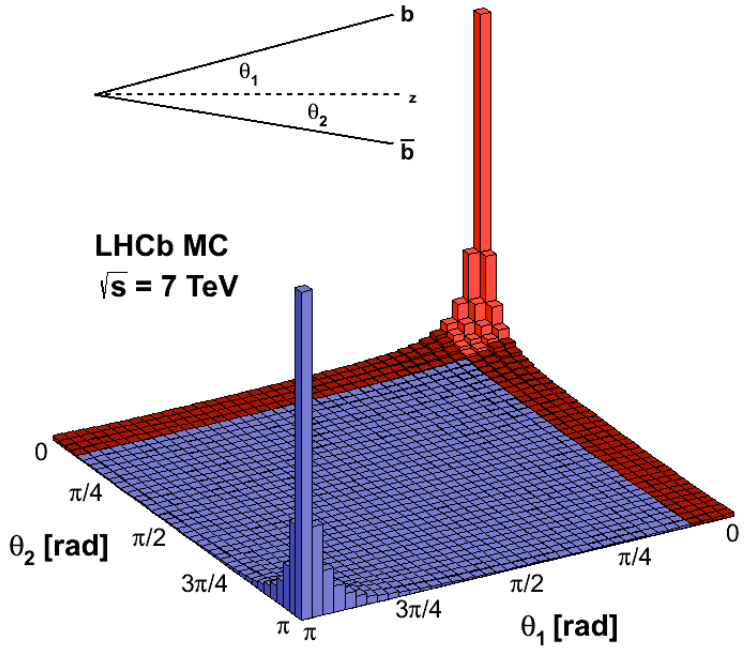

Figure 3.3: Correlation between the b and $\overline{b}$ quarks produced at the LHC for $s = \sqrt{7}$ TeV, created using PYTHIA8. The LHCb acceptance corresponds to the red bins: θ_1 and θ_2 <300 mrad. This covers ≈35% of the $b\overline{b}$ production.

3.2.1 Detector optimisation for performing flavour physics

Fig. 3.5 shows the B meson momenta from a simulation sample of $B \to \mathrm{K}^*\mathrm{e}^+\mathrm{e}^-$. A mean momenta measured to be 120 GeV and a mean lifetime of 1.5 ps corresponds to a decay length of around 1 cm in the lab frame. This gives a clear signature for a typical b event, and requires precision tracking and vertexing of not only the primary vertex (PV) but the secondary vertex (SV). In a hadron collider environment, many tracks are produced with each proton proton collision. In order to facilitate the correct identification of a track to a vertex, it is desirable to have only one proton proton collision per bunch crossing, which requires running at a lower instantaneous luminosity than ATLAS or CMS. By the end of 2011, LHCb ran with a maximum instantaneous luminosity of $4 \times 10^{32}\mathrm{cm}^{-2}\mathrm{s}^{-1}$ giving an average of 1.4 proton proton interactions per bunch crossing, whereas ATLAS and CMS went

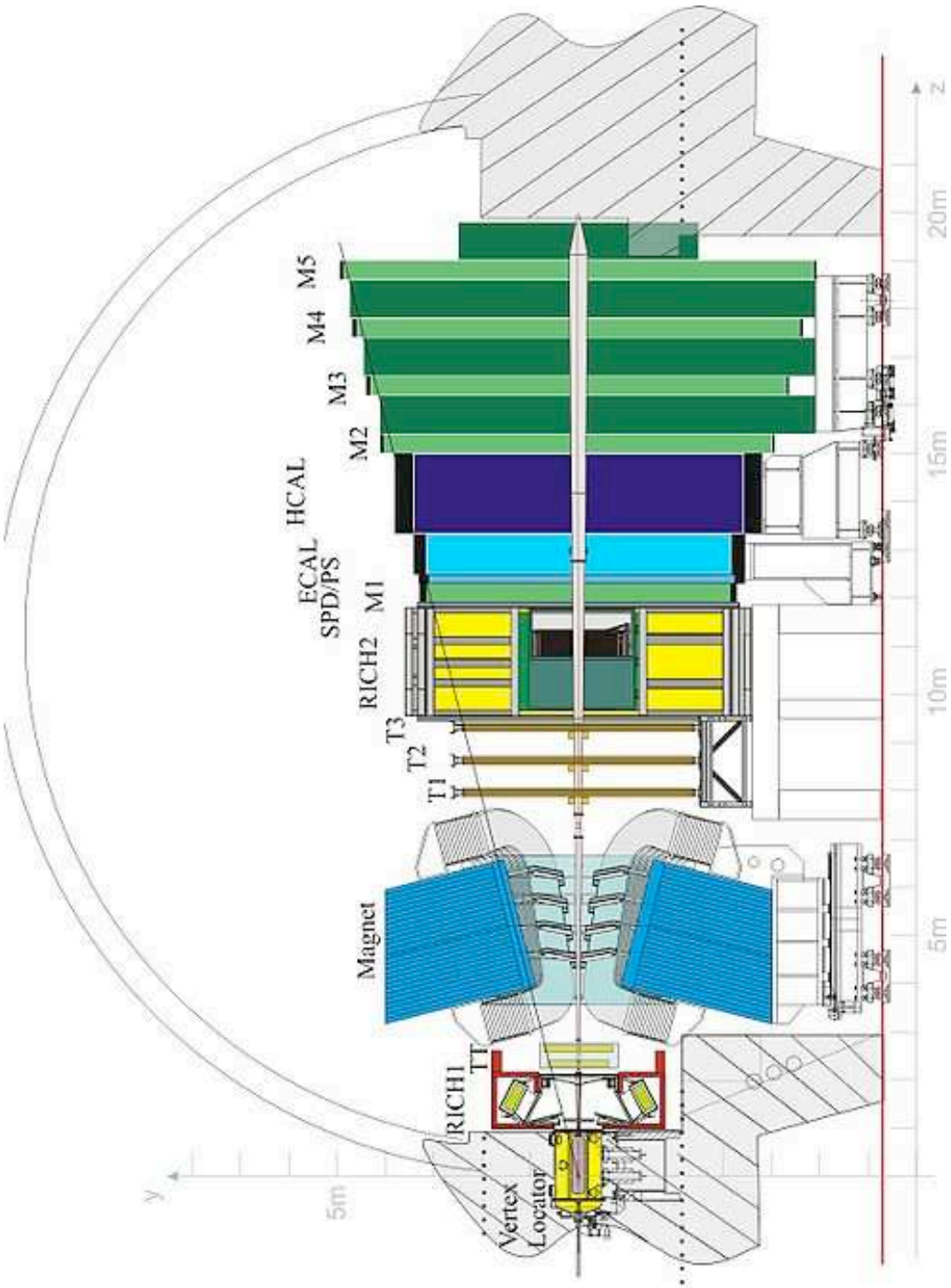

Figure 3.4: Schematic view of the LHCb detector [59].

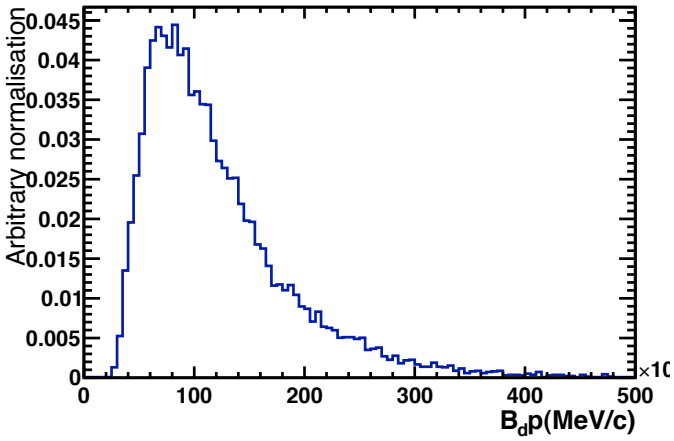

Figure 3.5: Momenta of B mesons decaying through the channel $B \to K^* e^+ e^-$, from Monte Carlo simulation.

up to $3.65 \times 10^{33} \text{cm}^{-2}\text{s}^{-1}$ and 25 proton proton interactions per crossing. This is still twice the instantaneous luminosity that LHCb was designed for, but the trigger and reconstruction software have been adapted, and show good performance beyond the original specifications and despite the harsh environment. The LHC provides different instantaneous luminosities by reducing the focus of the beams at LHCb compared to the GPDs, and via a process called luminosity leveling. By offsetting the two colliding beams in the vertical plane at the LHCb interaction point, the instantaneous luminosity is reduced. This separation is automatically varied as the beam degrades throughout the run, allowing for the delivery of constant luminosity to LHCb, as opposed to at ATLAS and CMS as can be seen in Fig. 3.6. This has the added advantage of providing stable operational conditions throughout the whole fill.

Key requirements for the analysis of flavour physics are an excellent vertex and tracking reconstruction, good particle identification performance and an efficient trigger, each of which will now be described in turn.

3.2.2 Vertex detection and the tracking system

As already mentioned, the flight distance of a B meson and its subsequent decay is one of its key signatures, and requires excellent vertex resolution in order to suppress minimum bias (*i.e.*, inelastic pp collisions) background for optimal signal

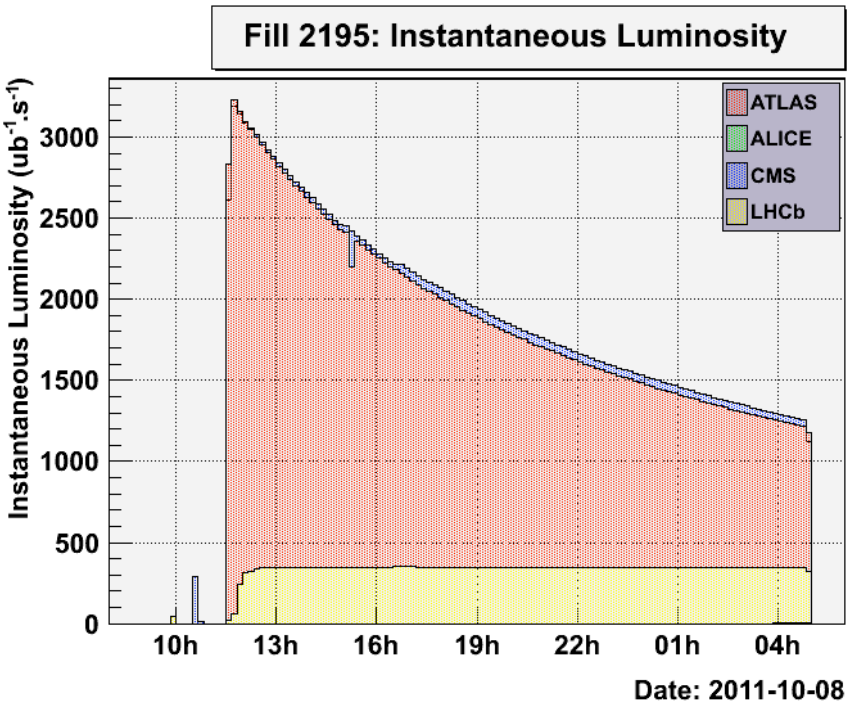

Figure 3.6: An example of the instantaneous luminosity as a function of time for ALICE,ATLAS, CMS and LHCb during one fill in 2011.

efficiency. It is also necessary for the precise reconstruction of the hadron proper time. Background suppression also necessitates that the tracking system provides a good momentum resolution, which is also required for good mass resolution. It must be able to perform well despite the high occupancy in the forward direction, and also must be able to cope with the bunch crossing separation of 25 ns. The tracking system consists of the VELO, the magnet, the trigger tracker (TT), the inner (IT) and the outer tracker (OT).

3.2.2.1 The Vertex Locator: VELO

Vertex reconstruction is performed by software using information from VELO, a silicon strip detector lying close to the beamline, thereby allowing for the precise reconstruction of the primary vertex and the secondary vertices. It has the highest position resolution out of all of the four main experiments on the LHC.

It consists of 21 modules, each of which has two semi-circular silicon sensor which are positioned along and perpendicular to the beam axis over a distance of

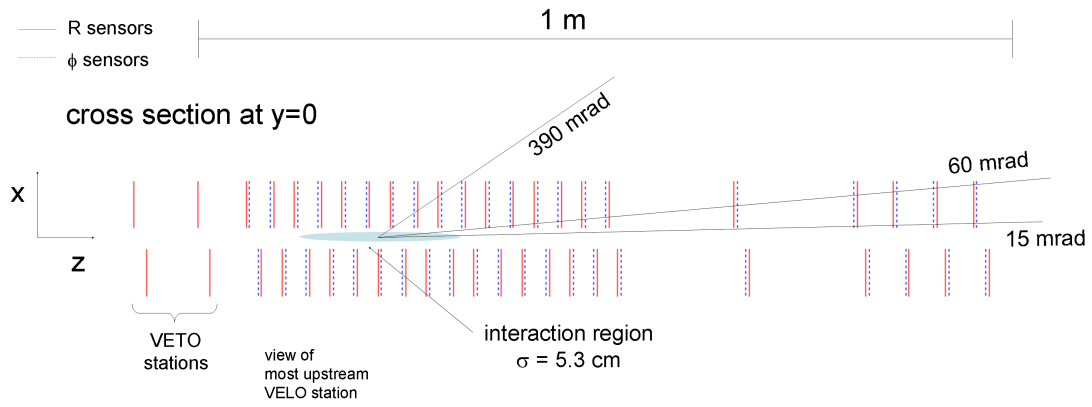

Figure 3.7: Cross section showing the layout of the VELO sensors and the pileup modules. The ϕ and R sensors are marked in blue and red, respectively.

approximately 1m. One sensor provides measurements in the r coordinate, and the other in the ϕ coordinate, with the cylindrical coordinate system chosen to increase the speed of reconstruction in the trigger. In addition, there are two pile-up stations placed upstream of the interaction point, used to quickly determine the number of primary vertices in the event for the Level-0 (L0) trigger. The layout is shown in Fig. 3.7.

Each sensor has an active internal radius of $\approx 8\,\text{mm}$, optimised to provide information as close to the beam line as possible without suffering from radiation damage in this high occupancy region of the detector, and an external radius of 42 mm. As the LHC beam sectional area increases during injection, the two halves are completely retracted, (see Fig. 3.8 for the cross section in the xy-plane, and are retracted by 3 cm during injection in order to avoid radiation damage. To optimise data taking efficiency, the closing procedure is now performed automatically by monitoring the beam positions once the LHC beams are declared stable.

In order to be as close to the beamline as possible, the VELO is placed within the LHC vacuum. In order to protect the main vacuum, it is contained within a secondary vacuum by a thin walled corrugated aluminum sheet, chosen to keep to a minimum the amount of material in the detector acceptance. This also protects the VELO from the high frequency fields caused by the beams. The shape of the foil allows each half of the VELO detector to overlap, providing a gapless measurement in ϕ and aiding with alignment. A schematic showing the shape of the foil is shown

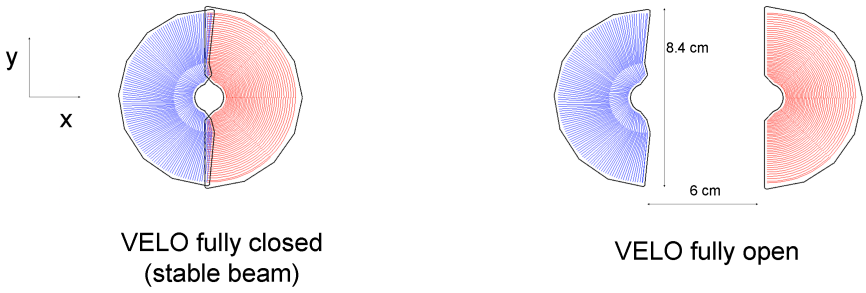

Figure 3.8: The front face of a module in the closed and open position.

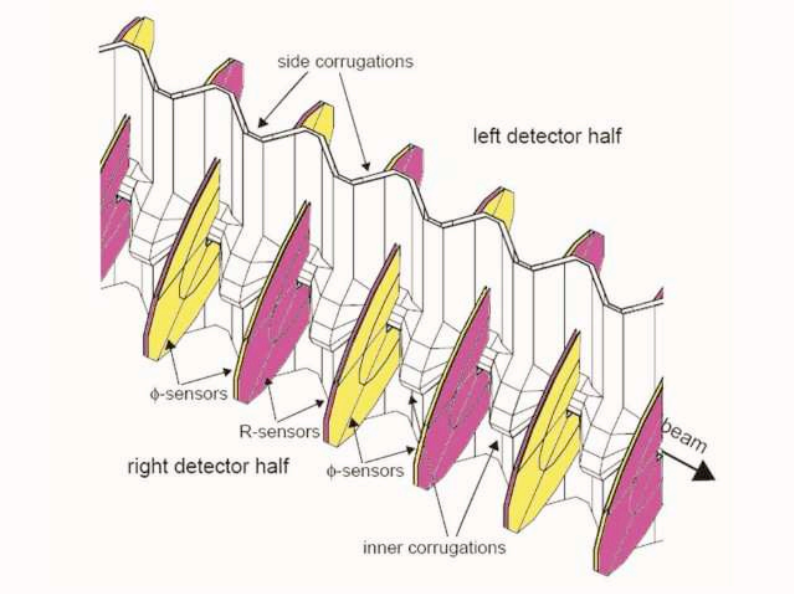

Figure 3.9: A close up of the VELO in its closed position with respect to the RF foil.

in Fig. 3.9.

The performance of the VELO is reflected in the measured resolution of the impact parameter, (IP), defined as the perpendicular distance between a vertex and a track, an important variable used in the LHCb trigger. The IP resolution as a function of $1/p_{\mathrm{T}}$ for 2011 data and Monte Carlo (MC) is shown in Fig. 3.10(a). The resolution at high p_{T} is well described by the MC. The most probable cause of the small remaining discrepancy between data and MC is thought to be related to the material description in the MC, but is still under investigation.

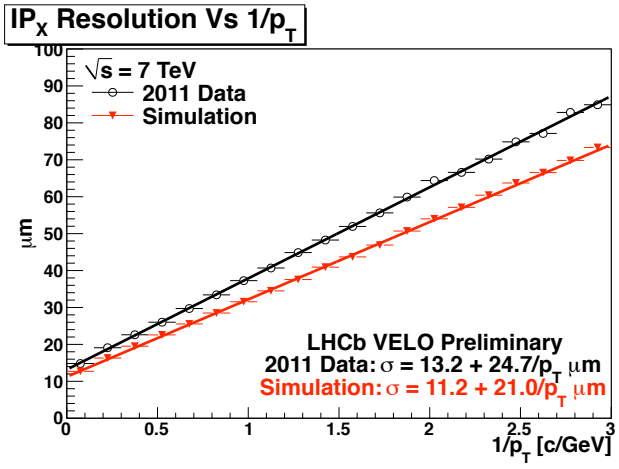

(a) σ_{IP} as a function of $1/p_{\mathrm{T}}$

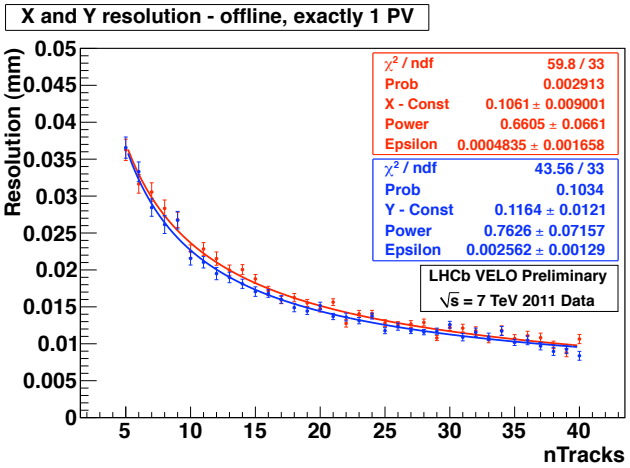

(b) σ_{PV} as a function of the number of tracks

Figure 3.10: The resolution in x of the impact parameter as a function of $1/p_{\mathrm{T}}$ for the 2011 data compared to MC(3.10(a)). The resolution in x (red) and y (blue) of the primary vertex as a function of the number of reconstructed tracks, for events containing one PV (3.10(b)).

3.2.2.2 The LHCb magnet

The magnet, shown in Fig. 3.11, was designed with the aim of providing a good momentum resolution and thus a high magnetic field covering the tracking system, but with a low field in the region of the RICH. A warm dipole magnet was chosen over a superconducting magnet in order to reduce construction costs and time constraints. Its magnetic field has an amplitude of 1 T, and an integrated value of 4 Tm over

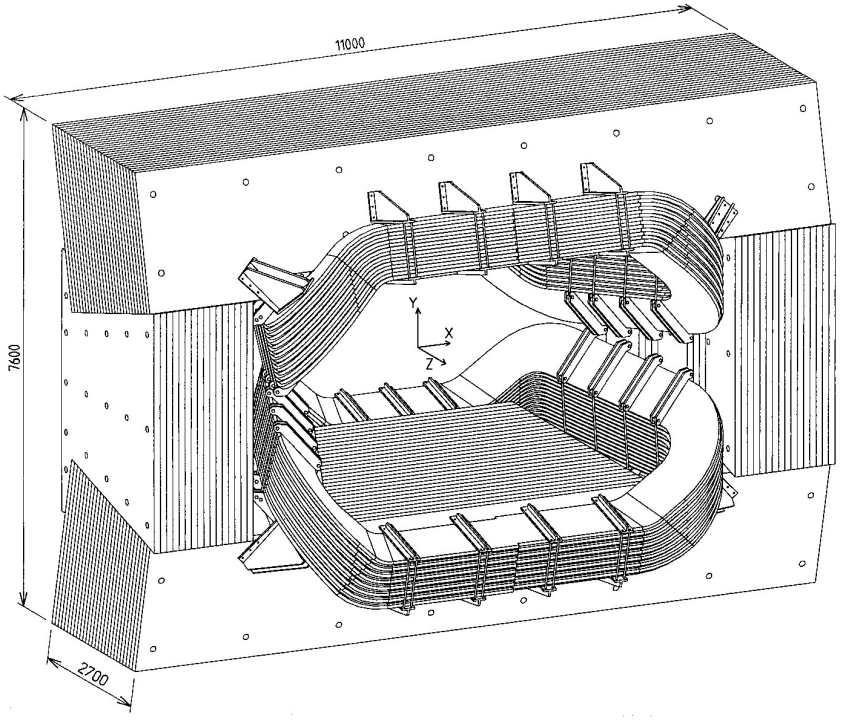

Figure 3.11: The LHCb dipole magnet, and its supporting infrastructure. The dimensions shown are given in mm

a length of 10 m. Choosing a dipole magnet also allows for the magnetic field to be regularly reversed, in order to minimise systematic uncertainties due to detector asymmetries or an inhomogeneous magnetic field.

3.2.2.3 The silicon tracker

The silicon tracker (ST) is the collective name given to the trigger tracker (TT) which is between RICH 1 and the LHCb magnet, and the inner tracker (IT), located downstream of the magnet. Single planes of the silicon tracker are illustrated in Fig. 3.12. They both share the same silicon strip technology with a strip pitch of ≈ 200 μm. Each of the ST stations has four detection layers, the first and last are oriented vertically to measure x, and are hence called x layers, with the u and v layer in between rotated by a stereo angle of +5 deg and -5 deg respectively to allow for the measurement of the transverse momentum.

The TT covers the whole detector acceptance, and provides fast measurement of the momentum to be used in the trigger. TT also allows the reconstruction of

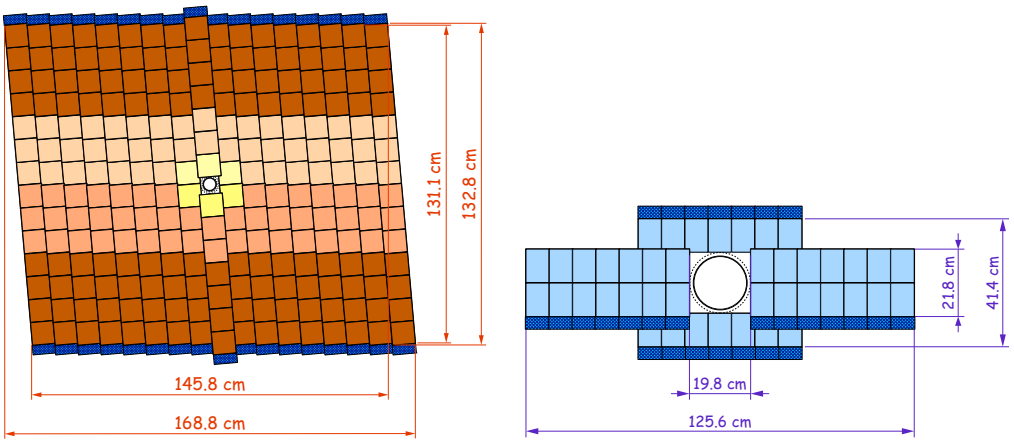

(a) TT (b) IT

Figure 3.12: Schematic view of the v TT layer 3.12(a) and the x IT layer 3.12(b).

long-lived particles that decay outside of the VELO, for example, the K_S.

The IT on the contrary, does not encompass the whole LHCb acceptance, but the high occupancy region around the beampipe where the radiation and multiplicity are too high to allow for a drift time detector, with the remaining acceptance covered by the OT. The IT is divided into three stations, labeled T1-T3, each of which have four detector boxes, and each with the four layers as described above. The detector boxes are placed around the beamline and overlap to facilitate the alignment and to ensure complete acceptance.

The OT is a time-drift detector with three stations in the same plane as those of the IT, and with the same four layer layout. Each layer is composed of two dense overlapping planes of straw tubes filled with a 70% mixture of Argon, and 30% CO_2, which provides drift times under 50 ns, necessary to avoid spillover over more than two bunch crossings.

3.2.3 Track reconstruction

There are several different types of track defined at LHCb, as illustrated in Fig. 3.13. The track reconstruction is provided by a series of algorithms, which determine the track type based on the combination of information from the subdetectors. The definitions of the track type are as follows:

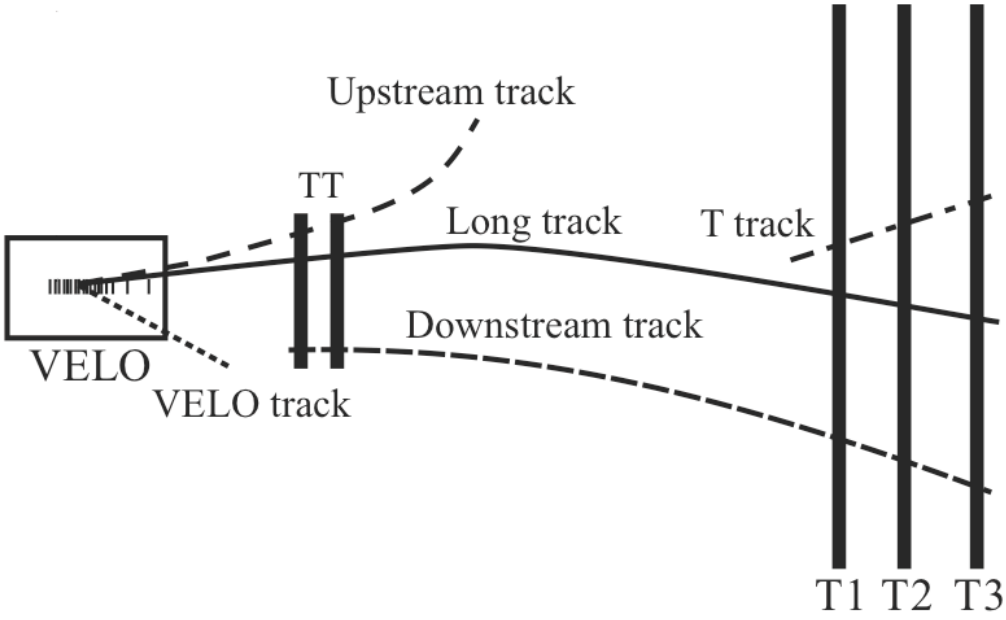

Figure 3.13: Schematic of the definitions of track types at LHCb

- **Long tracks,** traverse the whole tracking system, from the VELO to the T stations, and consequently provide the best momentum resolution, and are the most common track type used in physics analysis. All tracks studied in the analysis presented here are long tracks.
- **Downstream tracks**, are first detected at the TT. These are useful to study K^0_S and Λ particles, which may decay outside of the active VELO region.
- **Upstream tracks** exit the detector acceptance after the TT. Although these are reconstructed with less quality than long tracks, they give information on low momentum particles, which are swept out of the acceptance by the magnet. These are used to perform studies in RICH1.
- **VELO tracks** only have VELO information, and are used in reconstruction of the primary vertices.
- **T tracks** are first detected at T1, usually having been produced in secondary interactions. They are used in global pattern recognition in RICH2.

The reconstruction strategy for long tracks is based on what is known as *seeding*, by searching for track seeds in the region where the magnetic field is weakest, and can

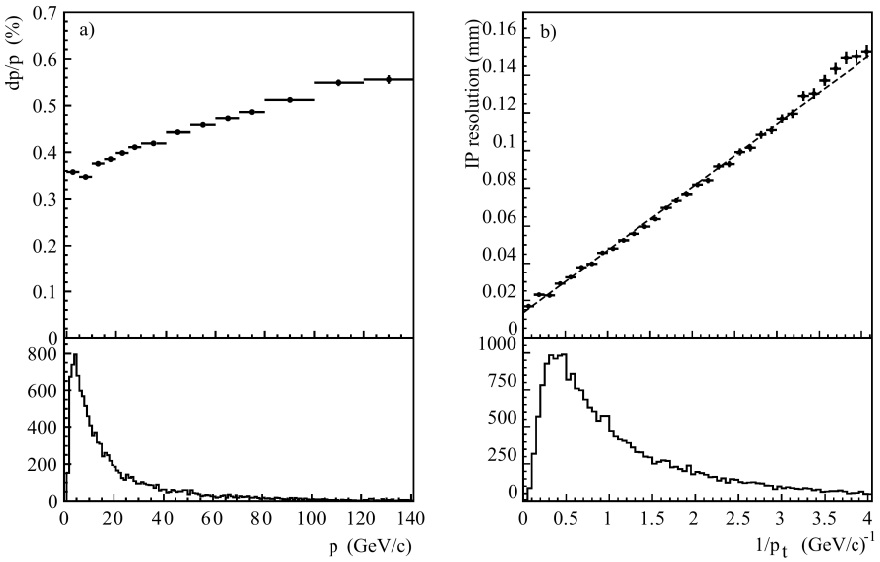

Figure 3.14: Resolution on the reconstructed track parameters at the production vertex of the track according to simulation: the momentum resolution (left) and the impact parameter resolution (right) as a function of p and $1/p_T$, respectively.

be reconstructed as straight line segments. Two strategies are then employed, the first starts with VELO seeds and propagates it through the magnetic field to match with hits in the tracking stations. The second works backwards, taking tracking seeds, and propagating backwards to match with VELO tracks. TT hits close to the resulting tracks to increase the momentum resolution and reduce the number of fake tracks. The tracks are fit with a bidirectional Kalman Filter, which takes into account energy loss and multiple scattering.

The tracking system has an average track efficiency of 95%, and a momentum resolution $\Delta p/p$=0.4% for 5 GeV/c tracks to $\Delta p/p$=0.6% for 100 GeV/c tracks. This is close to expectations, shown in Fig. 3.14.

3.2.4 Detectors used for particle identification

A number of B decays are topologically identical and thus indistinguishable without particle identification. Moreover, good π-K separation is needed to perform

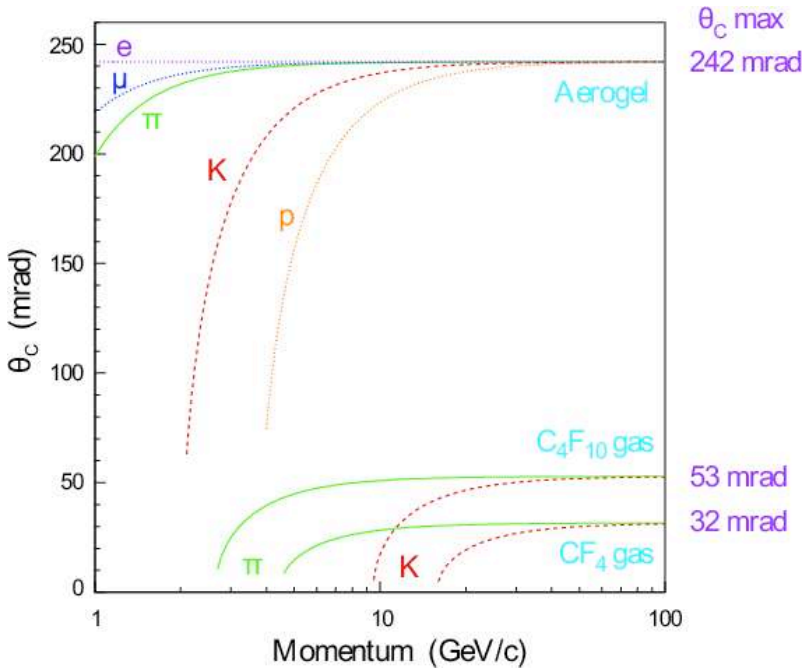

Figure 3.15: Cherenkov angle versus particle momentum for the RICH radiators

flavour tagging of the B meson. The particle identification is performed by combining information from the Cherenkov detectors, the calorimeters, and the muon chambers.

3.2.4.1 Ring Imaging Cherenkov (RICH) detectors

The identification of hadrons is achieved by measuring the particle mass using two Ring Imaging Cherenkov, (RICH) detectors. Cherenkov light is produced when charged particles travel with a speed greater than the speed of light in the medium, resulting in a characteristic cone with opening angle θ_C according to

$$cos(\theta_C) = \frac{1}{n\beta} \tag{3.1}$$

where n is the refractive index of the material and β is the velocity of the charged particle. Hence, the particle mass can be calculated by measuring the opening angle of the Cherenkov light cone and the track momentum. In order to cover the whole momentum range of 1 GeV/c to 100 GeV/c, two RICH detectors are used (see Fig. 3.15), with three different radiator media with differing refractive indices. Both

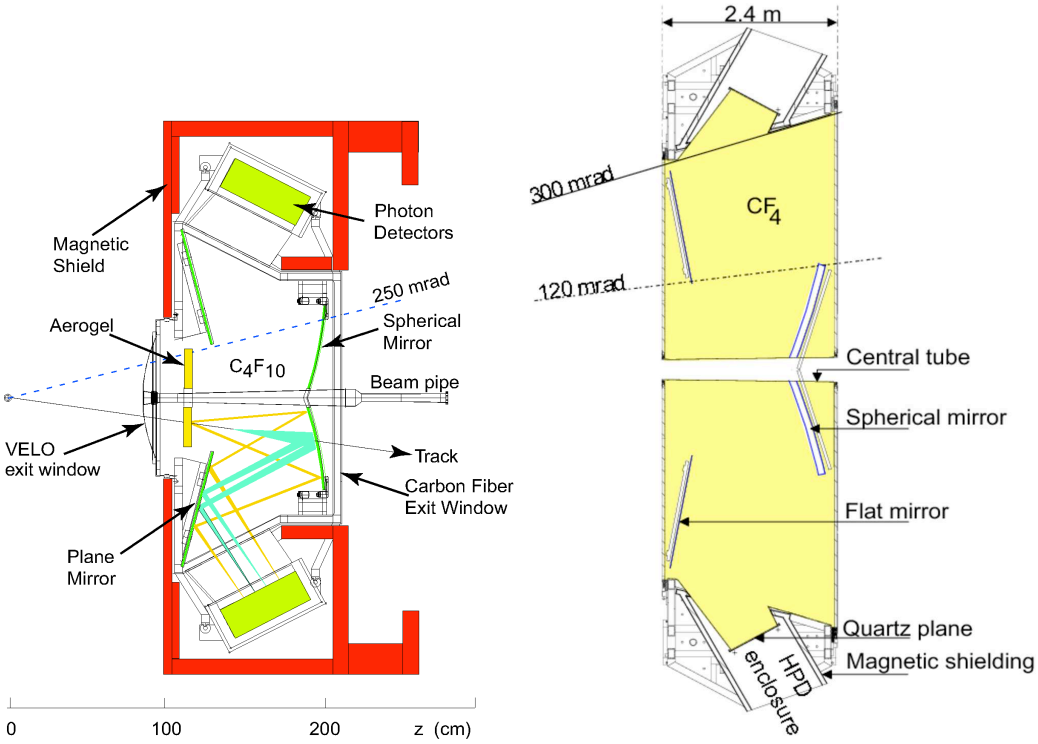

Figure 3.16: Schematic view of RICH1 (left) and RICH2 (right).

RICHs operate by reflecting the Cherenkov light with two plane mirrors and guiding it to photon detectors, which are placed outside the acceptance. For a schematic layout of the RICH detectors, refer to Fig. 3.16. RICH 1 is located upstream of the magnet, immediately after the VELO, and it covers the low momentum range, [1-40] GeV/c over the whole LHCb acceptance. It has two radiator materials, aerogel (n=1.03) and C_4F_{10} gas (n=1.0014). The RICH2 is located downstream of the magnet. It is designed to separate charged particles with high momentum, from 15 GeV/c to beyond 100 GeV/c, so it has a limited angular acceptance of approximately 15 mrad to ± 200 mrad in the bending plane, and ± 100 in the non bending plane, (*i.e.* the region where high momentum particles are located.)

3.2.4.2 The calorimeters

As can be seen in Fig. 3.15, the discrimination power of the RICH to separate $e^{\pm}$, $\mu^{\pm}$ and $\pi^{\pm}$ is limited to the very low momenta region, less than 3 GeV/c. The calorimeters are therefore vital to perform the electron and photon identification

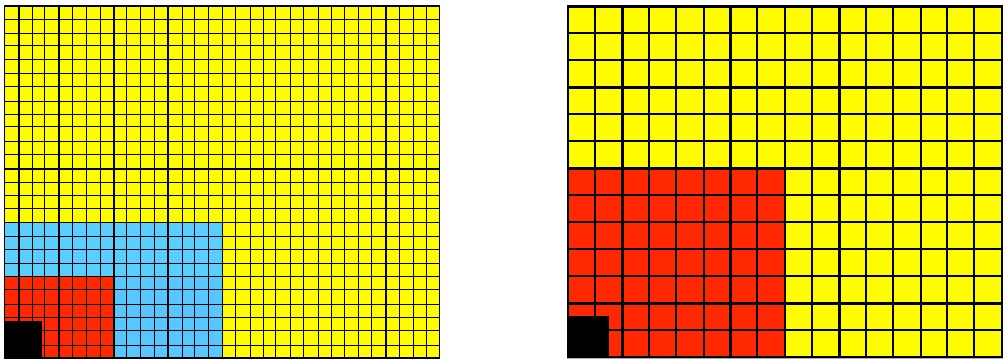

Figure 3.17: One quarter of the detector front face is showing the lateral segmentation of the SPD, PS and ECAL (left) and HCAL (right).

necessary for the analysis of this thesis. They also provide some information for hadron identification, and are used to measure particle energy and position. They are critical to the first stage of the trigger (L0), providing high transverse energy hadron, electron and photon candidates. The calorimeter system is composed of the scintillator pad detector (SPD), the preshower detector (PS), the electromagnetic calorimeter (ECAL) and the hadronic calorimeter (HCAL). All subsystems have variable lateral segmentation, as shown in Fig. 3.17, as the occupancy varies by two orders of magnitude over the plane of the calorimeter surface, with three levels of granularity in the ECAL, which are projected to be the same angular size for the SPD/PS, and two in the HCAL.

All the subsystems also work via the same principle. Scintillating light is carried by wavelength-shifting fibres to photomultiplier tubes.

SPD/PS detector

The use of the calorimeters in the first stage of the trigger imposes several design constraints. It must be able to provide electromagnetic candidates in an environment with high amounts of pion background within 25 ns. This is achieved via the measurement of the longitudinal profile of the electromagnetic showers in the ECAL and HCAL and the PS, which is placed after a 15 mm lead absorber equivalent to 2.5 X_0 (radiation lengths) and in front of the ECAL. Charged hadrons can be separated from electromagnetic particles due to the difference in their interaction length. The SPD is located just before the lead absorber, and as it is sensitive to charged particles, it is used to separate electrons from neutrals

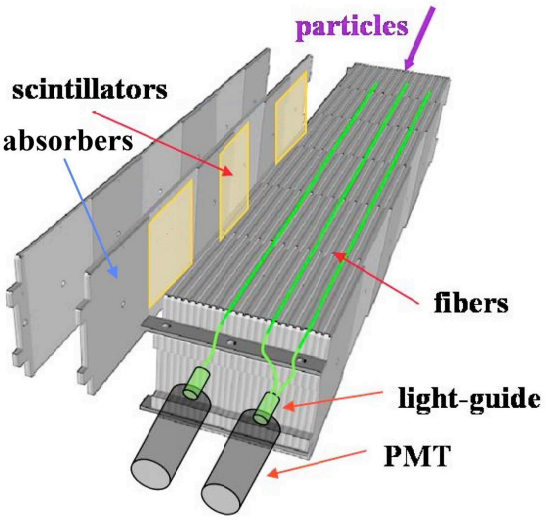

Figure 3.18: Schematic of a module of the HCAL.

(π^0 and photons) before showering. It is also used to provide an estimate of the number of tracks at the first level of the trigger, and thus to veto high pile-up events.

ECAL

For optimal energy resolution, the ECAL is designed to fully contain the EM showers from high energy photons, and thus has a thickness of 25 X_0. It is a sampling calorimeter using 'sashlik' technology, made up of layers of lead and a scintillating polystyrene. Its design energy resolution is $\frac{\sigma(E)}{E} = \frac{10\%}{\sqrt{E}} \otimes 1\%$ where the first term comes from statistical fluctuations in the shower, and the second is from systematic uncertainties due to the calibration procedure. Due to the high radiation close to the beampipe, the calorimeter has a smaller inner acceptance than the tracking system, with the sensitive region starting at $\theta_{y,x} > 25$ mrad. The calorimeters have been found to be susceptible to the effects of aging, affecting the trigger rates, and at different rates for different regions. Calibration is therefore performed routinely to correct for this.

HCAL

The HCAL is a sampling calorimeter, composed of iron and scintillating tiles. It is oriented differently from the ECAL, with the scintillating tiles running parallel to the beamline (refer to Fig. 3.18 to see the structure of the modules). It also

has coarser granulation than the ECAL, due to the larger transverse development of hadronic showers. As it is primarily used in the trigger, and due to space limitations, it was built with a thickness of 5.6 X_0 and thus does not contain the whole hadronic shower. Its design resolution is therefore $\frac{\sigma(E)}{E} = \frac{80\%}{\sqrt{E}} \otimes 10\%$.

3.2.5 Electron identification

The energy deposited in the calorimeter cells are clustered together using a 'cellular automation procedure' [60]. This algorithm finds a local maxima, and then adds neighboring cells in an iterative process.

The basic ECAL estimator, χ^2_e, is then constructed via a global matching procedure between reconstructed tracks, and these clusters in the calorimeter [61]. The procedure includes in particular, the balance of the energy of the cluster and the track momentum (see Fig. 3.19(b)) and matching between the barycenter of the cluster, and the position of the track when extrapolated to the calorimeter plane. The distribution of this χ^2_e is shown in Fig. 3.19(a). Another estimator is provided by Bremsstrahlung photons that are emitted before the magnet, and thus have positions that are predicted from the extrapolation of track segments. Furthermore, the PS and HCAL also provide information to discriminating information, as demonstrated in Fig. 3.20. This provides four estimators, χ^2_e, $\chi^2_B rem$ and the energy of the PS and HCAL, all of which are combined with the identification information from the RICH to provide a global log-likelihood for the electron hypothesis.

3.2.6 The muon chambers

The muon system consists of five stations, labeled M1-M5. Due to their low interaction probability, muons are the only charged particles likely to traverse the whole detector material. The muon system is thus placed behind the calorimeters (M2-M5) with the exception of M1, which is located before the SPD to provide an improved p_{T} measurement for the trigger. A schematic of the layout can be seen in Fig. 3.21(a). As with the calorimeters, the readout cells increase in size with distance from the beampipe, as shown in Fig. 3.21(b), in order to provide a steady channel occupancy, across the acceptance. They consist of multiwire proportional chambers, with M1 also using Gas-Electron Multiplier detectors in the inner most

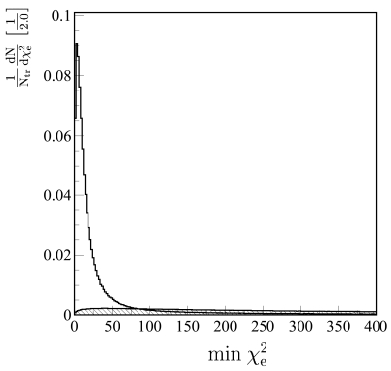

(a) The minimum value for χ^2_e estimator.

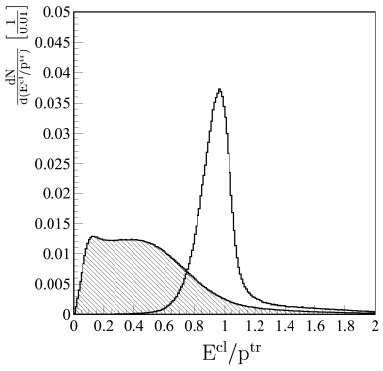

(b) The ratio of energy of the cluster and the track momentum.

Figure 3.19: Variables used for electron identification shown MC electrons (open histogram) and hadrons and muons (hatched histogram) according to MC. Histograms taken from Ref. [61].

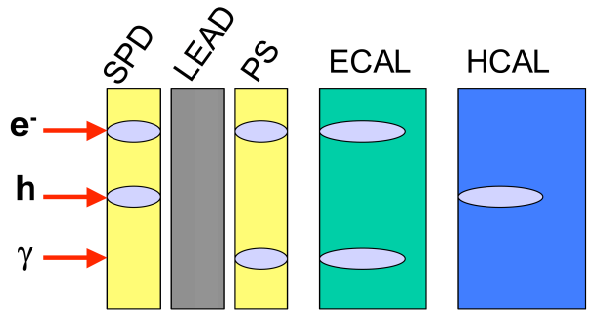

Figure 3.20: Schematic showing the expected energy deposition in the calorimeter system for electrons, hadrons and photons. Diagram taken from Ref. [62].

region. The stations are interspersed with 80cm iron absorbers, leading to 20 interaction lengths to M5 (including the calorimeters). This corresponds to a minimum required muon p of 6 GeV/c to traverse the whole detector.

3.2.7 The trigger

At the interaction point of LHCb, the bunch crossing rate is 40 MHz. A complex sophisticated trigger is required to quickly select the interesting events and reduce

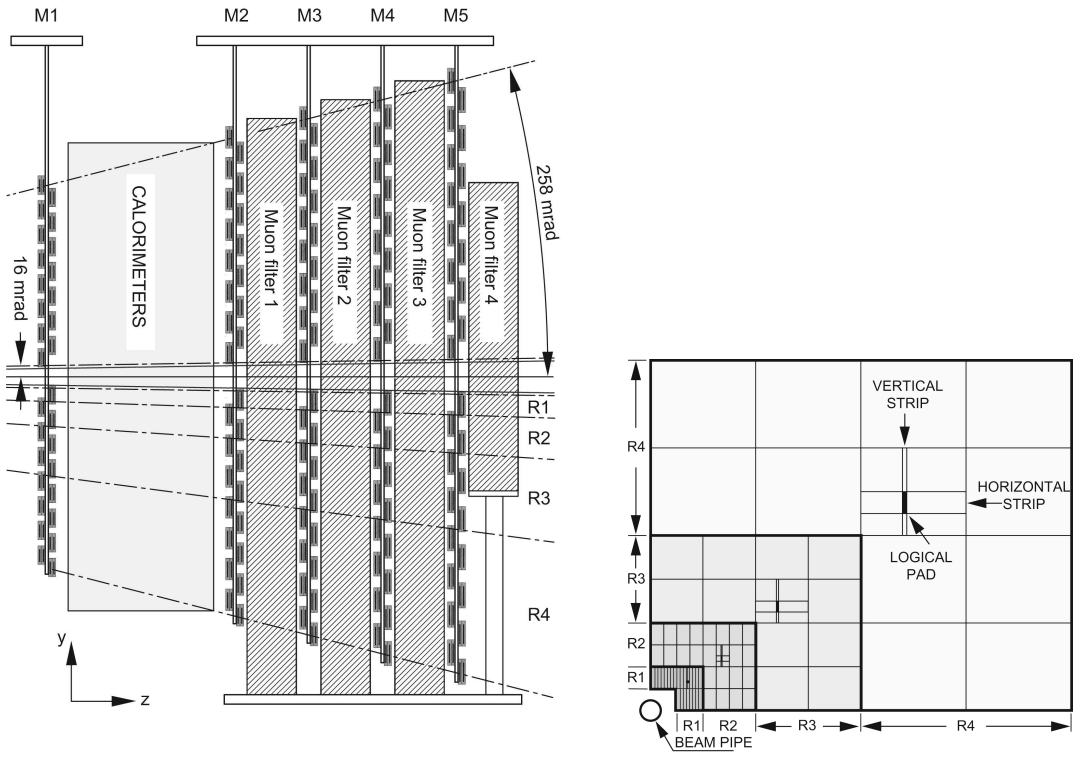

Figure 3.21: Schematic of the five muon stations 3.21(a) and the x IT layer 3.12(b) and one quadrant of the M2 station showing the sensitive regions R1-R4 in which the channel density successively halves outwards from the beampipe 3.21(b). Each rectangle represents one chamber

this to the rate that can be stored, of a few kHz. The trigger must also be flexible in order to adapt to different running conditions.

This is done in two main stages. First, is the L0 trigger: a hardware trigger operating synchronously with the 40 MHz bunch crossing frequency, which reduces event rates to 1 MHz, at which the whole detector can be readout. Next is a software High Level Trigger (HLT), which further reduces the event rate to 3 kHz to be stored to tape. It is split in two levels: HLT1 uses partial reconstruction, and HLT2 is able to perform full event reconstruction.

3.2.7.1 L0 Trigger

The L0 trigger is designed to select $b\bar{b}$ events whilst rejecting minimum bias. Signatures of b hadron decays include high p_{T} particles of the order of several GeV/c.

Thus, the calorimeter system selects high E_{T} candidates by summing the energy over 2x2 clusters in the ECAL and HCAL and selecting those with the highest energy. Information from the PS/SPD, ECAL and HCAL is combined in order to tag the candidates as electrons, photons or hadrons. A threshold is then placed on the E_{T}: 3500 MeV for hadron candidates, and 2500 MeV for photon and electron candidates, during 2011. A limit of less than 600 hits in the SPD was also applied, in order to reduce busy events that would saturate the HLT computing farms.

Single and dimuon candidates are formed by finding the two highest p_{T} muon tracks that go through the muon stations and point towards the interaction point, in each quadrant of the muon chamber.

3.2.7.2 High Level Trigger (HLT)

The HLT is split into two levels, as the high output rate from the L0 trigger and the available computing power in the Event Filter Farm does not allow for the immediate use of the full detector information.

HLT1

The strategy of the first stage of the HLT1 is to perform an inclusive selection looking for single tracks originating from b hadrons. It is based on the assumption that most b decays have at least one high momentum track with a large IP with respect to all primary vertices in the event, and a good track fit quality. This differs from the original strategy of confirming L0 candidates, and allows for all L0 candidates, regardless of how they were triggered, to be used as input for HLT1. The one track trigger strategy was found to be more efficient, and more stable in terms of time and retention rate, with varying running conditions. Busy events that would saturate the HLT are rejected by using 'Global Event Cuts' on the number of clusters in the VELO, OT and IT. The HLT1 reduces the rate to ≈ 50 kHz.

HLT2

At 50 kHz, it is possible to perform a close to offline reconstruction using tracks that have p_{T} >500 MeV/c and p >5000 MeV/c, thus allowing for both more channel specific lines, and inclusive selections. In 2011, around a third of the trigger bandwidth was given to an inclusive topological trigger, searching for generic n-body B decays. The B candidate is corrected for missing p_{T}, in order to allow

for missing daughter particles, even with a relatively tight HLT2 selection. In 2011, the selection was based on a Boosted Decision Tree, performing a multivariate selection based on parameters such as the flight distance χ^2 of the B candidate, daughter p_{T} and the sum of the IPχ^2 of the daughters. The efficiency of HLT2 for B decays with more two, three or four tracks is more than 80% [63], and the rate is successfully reduced to a few kHz.

Chapter 4

Measurement of the ratio of branching fractions

Contents

Despite the challenging nature of performing analyses with low $p_{\rm T}$ electrons in a hadronic environment LHCb has collected the largest sample of $B^0 \to K^{*0}e^+e^-$ to date. Although the angular analysis can not be carried out with the present statistics collected at LHCb,it is useful to measure the branching fraction in the dilepton mass range of 30 MeV/c^2 to 1 GeV/c^2 in order to gain confidence in the

analysis strategy and to validate our understanding of the detector, particularly with regards to electrons.

The following sections describe the measurement of the $B^0 \to K^{*0}e^+e^-$ branching ratio with respect to that of $B^0 \to J/\psi\, K^{*0}$ with the J/ψ decaying into two electrons, based on the analysis of 1 fb^{-1} of LHCb data with a centre of mass energy of $\sqrt{s} =$ 7 TeV, collected in 2011.

4.1 Current status

The only experiments to have observed $B^0 \to K^{*0}e^+e^-$ to date are BaBar [64] and Belle [65], which have collected $\mathcal{O}$ (30) $B^0 \to K^{*0}\ell^+\ell^-$ events, in q^2 ranges of $<2\,\text{GeV}^2/c^4$, summing over final state electrons and muons. The measurements of the $B^0 \to K^{*0}e^+e^-$ branching fractions are dominated by the statistical uncertainty, and no measurement is currently available in the q^2 region optimal for the angular analysis proposed here. A summary of experimental measurements of the branching fractions available from the B Factories can be seen in Table 4.1.

Experiment	Decay mode	q^2 (GeV$^2/c^4$)	N_s	$\mathcal{B}(10^{-7})$
BaBar	$B^0 \to K^{*0}\ell^+\ell^-$	total	NA	$10.2^{+1.4}_{-1.3} \pm 0.5$
	$B^0 \to K^{*0}\ell^+\ell^-$	0.10-2.00	$26.0^{+7.1}_{-6.4}$	$1.89^{+0.52}_{-0.46} \pm 0.06$
Belle	$B^0 \to K^{*0}e^+e^-$	total	NA	$11.8^{+2.7}_{-2.2} \pm 0.9$
	$B^0 \to K^{*0}\ell^+\ell^-$	0.00-2.00	$27.4^{+7.4}_{-6.6}$	$1.46^{+0.40}_{-0.35} \pm 0.11$

Table 4.1: Summary of the relevant results from the B Factories. NA signifies that the number is not available in the published material. For Belle, the lower limit on the dielectron mass is 140 MeV/c^2.

4.2 Theoretical prediction

The expected $B^0 \to K^{*0}e^+e^-$ rate can be calculated with respect to the $B^0 \to K^{*0}\gamma$ branching fraction. Following, [34]:

$$\mathcal{B}_{\text{Vis}}(B^0 \to K^{*0}e^+e^-)^{q^2_{\text{max}}} = \mathcal{B}(B^0 \to K^{*0}\gamma) \times \frac{\alpha}{3\pi} ln((\frac{q^2_{\text{max}}}{(2m_e)^2})) \tag{4.1}$$

and so, for the dilepton mass range, [30-1000] MeV/c^2, and using taking the PDG central value, $\mathcal{B}(B^0 \to K^{*0}\gamma)$=4.33×10^{-5},

$$\begin{aligned}\mathcal{B}_{\rm Vis}(B^0 \to K^{*0}e^+e^-)^{30-1000\,{\rm MeV}/c^2} &= \mathcal{B}(B^0 \to K^{*0}\gamma) \times \frac{\alpha}{3\pi} ln((\frac{1000}{30})^2) \\ &= 2.35 \times 10^{-7}\end{aligned} \tag{4.2}$$

A factor, $\frac{1}{1-\langle F_L \rangle}$, where $\langle F_L \rangle$ is the fraction of longitudinal polarisation of the K^{*0}, should also be included, to take into account that there is no longitudinal term in $B^0 \to K^{*0}\gamma$. Taking $\langle F_L \rangle$ to be 19%, as found from the $(B^0 \to K^{*0}e^+e^-)^{30-1000\,{\rm MeV}/c^2}$ Monte Carlo (MC), gives:

$$\begin{aligned}\mathcal{B}_{\rm Vis}(B^0 \to K^{*0}e^+e^-)^{30-1000\,{\rm MeV}/c^2} &= 2.35 \times 10^{-7} \times 1.23 \\ &= 2.9 \times 10^{-7}\end{aligned} \tag{4.3}$$

It should be noted that this prediction only includes the contributions from the electroweak penguin diagrams. Including the other contributions gives an extra correction of approximately 7%.

4.3 Analysis Strategy

$B^0 \to J/\psi(e^+e^-)K^{*0}$ has the same final state and similar topology as $B^0 \to K^{*0}e^+e^-$. As seen in Table 4.2, its branching ratio is very well measured, owing to the fact that it is of the order of 275 times larger than the predicted $B^0 \to K^{*0}e^+e^-$ branching fraction in the dilepton mass range of interest. It is therefore used as a control channel, such that by measuring the ratio of branching fractions, systematic uncertainties cancel in as far as possible. Furthermore, it provides a useful handle to study discrepancies ,between the data and the MC simulation, due to detector effects. However, it should be noted that the two decays do not have exactly the

Decay mode	Average branching fraction from the PDG [25]
$B^0 \to J/\psi K^{*0}$	$(1.34 \pm 0.06)\times10^{-3}$
$J/\psi \to e^+e^-$	$(5.94 \pm 0.06)\times10^{-2}$

Table 4.2: Summary of the relevant results for the normalisation channel $B^0 \to J/\psi(e^+e^-)K^{*0}$.

same kinematics. Due to the lower q^2 range, the electrons from $B^0 \to K^{*0}e^+e^-$ have

on average, a smaller p_{T}, than those from $B^0 \to J/\psi(e^+e^-)K^{*0}$, (and hence a higher p_{T} for the K^{*0}) as can be seen in Fig. 4.1. Consequently, the angle between the electron pair is smaller for $B^0 \to K^{*0}e^+e^-$, and thus is more susceptible to reconstruction difficulties, such as the duplication of tracks and improper bremsstrahlung reconstruction. The L0 trigger efficiency is also different for the two channels.

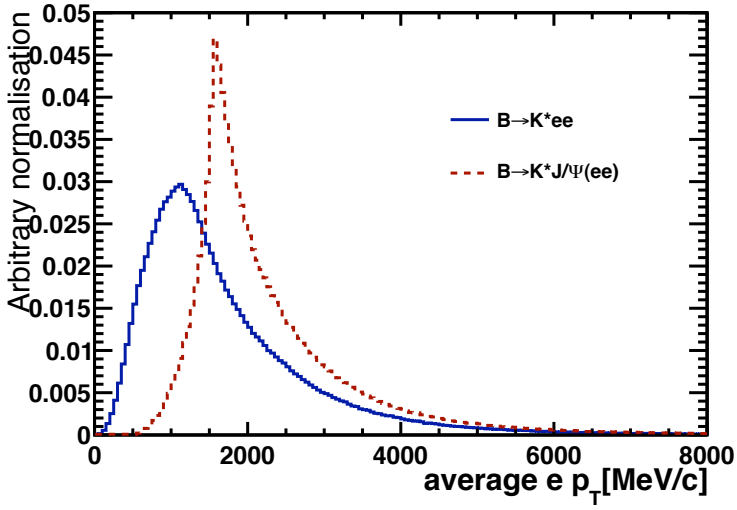

Figure 4.1: The p_{T} averaged over the positron and electron values at the generator level for $B^0 \to K^{*0}e^+e^-$ MC, shown as the blue solid line, and $B^0 \to J/\psi(e^+e^-)K^{*0}$ MC, shown as the red dotted line.

4.3.1 Data samples and software

Data

The analysis is carried out on events collected at the LHCb detector in 2011 at $\sqrt{s}$ =7 TeV, corresponding to 1 fb^{-1}, taken during stable running conditions. After being triggered by the LHCb detector, it is necessary to strip (reduce) the collected data in order to produce a dataset of a manageable size in terms of both storage, and processing time to perform the analysis. The stripping selection details are discussed in Section 4.4.1. The data were reprocessed several times a year, to take in to account improvements in alignment and reconstruction. The candidates in this analysis were reconstructed with the Reco12 configuration, and preselected by the stripping lines (containing the exclusive preselection criteria), 'StrippingBd2eeKstarLine' and StrippingBd2JpsieeKstarLine. Stripping lines are collected and saved in 'streams', in this case, the 'Radiative stream' of version Stripping17. They were analysed offline

using v29r1p1 of the DaVinci software package [66], which allows for complex selection algorithms.

Signal MC

MC samples, simulated with an average number of visible pp interactions per bunch crossing, μ=1.4, which is representative of the data collected, and passing these same stripping selections, are used to study the signal. These samples correspond to $\mathcal{O}$ (6M) $B^0 \to K^{*0}e^+e^-$ and $\mathcal{O}$ (2M) $B^0 \to J/\psi(e^+e^-)K^{*0}$ events with all four tracks in the LHCb detector acceptance of 10 mrad $<\theta <$300 mrad. The generated events are based on the model described in Ref. [67], with corrections to the form factors applied as in Ref. [68]. A separate sample of $B^0 \to K^{*0}e^+e^-$ events generated as a phase-space decay, neglecting the physics in the angular distribution were also produced in order to study the angular acceptance. Details of the versions of the software used to produce the MC samples can be found in Appendix A.

As can be seen in Fig. 3.10(a), there is a discrepancy between the data and MC in the impact parameter (IP) resolution. These differences are thought to be related to the material description in the MC, but are still under investigation. To account for this discrepancy, a 'smearing' of the tracks is applied. The IP resolution can be described as a function of the inverse of the track $p_{\rm T}$. The x and y coordinate of each simulated track state is smeared according to a Gaussian, the sigma of which corresponds to the observed data-MC differences, as a function of $p_{\rm T}$. The track states are used in the calculation of the IP, thus the smearing is propagated so that the MC samples are representative of the data.

The SPD multiplicity over the course of 2011 is also not well represented in the MC, as seen in Fig. 4.2(a), for signal $B^0 \to J/\psi K^{*0}$ MC and data samples. This is due to the fact that it is difficult to model the charged particle production in the forward region [69]. *

As the shape of the signal depends on the SPD multiplicity, with the resolution worsening with increasing SPD multiplicity, (demonstrated for $B^0 \to J/\psi K^{*0}$ MC in Fig. 4.3,) the $B^0 \to J/\psi K^{*0}$ and $B^0 \to K^{*0}e^+e^-$ MC samples were reweighed to have similar SPD distributions as the data, the result of which can be seen in Fig. 4.2(b). This increase in resolution is due to the larger occupancy in the calorimeters, and thus the degradation of the Bremsstrahlung recovery performance.

*In order to remove the majority of the background for the $B^0 \to J/\psi K^{*0}$ data sample, a cut is applied on the B mass after applying a constraint on the J/ψ mass.

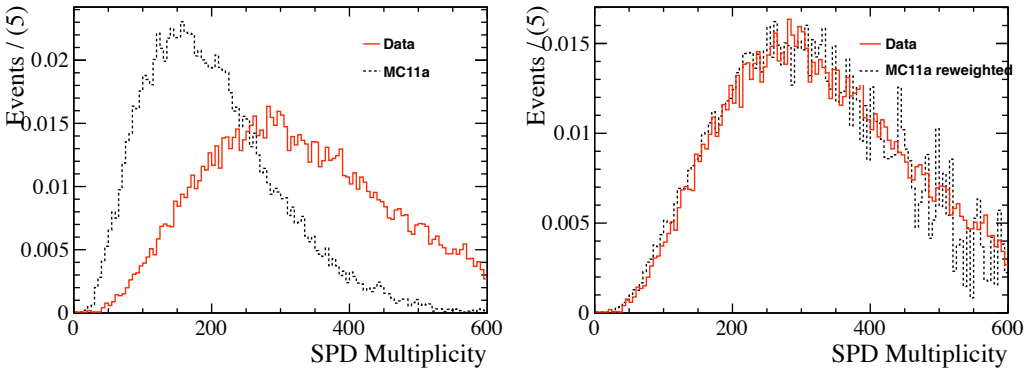

Figure 4.2: The SPD multiplicity distribution for $B^0 \to J/\psi\, K^{*0}$ data in the red solid line, and MC in the black dashed line before (left) and after (right) reweighting. It should be noted that a cut is applied on the trigger requiring the SPD multiplicity to be less than 600.

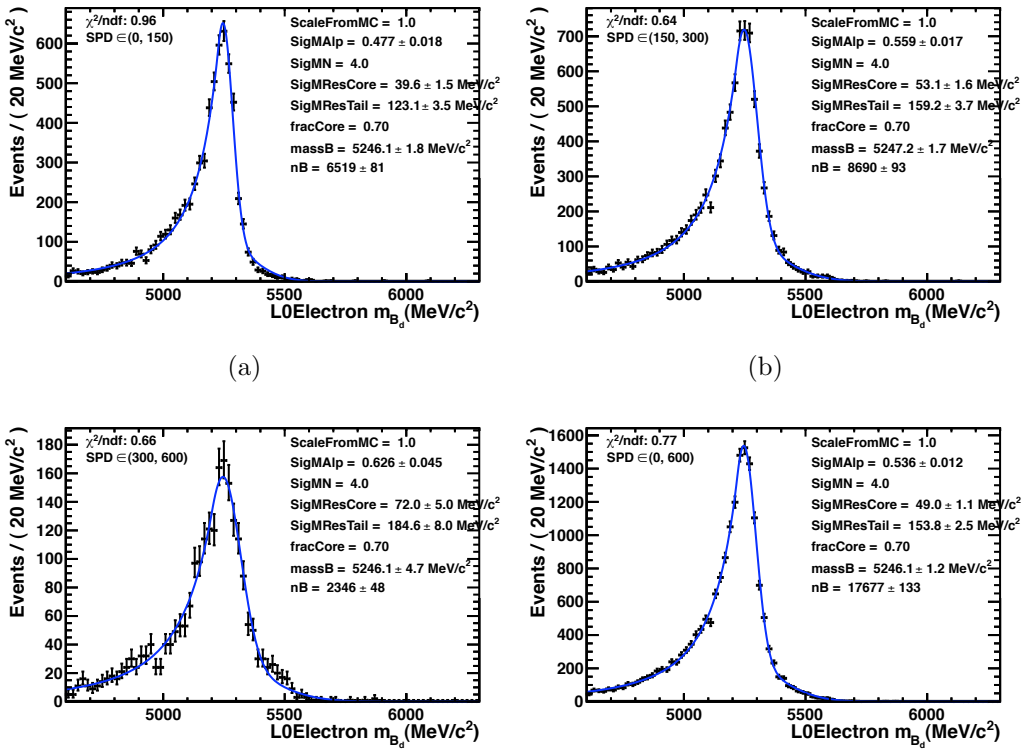

Figure 4.3: The reconstructed B mass for $B^0 \to J/\psi K^{*0}$ MC in different bins of SPD multiplicity: [0-150] (a), [150-300] (b), [300-600] (c) and [0-600] (d).

Background MC

Several background MC samples are also generated to study potential specific backgrounds. These are,

- $B^0 \to K^{*0}\gamma$,
- $B^0 \to D^- e^+ \nu$,
- $\Lambda_b \to \Lambda^* \gamma$ where $\Lambda^* = \Lambda(1520)$ and $\Lambda(1670)$,
- inclusive $B^0/B^\mp \to J/\psi\,(e^+e^-)K^*X$.

Each of these samples have their IP resolution and SPD multiplicity smeared in the same manner as the signal MC samples.

4.4 Selection

In order to minimise systematic uncertainties in the measurement of the ratio of branching fractions, the same selection procedure, (except for the invariant mass window of the electron pair,) is applied to $B^0 \to K^{*0}e^+e^-$ and $B^0 \to J/\psi\, K^{*0}$, with the selection optimised towards the more challenging $B^0 \to K^{*0}e^+e^-$ channel. In the MC selection studies conducted previously [70], a cut based analysis had been developed. However, due to the lower trigger efficiency than foreseen, in order to maximise the signal efficiency whilst still reducing the high level of combinatorial background resulting from the low $p_{\rm T}$ signal electrons, a more optimal selection was required. A multivariate analysis, based on a Boosted Decision Tree (BDT) [71] was chosen, more details of which can be found in Sect. 4.4.3.

Candidates first have to pass the trigger and stripping cuts, described in Sect. 4.4.1. A further preselection was then applied (Sect. 4.4.2) before applying the BDT. The final selection was optimised in a 2D plane of BDT output and electron $\mathrm{DLL}_{e\pi}$, (which was not used in the training of the BDT) to maximise the $\frac{S}{\sqrt{(S+B)}}$, where S and B denote the number of signal and background events, respectively. This is in order to search for a clean signal in the presence of fluctuations of the observed signal and background. This is done using $B^0 \to K^{*0}e^+e^-$ MC and the upper mass sideband from the 2011 data sample. It was found that the signal resolution and type and rate of background depends on what caused the L0 trigger to fire. For this reason, the optimisation is performed separately for three different, mutually

exclusive, trigger categories: those triggered by a signal electron, those triggered by a signal hadron, and those triggered independently from the signal decay.

The BDT is designed to reduce combinatorial background, but a high background contamination still remains from specific backgrounds with properties similar to the signal, for which extra cuts are required. MC samples are used to study and set the cuts to reduce these exclusive backgrounds.

4.4.1 Trigger and stripping cuts

The trigger conditions were relatively stable throughout 2011, with only a limited number of Trigger Configuration Keys (TCK), (which define the algorithms and selection criteria for the trigger,) used during the whole year's data taking. The most important lines for this analysis are those used for the L0 trigger, where the greatest loss in efficiency arises. As mentioned above, there are three trigger categories of interest. The first category requires the L0Electron line to be triggered by one of the signal electrons (L0ElectronTOS.) This means there is an electromagnetic cluster with a transverse energy greater than 2.5 GeV along with at least one SPD hit to signify the track is charged, as opposed to a photon. The second, demands that the electrons did not pass this line, and that the signal kaon or pion trigger the L0Hadron line (L0HadronTOS.) This line selects events with a cluster in the Hadronic Calorimeter with a transverse energy greater than 3.5 GeV. The final trigger category defined in the analysis, requires that the event passes the Trigger Independent of the Signal (TIS), and is not L0ElectronTOS or L0HadronTOS. This occurs when any particle from the event, other than those forming the signal candidate, is triggered by any trigger line, *i.e.* the Electron, Photon, Hadron, Muon or Dimuon L0 line. No requirements are placed on the HLT1 or HLT2.

An exclusive stripping selection was developed, comprising the cuts shown in Table 4.3. It selects four good quality tracks (low Track χ^2) for which the χ^2 distance of closest approach (IP χ^2) to any reconstructed Primary Vertex (PV) is large. In order to reduce ghost tracks, (*i.e.* duplicate tracks containing the same hits or resulting from a cluster from one particle being split in two), for all pairs separated by a small pseudo-distance (CloneDist) [72], the track with the worst quality track fit is removed. This is especially important for the low p_{T} electrons, as the opening angle between them is small. A cut is applied on the difference in the log-likelihoods between the pion, and kaon or electron hypothesis, for each track

Particle	Stripping Cut
B	mass window= 1000 MeV/c^2 Vertex χ^2 <45 IP χ^2 <64 IP <0.05 mm FD χ^2 >9 θ $_{\text{flight}}$ <45 mrad
K^{*0}	mass window $m_{K^{*0}}$ = 130 MeV/c^2 Vertex χ^2 <25 IP χ^2 >1 FD χ^2 >1
e^+e^- (J/ψ)	$m_{e^+e^-}(m_{J/\psi})$= 20-1500 (2200-4200) MeV/c^2 Vertex χ^2 <15 FD >1
K	p_{T} >400 MeV/c p >3000 MeV/c Track χ^2 <5 IP χ^2 >4 DLL$_{K\pi}$ >−5 CloneDist<0
π	p_{T} >300 MeV/c p >3000 MeV/c Track χ^2 <5 IP χ^2 >4 DLL$_{K\pi}$ <10 CloneDist<0
e	p_{T} >300 MeV/c Track χ^2 <5 IP χ^2 >2.25 DLL$_{e\pi}$ >−2 CloneDist0
	$\Sigma_{i=e^+,e^-,K,\pi}$IPS(i)>15

Table 4.3: Stripping selection used for $B^0 \to K^{*0}e^+e^-$ and $B^0 \to J/\psi\, K^{*0}$. See the main text in Section 4.4.1 for definitions of the variables.

in order to identify the correct particles. These tracks are then combined to form the $e^+e^-/J/\psi$ and K^{*0} candidates which are required to have a good quality fit for the decay vertices (Vertex χ^2) formed by the two tracks. The B candidate is then reconstructed by combining the e^+e^- or J/ψ with the K^{*0} candidates. It is required to have a small IP with respect to the PV, a large χ^2 separation of the

decay vertex with respect to the PV, and a small θ_{flight}, (*i.e.* the angle between the B momentum direction, and the direction of flight from the PV). To further reduce random combinatorics of tracks not truly coming from a B, a cut on the sum of the IP significance ($\Sigma_{i=e^+,e^-,K,\pi}$IPS(i)) is also applied. At this level, all the cuts applied are kept loose.

4.4.2 Preselection cuts

Before training the BDT, a further preselection was applied on top of the stripping cuts. This was primarily to tighten the particle identification (PID) cuts, and to include sanity checks removing any anomalous measurements, both of which could result in sub-optimal training. A few other cuts were tightened slightly in order to reduce the dataset to a more manageable size to perform the BDT training, but whilst retaining high efficiency on the signal. The details of the cuts in this preselection can be seen in Table 4.4. According to the MC, the efficiency of the preselection on triggered and stripped events, ϵ_{presel}= 0.87, with a large part of the loss coming from the tightened PID cuts.

Particle	Preselection Cut
B	Vertex χ^2 <36
	Vertex χ^2 >0
	IP χ^2 >0
	FD χ^2 >16
	FD χ^2 <100000
	θ_{flight} <16 mrad
K^{*0}	Vertex χ^2 <15
$e^+e^-/J/\psi$)	$m_{e^+e^-}$= (30-1000)/(2400-3400) MeV/c^2
K	$\text{DLL}_{K\pi}$ >0
π	$\text{DLL}_{K\pi}$ <5
e	p_{T} <25000 MeV/c
	$\text{DLL}_{e\pi}$ >0
	$\Sigma_{i=e^+,e^-,K,\pi}$IPS(i)>20

Table 4.4: Preselection applied before the BDT training. See the main text in Section 4.4.1 for definitions of the variables.

4.4.3 Boosted Decision Tree (BDT) training

The final selection was performed using a BDT built under the TMVA package [73]. Other multivariate discriminants were tested, and the BDT was found to have the best performance. It was trained to discriminate MC $B^0 \to K^{*0}e^+e^-$ from the upper sideband (m_{B^0} >5600 MeV/c^2) of the data collected, which is representative of the combinatorial background. In order to check for over-training in an unbiased manner, the samples were split in two by taking every other event to obtain, in the case of the real data, an average sample covering any changes in running conditions over time. One half was used to train the BDT, and the other to test its performance. Only the upper sideband was used in the training, as the lower also contains partially reconstructed events. The strength of the BDT is in distinguishing signal events from random combinatorics, and including these partially reconstructed events which have signal-like properties would result in a less than optimal discriminant. The BDT is built using the variables listed in Table 4.5, the distributions of which can be seen in Appendix B.1. It should be noted, that although including the daughter $p_{\rm T}$ in the discriminant can bias the angular acceptance and the objective is to perform an angular analysis of $B^0 \to K^{*0}e^+e^-$, once sufficient statistics are accumulated, it has been shown previously [70] that the analysis is not sensitive to the detailed knowledge of the angular acceptance.

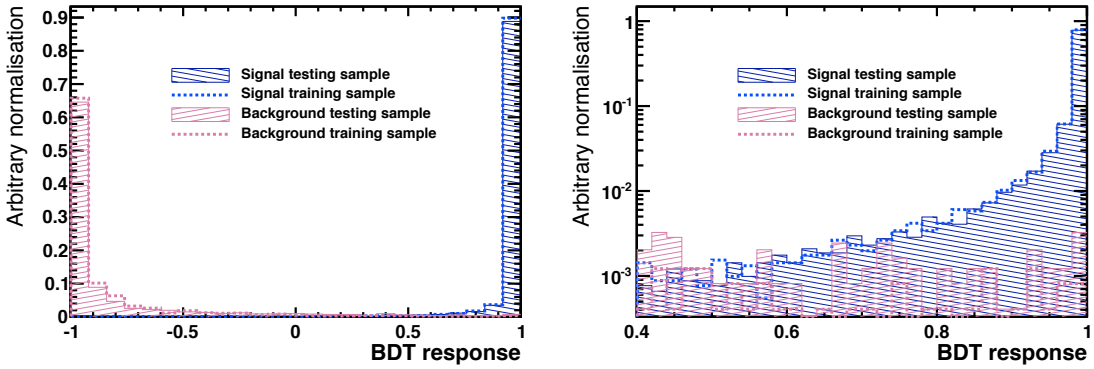

Figure 4.4: The output of the BDT for the signal and background for both the testing sample (shown in the hatched histograms) and the training sample (the dotted lines) in the full range (left) and on a log scale between 0.4 and 1 (right).

The agreement between MC and data for the BDT output was checked using $B^0 \to J/\psi K^{*0}$, and can be seen in Fig. 4.5(a) for BDT>0.8, where it is easier to obtain a clean data sample. This is done by applying a mass constraint on the J/ψ

Table 4.5: List of the variables used to build the BDT discriminant. See the main text in Section 4.4.1 for definitions of the variables.

Particle	Variable
B	p_{T}
	Vertex χ^2
	IP χ^2
	FD χ^2
	θ flight
K^{*0}	$m_{K^{*0}}$
	Vertex χ^2
	FD χ^2
e^+e^-	Vertex χ^2
	FD χ^2
Daughter	p_{T}
	IP χ^2
	Track χ^2

mass with the BDT cut set at 0.8, and the remaining background is removed using sweights [74]. The B mass distribution of this data sample is shown in Fig. 4.5(b).

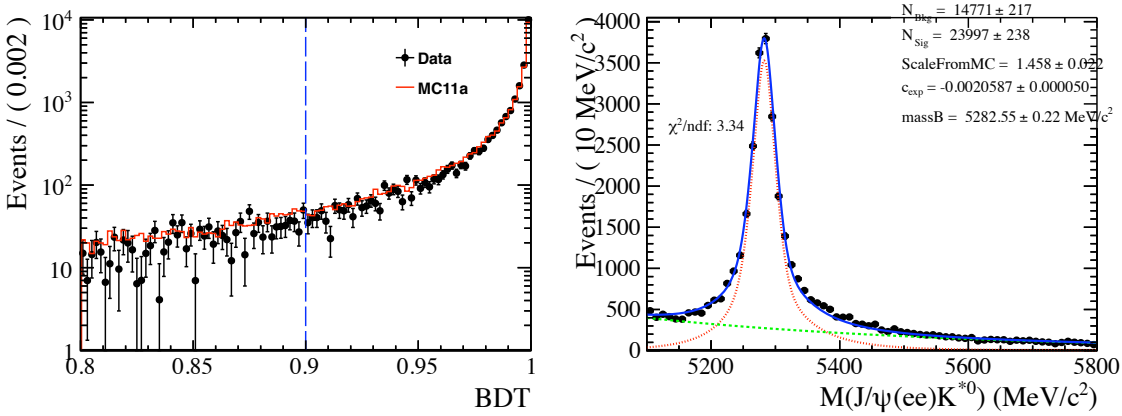

Figure 4.5: The output of the BDT for $B^0 \to J/\psi\, K^{*0}$ MC and data, with the background removed using the splot technique.

4.4.4 Optimisation

The BDT response for the signal peaks at one, and the background at minus one, as can be seen in Fig. 4.4, where the output for both the testing and training samples

are shown, to verify the discriminant does not suffer from over-training. In order to select the optimal cut value of the BDT output, a 2D optimisation was performed to maximise the $\frac{S}{\sqrt{(S+B)}}$ for both the BDT output and the $\mathrm{DLL}_{e\pi}$ value. It was found that the optimal PIDe cut is at 1, regardless of the BDT cut, as can be seen in Fig. 4.6, which shows the $\frac{S}{\sqrt{(S+B)}}$ in bins of BDT output and PIDe for the L0 Electron category. The method used to calculate the S and B is based on the fit as

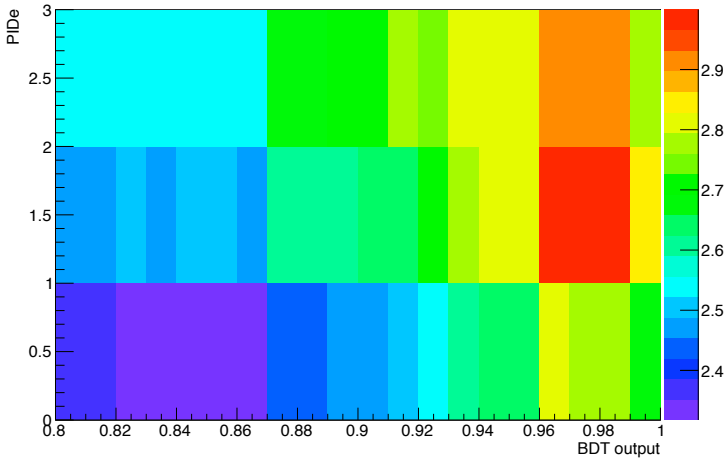

Figure 4.6: The $\frac{S}{\sqrt{(S+B)}}$ in bins of BDT output and PIDe for the $B^0 \to K^{*0}e^+e^-$ L0 Electron category.

discussed in Section 4.8. S is taken from the $B^0 \to K^{*0}e^+e^-$ MC, corrected by the ratio the yields predicted and observed in the $B^0 \to J/\psi\,(e^+e^-)K^{*0}$ case. B is taken from the number of background observed in data in a mass window of $\pm$ 300 MeV/c^2 around the B^0 mass. As this has the potential to bias the result, the procedure was repeated by extrapolating the amount of B in the signal region using the sidebands. The optimal cut values were found to be unchanged.

The $\frac{S}{\sqrt{(S+B)}}$ as a function of BDT cut for each trigger setting is shown in Fig. 4.7(a), with the optimal BDT cut value highlighted.

4.5 Signal after selection

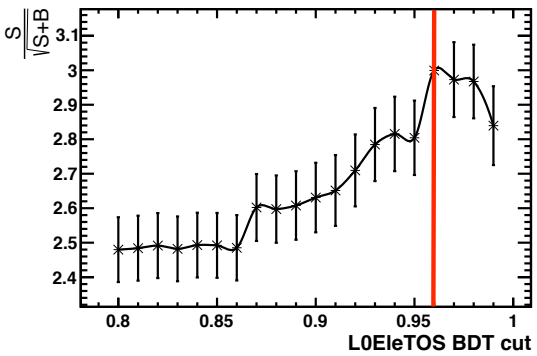

(a) L0ElectronTOS $\frac{S}{\sqrt{S+B}}$

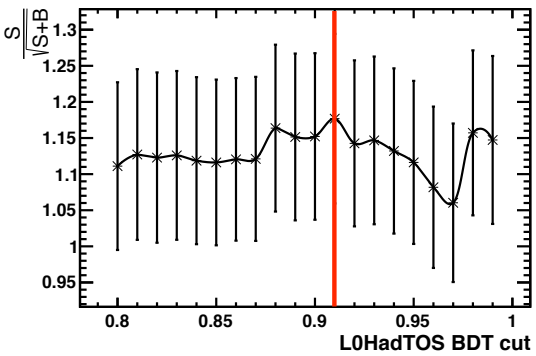

(b) L0HadronTOS $\frac{S}{\sqrt{S+B}}$

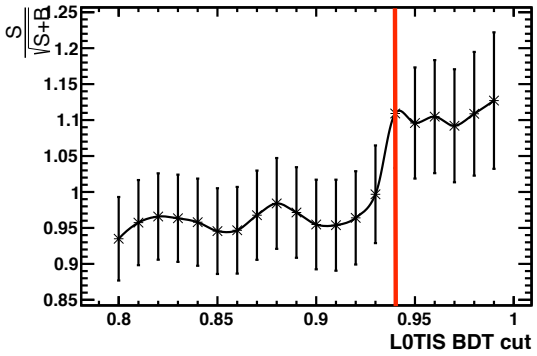

(c) L0TIS $\frac{S}{\sqrt{S+B}}$

Figure 4.7: The $\frac{S}{\sqrt{S+B}}$ variation with increasing BDT cut for each of the three trigger categories. The optimal BDT cut is marked with the yellow line

4.5.1 Bremsstrahlung recovery

Due to final state radiation and detector interactions, there is a probability for the electron to emit Bremsstrahlung photons. If this occurs after the magnet, the photon will be deposited in the same calorimeter cells as the electron, and the energy will be recuperated. However, if the photon is emitted before the magnet, the electron will be deflected by the magnetic field whereas the photon will continue on its initial trajectory, with its energy being deposited in a different part of the calorimeter from the electron, as demonstrated in Fig. 4.8. Missing this energy results in a worse reconstructed B^0 mass resolution, so it is desirable to recovery these Bremsstrahlung photons when possible. With the standard Bremsstrahlung

recovery tool, photons emitted before the magnet are searched for by linearly extrapolating the reconstructed electron track before the magnet to the plane of the ECAL, thus giving a predicted Bremsstrahlung photon position. A χ^2_{brem} is then constructed of the matching between this predicted position, and the barycentric position of the neutral clusters, and the photon energy with the smallest χ^2_{brem} is added to the momentum of the electron.

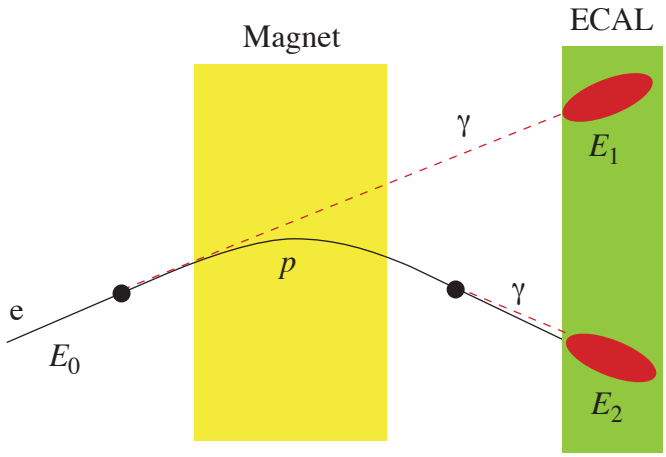

Figure 4.8: Schematic illustration of Bremsstrahlung photon recovery. An electron may radiate photons when passing through material before or after the magnet. In the first case, a well defined cluster corresponding to the photon is seen in the ECAL, with energy E_1, thus the energy of the electron at the origin, $E_0 = E_1 + E_2$ whilst in the second case the Bremsstrahlung energy forms part of the electron cluster with energy $E_2 = p$, the momentum measured in the spectrometer. (Taken from [75].)

4.5.2 Mass plots from $B^0 \to K^{*0}e^+e^-$ MC

The reconstructed B^0 masses for $B^0 \to K^{*0}e^+e^-$ and $B^0 \to J/\psi(e^+e^-)K^{*0}$ in the MC surviving the BDT cuts have very different shapes, as can be seen in Fig. 4.5.2. This is due to effects from the Bremsstrahlung recovery procedure: the small angle between the two low p_T electrons in $B^0 \to K^{*0}e^+e^-$ can cause the photon energy to be added to both electron tracks erroneously, and this extra energy thus explains the tail at high B^0 mass values. According the $B^0 \to K^{*0}e^+e^-$ MC, 44% of the signal events where a Bremsstrahlung photon is recuperated results in its double

counting (whereas the effect is less than 1% for $B^0 \to J/\psi\,(e^+e^-)K^{*0}$.) To rectify this, the Bremsstrahlung energy added to each electron was calculated, and if for both electrons, this was non zero and identical within 5 MeV, the added Bremsstrahlung energy for one electron (chosen randomly) was removed, and the e^+e^- and B^0 masses were recomputed. The corrected reconstructed B^0 mass for $B^0 \to K^{*0}e^+e^-$ is shown in Fig. 4.10. With this correction implemented, the MC predicts a total of 59 $B^0 \to K^{*0}e^+e^-$ events after the BDT selection in the 1 fb^{-1} collected in 2011.

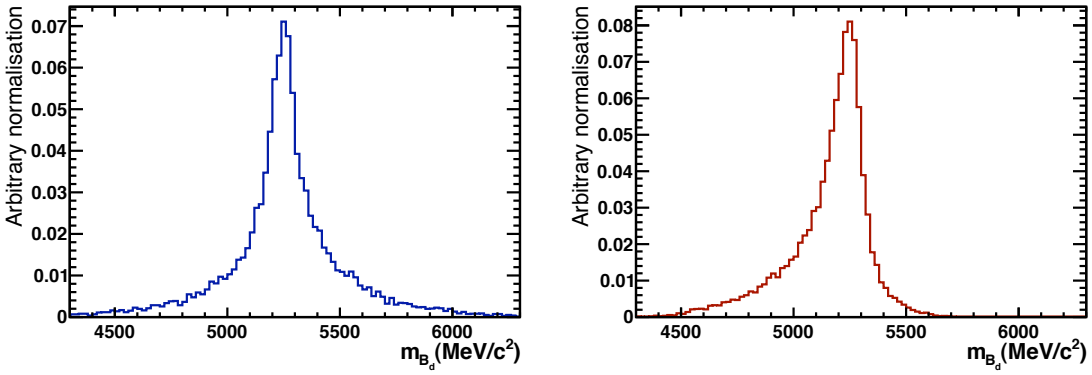

(a) $B^0 \to K^{*0}e^+e^-$ MC (b) $B^0 \to J/\psi\,(e^+e^-)K^{*0}$ MC

Figure 4.9: The reconstructed invariant B^0 mass after the standard Bremsstrahlung recovery.

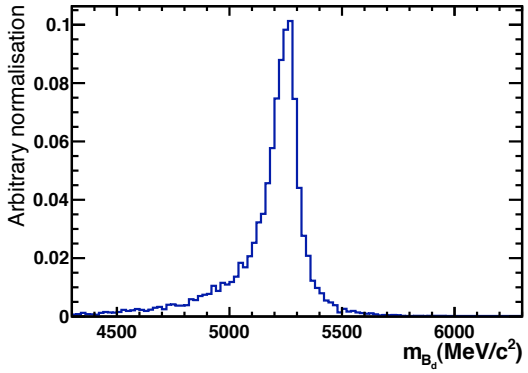

Figure 4.10: The reconstructed invariant B^0 mass after removing double counted Bremsstrahlung photons for $B^0 \to K^{*0}e^+e^-$ MC.

4.6 Specific background contamination

After applying the BDT selection, there still remains background from decays which have properties similar to the signal, and therefore survive the cut. As some of these have much larger branching fractions than $B^0 \to K^{*0}e^+e^-$, and peak under the signal mass, extra cuts were developed to reduce these contributions. It was checked using MC samples, that none of these background decays are expected to be reconstructed with a mass greater than 5600 MeV/c^2 as was used in the background sample for the BDT training, so they are not expected to be detrimental to the BDT training. The backgrounds considered in are:

- $B^0 \to K^{*0}\gamma$ where the photon converts into two electrons.
- Decays of the type, $B \to K^*\eta$, with and without a Dalitz pair.
- The semileptonic decay, $B^0 \to D^-e^+\nu$ where neutrinos are not reconstructed.
- $\Lambda_b \to \Lambda^*\gamma$ where the Λ^* decays to a kaon and a proton that is misidentified.
- $B^0 \to J/\psi\,(e^+e^-)K^{*0}$ with enough missing energy due to bremsstrahlung radiation to shift the J/ψ mass within the range, [30-1000] MeV/c^2.

4.6.1 $B^0 \to K^{*0}\gamma$

The branching fraction of $B^0 \to K^{*0}\gamma$ has been measured to be $\mathcal{B}= (4.33 \pm 0.15) \times 10^{-5}$ [25], and in the case where the photon converts into two electrons, it will have similar characteristics to $B^0 \to K^{*0}e^+e^-$. In LHCb, around 40% of the photons convert before the calorimeter, and although only a small fraction of these, $\mathcal{O}$ (10%) are reconstructed, the resulting B^0 mass should peak under that of the signal, making it a particularly dangerous background. MC samples samples were used to check the efficiency of the selection on this channel. The distribution of the reconstructed B^0 after the stripping and preselection is shown in Fig.4.11, and corresponds to an expected yield of 24 events in the 1 fb^{-1} analysed here. The output of the BDT when applied to the $B^0 \to K^{*0}\gamma$ MC is shown in Fig. 4.12, and as expected, it follows a similar distribution as $B^0 \to K^{*0}e^+e^-$. Extra cuts are therefore necessary to reduce this background.

Contrary to $B^0 \to K^{*0}e^+e^-$, the z coordinate of the vertex of e^+e^- pair in $B^0 \to K^{*0}\gamma$ does not have to coincide with that of the K^{*0} vertex. However, if this

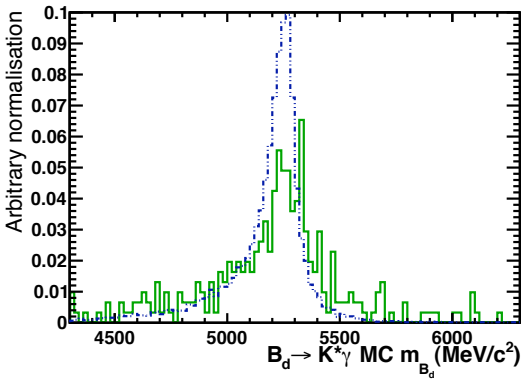

Figure 4.11: The reconstructed invariant B^0 mass of the $B^0 \to K^{*0}\gamma$ MC passing the $B^0 \to K^{*0}e^+e^-$ stripping and preselection cuts.

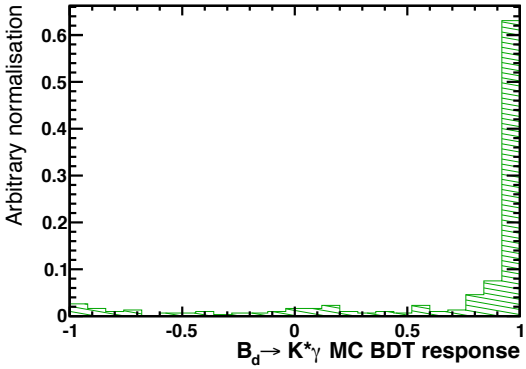

Figure 4.12: The output of the BDT when applied to the $B^0 \to K^{*0}\gamma$ MC passing the $B^0 \to K^{*0}e^+e^-$ stripping and preselection cuts with the cut value shown as the yellow line.

coordinate is measured with a large error, the e^+e^- may still be reconstructed as originating from the B^0 decay. Fig. 4.13 shows the absolute difference between the z coordinate of the e^+e^- and the K^{*0} vertices, as a function of the error on the z coordinate of the e^+e^- pair for both the $B^0 \to K^{*0}e^+e^-$ and $B^0 \to K^{*0}\gamma$ MC samples, after applying the BDT selection. Applying a cut on the error $\sigma(z(e^+e^-))$<30 mm removes 55% of the $B^0 \to K^{*0}\gamma$ events, and around 4% of the signal. However, this still leaves 11 events expected in the data and requires a further cut.

Electrons coming from a converted photon have a different distribution of hits in the VELO stations compared to electrons coming from the signal. The distributions of the z coordinate of the VELO sensor that first measured a hit from an electron track, (in terms of distance from the interaction point,) are shown in Fig. 4.14. This can be compared with the sensor where the first measurement would be expected

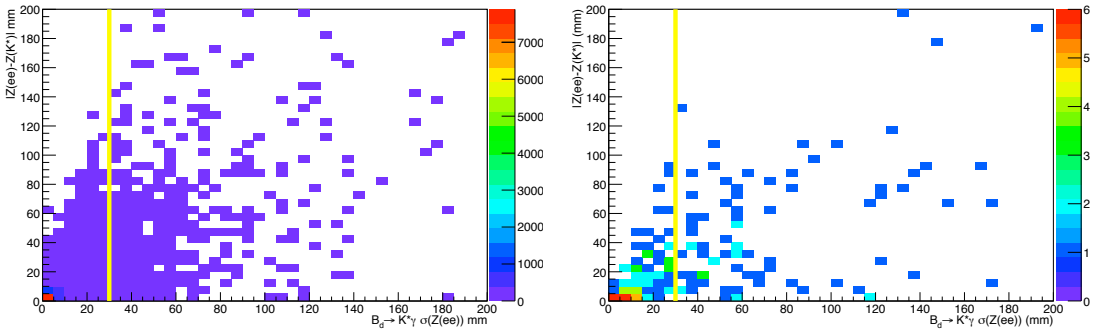

(a) $B^0 \to K^{*0}e^+e^-$ MC (b) $B^0 \to K^{*0}\gamma$ MC

Figure 4.13: The absolute difference between the z coordinate of the e^+e^- and the K^{*0} vertices, as a function of the error on the z coordinate of the e^+e^- pair.

if the electron comes from a $B^0 \to K^{*0}e^+e^-$ decay. A schematic showing how this expected first measurement is determined is shown in Fig. 4.15. The electron track is projected from the position of the K^{*0} vertex in the direction of the electron momentum. At each VELO sensor z position, the expected x and y coordinate of the electron track is computed. The first sensor position where these coordinates lie within the active region of the VELO sensor is taken as the expected first measurement z coordinate. The distribution of the expected z coordinate of the first measurement is also shown in Fig. 4.14, and the difference between the expected and measured first measurements can be seen in Fig. 4.16. A cut on the difference at less than 30 mm leaves only 5 expected events, whilst removing 7% of the signal, according to the MC.

4.6.2 $B \to K^*\eta$

In principle, there is another class of partially reconstructed events that have a different shape compared to the partially reconstructed events seen in the $B \to J/\Psi K^*$ sample. These are the ones where the e^+e^- comes from a converted photon. The prime example is $B \to K^*\eta$.

One of the photons from the $\eta \to \gamma\gamma$ transition can convert to an e^+e^- pair in the VELO material. These events have a very low e^+e^- invariant mass, and are thus suppressed by the same veto used to suppress events from $B \to K^*\gamma$

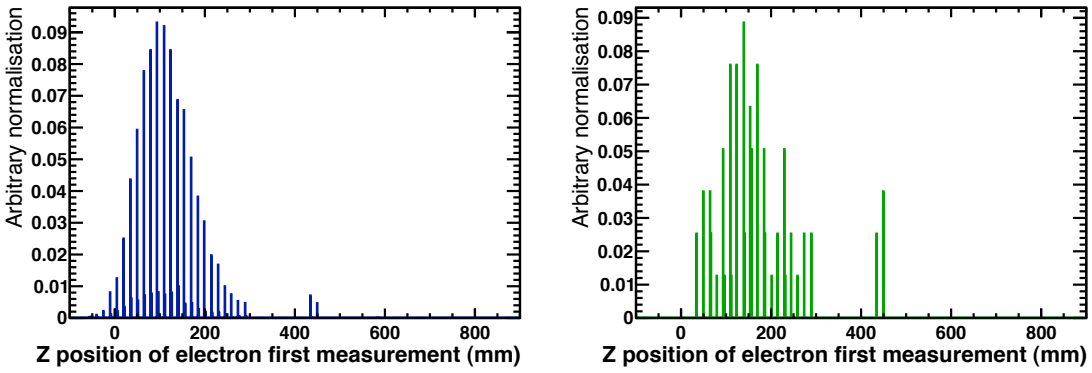

(a) $B^0 \to K^{*0}e^+e^-$ MC

(b) $B^0 \to K^{*0}\gamma$ MC

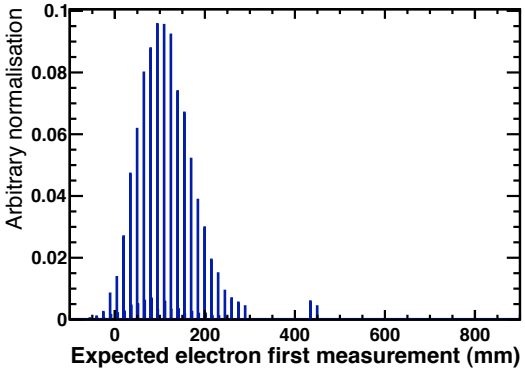

(c) $B^0 \to K^{*0}e^+e^-$ MC

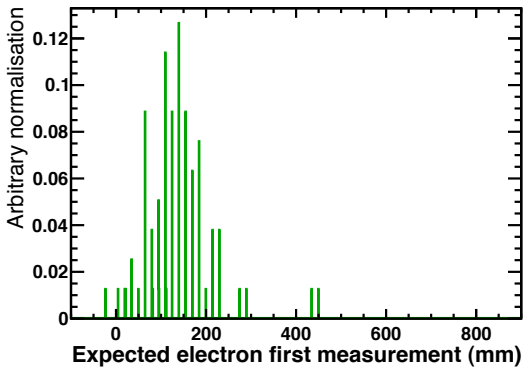

(d) $B^0 \to K^{*0}\gamma$ MC

Figure 4.14: The Z position of the first measurement of an electron (left) and that which is predicted in the case of signal (right), for $B^0 \to K^{*0}e^+e^-$ (above) and $B^0 \to K^{*0}\gamma$ (below) MC.

followed by a conversion $\gamma \to e^+e^-$. Their expected yield can be calculated from the ratio of the $B \to K^*\eta$ branching ratio to that of $B \to K^*\gamma$: $\frac{6.4\times10^{-6}}{4.33\times10^{-5}} = 0.148$. As the contamination from $B \to K^*\gamma(\to e^+e^-)$ has been evaluated (4.6.1) to be approximately 10%, and including a factor two since in the $B \to K^*\eta$ case, 2 photons can convert, the fraction of these partially reconstructed events is 2.9% of the $B \to K^*e^+e^-$ events . Because of the isotropic decay of the η, in the B centre of mass frame, the energy of non-reconstructed photons will have a flat distribution from 28 MeV to 2480 MeV. This means only about 0.33 (i.e. 1% of the total events) will have a reconstructed B mass between 4300 MeV/c^2 and the B mass(with a flat spectrum). Therefore it is a negligible contribution.

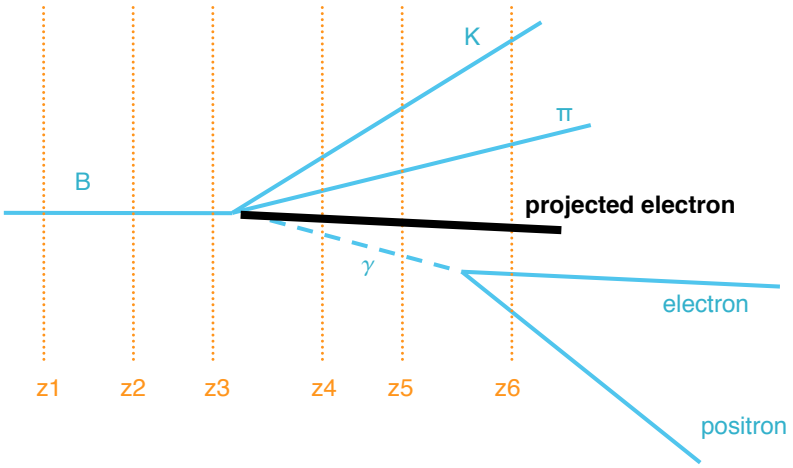

Figure 4.15: The electron track is projected from the position of the K^{*0} vertex in the direction of the electron momentum. At each VELO sensor z position, the expected x and y coordinate of the electron track is computed. The first sensor position where these coordinates lie within the active region of the VELO sensor is taken as the expected first measurement z coordinate. In this $B^0 \to K^{*0}\gamma$ case, the expected first measurement is at z4, whereas the first position actually measured is at z6.

Another possibility however, is that the η decays with a Dalitz pair. This pair originates from the B vertex and can have a mass larger than 30 MeV/c^2, and therefore could be accepted by our selection cuts. The mass spectrum of the Dalitz pair is given, for example in the original paper [76]. If $x = \frac{m^2_{e^+e^-}}{m^2_\eta}$ and $y = \frac{4m^2_e}{m^2_\eta}$ then:

$$\frac{dN}{dx} = \frac{1}{x} \times \sqrt{\frac{x-y}{x}} \times (1 + \frac{y}{2x}) \times (1-x)^3 \tag{4.4}$$

Integrating for $m_{e^+e^-} > 30$ MeV/c^2, one obtains that 38% of Dalitz pair will have a e^+e^- invariant mass greater than 30 MeV/c^2, with a median mass of 100 MeV/c^2. Including the Dalitz branching ratio of 1.75% , the branching ratio of $B \to K^*\eta$ eith $\eta \to \gamma\gamma$ of 6.4×10^{-6}, and the 38% above, one obtains a partially reconstructed contribution of 4.3×10^{-8} i.e. 16% of the $B \to K^*e^+e^-$ rate. These events will have a flat spectrum of non-reconstructed gamma between 28 MeV and 3241 MeV

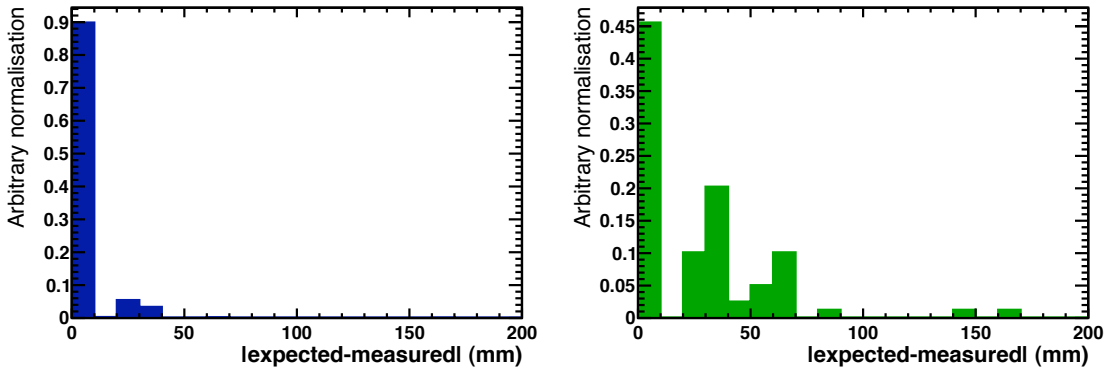

(a) $B^0 \to K^{*0}e^+e^-$ MC (b) $B^0 \to K^{*0}\gamma$ MC

Figure 4.16: The difference between the z position of the first measurement of an electron, and that which is predicted in the case of signal.

and hence a reconstructed Bmass from m_{B^0} -28 MeV/c^2 to m_{B^0} -3241 MeV/c^2. In a B mass interval of m_{B^0} ± 300 MeV/c^2, there will be a contribution of $\frac{300}{3241-28} \times 4.32 \times 10^{-8} = 4.0 \times 10^{-9} = 1.5\%$ of the predicted $B^0 \to K^{*0}e^+e^-$ branching ratio, which can be neglected. In the interval (4.3-5.0) GeV approximately, where the combinatorial + partially reconstructed background is fitted, the branching ratio is 9.4×10^{-9},i.e.3.4% of the K*ee branching ratio, and this is still small compared to the 50% error on the partially reconstructed background. This background can thus be neglected. All other contributions with Dalitz pairs from $B \to K^*\pi^0$, $B \to K^*\eta'$ with $\eta' \to \gamma\gamma$ or $\rho\gamma$, $B \to K^*\omega$ with $\omega \to \pi^0\gamma$ give much smaller contribution.

4.6.3 $B^0 \to D^-e^+\nu$

A further exclusive background comes from $B^0 \to D^-e^+\nu$ with the D^- decaying to e^- K^{*0} ν, the first order Feynman diagram of which can be seen in Fig. 4.17. As the neutrinos are not reconstructed, the reconstructed B^0 mass is generally lower than that of the signal, but it can still fall within the selection mass window (see Fig. 4.18 for the reconstructed B^0 mass of the $B^0 \to D^-e^+\nu$ MC passing the preselection). The branching fraction for this channel is very large compared to the signal: $\mathcal{B} \approx$ 2.17%, meaning that after the preselection cuts, 75 events are expected in the analysis sample. The B^0 candidate does not have a lot of missing momentum. Therefore, the neutrinos have low energy and the decay has the characteristics of

a completely reconstructed B event with the same final state as the signal, so the BDT output is again similar to that of $B^0 \to K^{*0}e^+e^-$, as can be seen in Fig. 4.19. The small neutrino energies imply that in the rest frame of the B, the D^- and e^+ are produced almost back to back with the e^+ having an energy of ≈ 2 GeV and in the rest frame of the D^-, the K^{*0} and e^- will be almost back to back. To produce a small reconstructed e^+e^- mass, the K^{*0} will be in almost the opposite direction to e^+. The fact that the neutrino energies must be small (in order to pass the cut on the θ_{flight} of the B) creates an asymmetry in the $\cos(\theta_L)$ distribution , where θ_L is one of the angles of interest in the angular analysis, as shown in Fig. 2.2, and defined as the direction between the e^+ and the direction opposite the B^0 in the rest frame of the e^+e^-, and is symmetric for $B^0 \to K^{*0}e^+e^-$. Although this is not the angle most critical to the photon polarisation measurement, it is still preferable to remove these events. In order to reduce this background, the invariant mass of the K^{*0} combined with the lepton that would come from the D is computed, as shown after the BDT selection for the signal and $B^0 \to D^-e^+\nu$ MC samples in Fig. 4.20. A lower cut on this invariant mass system at 1900 MeV/c^2 removes most of these events, with the MC predicting nine remaining in the 1 fb^{-1} of data, but none within the signal window, for a 3% loss of $B^0 \to K^{*0}e^+e^-$ MC.

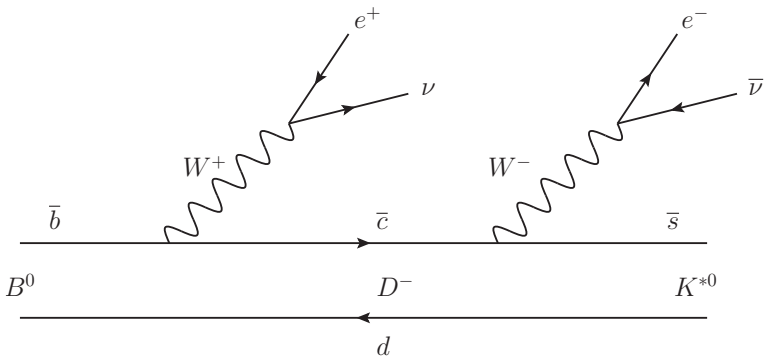

Figure 4.17: The Feynman diagram for $B^0 \to D^-e^+\nu$ with the D^- decaying to e^- K^{*0}.

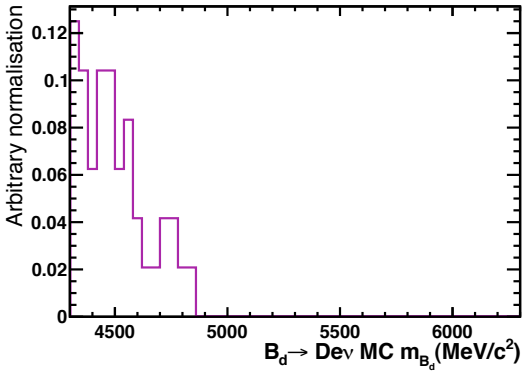

Figure 4.18: The reconstructed B^0 mass for $B^0 \to D^- e^+ \nu$ MC passing the stripping preselection cuts.

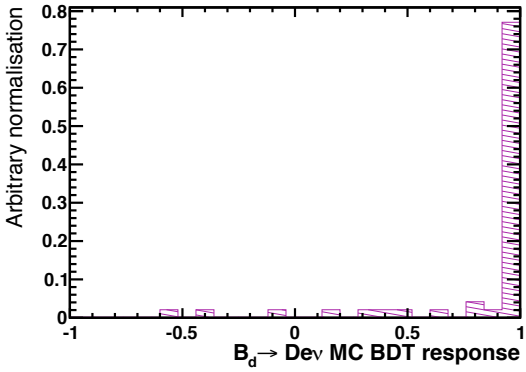

Figure 4.19: The BDT output for $B^0 \to D^- e^+ \nu$ with the D^- decaying to e^- K^{*0} MC.

4.6.4 $\Lambda_b \to \Lambda^* \gamma$

We have investigated the potential contamination due to radiative $\Lambda_b \to \Lambda^* \gamma$, where Λ^* stands for $\Lambda(1520)$ and $\Lambda(1670)$, both of which can decay to a pK final state with unknown branching fractions. However, for the $B \to K^* \gamma$ publication an estimate of the effective branching fraction has been performed for a $K\pi$ invariant mass of less than 2.5 GeV [77], where they find :

$$B(\Lambda_b \to \Lambda^*(pK^-)\gamma) \times \frac{f_{\Lambda_b}}{f_d} = (4.2 \pm 0.7) \times 10^{-6} \tag{4.5}$$

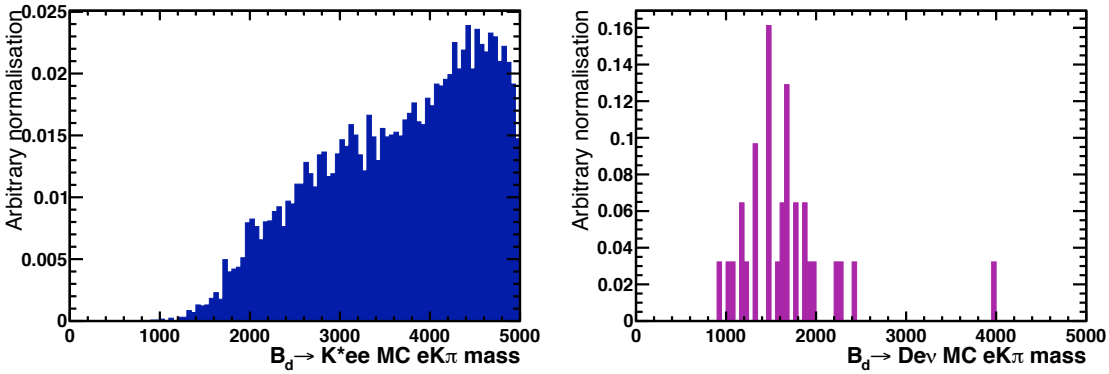

(a) $B^0 \to K^{*0} e^+ e^-$ MC

(b) $B^0 \to D^- e^+ \nu$ MC

Figure 4.20: The invariant mass of the kaon, pion and electron that would come from the D in the case of $B^0 \to D^- e^+ \nu$ after the BDT cuts.

where f_{Λ_b} and f_d are the hadronisation factors of the b quark to λ baryons and B^0 mesons, respectively.

Two batches of one million generated events MC events corresponding to $\Lambda_b \to \Lambda(1520/1670)\gamma$ have been analysed, using the $B^0 \to K^{*0} e^+ e^-$ selection with only the very loose PID cuts at the stripping level applied. One event is selected for the $\Lambda(1520)$ and 4 for the $\Lambda(1670)$.

Combining these efficiencies with eqn. 4.5, one finds that, summing all the trigger categories together one ends with less than one event before applying the tight PID cuts. This small background is thus neglected.

4.6.5 $\phi \to KK$ veto

Background can arise from events where a K is misidentified as a π, thus a ϕ is reconstructed as a K^{*0}. This background is largely reduced by the PID cuts applied at the preselection, but the distribution of the K^{*0} mass recomputed under the K K hypothesis in the $B^0 \to J/\psi\,(e^+e^-)K^{*0}$ data, as shown in Fig. 4.21, shows a small contribution from remaining ϕ events. This is reduced by requiring the K K mass to be greater than $1040\,\mathrm{MeV}/c^2$, which removes less than one percent of the signal

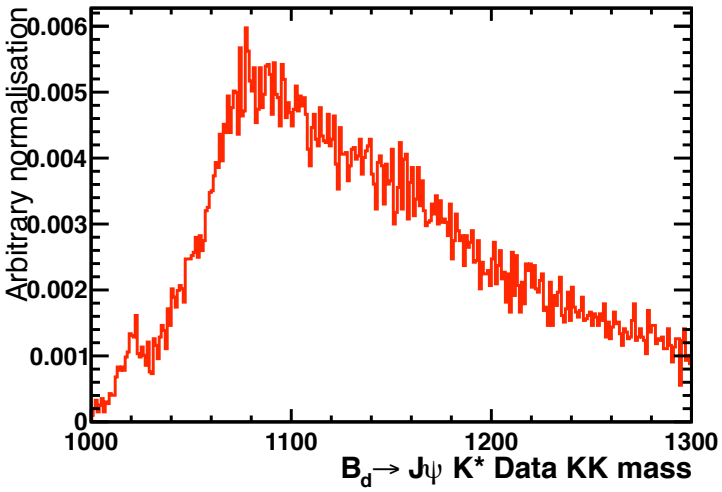

Figure 4.21: The K^{*0} mass recomputed under the K K hypothesis for the $B^0 \to J/\psi(e^+e^-)K^{*0}$ data. The small peak around 1020 MeV/c^2 comes from misidentified ϕ particles

4.6.6 $B^0 \to J/\psi(e^+e^-)K^{*0}$

The selection for $B^0 \to K^{*0}e^+e^-$ was applied to the $B^0 \to J/\psi(e^+e^-)K^{*0}$ MC sample, in order to analyse the contamination. For this to occur, the event must suffer from non-recovered bremsstrahlung photons to the extent that the J/ψ is reconstructed within the dilepton mass range (30-1000) MeV/c^2. The surviving MC corresponds to one expected event in the 1 fb^{-1} sample, but as the missing energy propagates to the reconstructed B^0 mass, they were found with a mass below the chosen B^0 signal window of $\pm$ 300 MeV/c^2. This background is therefore negligible.

4.7 Predictions from $B^0 \to K^{*0}e^+e^-$ MC

It order to use the MC to predict the number of events expected in a given data sample, it is necessary that the distributions of the variables used in the selection are well simulated, as far as possible. As mentioned above, the track IP of the MC was smeared to mimic that of the data. There is also a known discrepancy between the kaon, pion and electron identification performance between data and MC. This can be corrected for by using the PID calibration procedure [78], details of which

are given in Section 4.10.2.4.

4.7.1 Expectations for $1\,\text{fb}^{-1}$ of data from $B^0 \to K^{*0}e^+e^-$ MC

The predicted yields for $B^0 \to K^{*0}e^+e^-$ and $B^0 \to J/\psi\,(e^+e^-)K^{*0}$ in the $1\,\text{fb}^{-1}$ sample collected in 2011 according to the MC are shown in Table 4.6 and Table 4.7 for each stage of the selection, and for each of the three categories, and in total. This however, assumes that the MC correctly reproduces the number of events falling within each trigger category, and neglects any radiation damage on the detector.

Table 4.6: The expected number of $B^0 \to K^{*0}e^+e^-$ events in 1 fb^{-1} as predicted by the MC assuming a branching ratio of 2.9×10^{-7}.

Trigger category	Preselection(no. events)	BDT	Specific cuts
L0ElectronTOS	50	45	39
L0HadronTOS	17	16	13
L0TIS	18	15	13
Total	86	76	64

Table 4.7: The expected number of $B^0 \to J/\psi\,(e^+e^-)K^{*0}$ events in 1 fb^{-1} as predicted by the MC

Trigger category	Preselection(no. events)	BDT	Specific cuts
L0ElectronTOS	23300	19700	15500
L0HadronTOS	2800	2400	1900
L0TIS	6700	5400	4000
Total	32747	27606	21371

4.8 Fitting procedure

As the expected number of $B^0 \to K^{*0}e^+e^-$ events in 1 fb^{-1} is low, it is not possible to determine all the probability density function (PDF) parameters directly from a fit to data. Furthermore, although $B^0 \to J/\psi\,(e^+e^-)K^{*0}$ benefits from a much larger

yield, the kinematics are not the exactly the same, as was shown in Section 4.3. It is therefore necessary to use input from the $B^0 \to K^{*0}e^+e^-$ MC, but corrected by a μ_B scale factor determined by $B^0 \to J/\psi\,(e^+e^-)K^{*0}$ to account for differences arising between the data and the MC. To extract the $B^0 \to K^{*0}e^+e^-$ signal yields, an extended unbinned maximum likelihood fit is performed, which also allows fits for the number of combinatorial background. As will be described below, the number of partially reconstructed background is fixed using information from $B^0 \to J/\psi\,(e^+e^-)K^{*0}$.

4.8.1 Signal shape

The reconstructed signal B^0 mass is parametrised by a double Crystal-Ball (CB) distribution [79], in order to take into account the tail arising from energy losses due to missing Bremsstrahlung photons. The CB function is described by:

$$f(x;\alpha,n,\overline{x},\sigma) = N \times \begin{cases} \exp\left(-\frac{(x-\overline{x})^2}{2\sigma^2}\right), & \text{for } \frac{x-\overline{x}}{2\sigma} > -\alpha \\ A \times \left(B - \frac{x-\overline{x}}{\sigma}\right)^{-n}, & \text{for } \frac{x-\overline{x}}{2\sigma} \leq -\alpha \end{cases} \tag{4.6}$$

where A and B are:

$$A = \left(\frac{n}{|x|}\right)^n \exp\left(-\frac{\alpha^2}{2}\right) \tag{4.7}$$

$$B = \frac{n}{|\alpha|} - \alpha \tag{4.8}$$

The two CB functions share the same $\mu_{B^0\text{mass}}$, α: the transition point from a Gaussian distribution to a power law tail distribution, and n: the exponent of the power law tail, but with differing widths, σ_1 and σ_2. The n parameter is highly correlated with α, and so n is fixed to be 4. The μ_{B^0} is fixed, using the value as measured in the $B^0 \to J/\psi\,(e^+e^-)K^{*0}$ data, but shifted by the difference in μ_{B^0} for $B^0 \to K^{*0}e^+e^-$ and $B^0 \to J/\psi\,(e^+e^-)K^{*0}$, according to the MC. The α parameter, and the two widths are taken from the fit to the $B^0 \to K^{*0}e^+e^-$ MC. As the resolutions are expected to be different between data and MC (due to, for example, imperfect detector alignment, effects from the aging of the detector not modelled in the MC *etc.*), it is necessary to include a μ_B scale factor to account for the worse resolution in data with respect to the MC. This scaling is taken from a comparison of the fit parameters obtained from $B^0 \to J/\psi\,(e^+e^-)K^{*0}$ MC and the data, the value of which can be seen in Table 4.8 for each trigger category. However, in order to correctly determine the signal parameters from the data, a description of the background pdf

is also required.

Trigger category	μ_B scale factor
L0ElectronTOS	1.118 ± 0.025
L0HadronTOS	1.235 ± 0.092
L0TIS	1.165 ± 0.057

Table 4.8: μ_B scale factor to correct the width determined MC to that measured in the data, as found from $B^0 \to J/\psi\,(e^+e^-)K^{*0}$

4.8.2 Background distributions

For both $B^0 \to K^{*0}e^+e^-$ and $B^0 \to J/\psi\,(e^+e^-)K^{*0}$, two types of background are considered. Firstly, there is random combinatorial background consisting of tracks not all originating from the same B^0. This is modelled by an exponential function, the slope of which is left floating in the fit in both cases. Secondly, there is background arising from true B decays but with one or more tracks missing from the reconstruction. In the case of $B^0 \to J/\psi\,(e^+e^-)K^{*0}$, there are two sources for these partially reconstructed events: those from the hadronic part (such as events with higher K^* resonances), and those from the J/ψ part (such as events coming from $\psi(2S)$ decays). In order to study this background, 1.3 million inclusive $B^0/B^\mp \to J/\psi\,(e^+e^-)K^*X$ decays were simulated, and the selection cuts applied, as well as a veto on true $B^0 \to J/\psi\,(e^+e^-)K^{*0}$ events. The surviving events were split into those where the J/ψ comes from an excited charmonium resonance, and those where it comes from a B meson and thus attributed to partially reconstructed background coming from the hadronic part. These were fit using the RooKeysPdf class in RooFit, [80] which provides a non-parametric description of the distribution, an example of which can be seen in Fig. 4.22. The shapes found using the inclusive MC were fixed, and added to the background description in the fit to the $B^0 \to J/\psi\,(e^+e^-)K^{*0}$ data.

4.8.3 Fit to $B^0 \to K^{*0}e^+e^-$ data

$B^0 \to K^{*0}e^+e^-$ only suffers from the hadronic part of this background, and the ratio of this with respect to the signal is expected to be the similar as for $B^0 \to J/\psi\,K^{*0}$. The shape of the pdf of the hadronic part is therefore fixed from the inclusive MC,

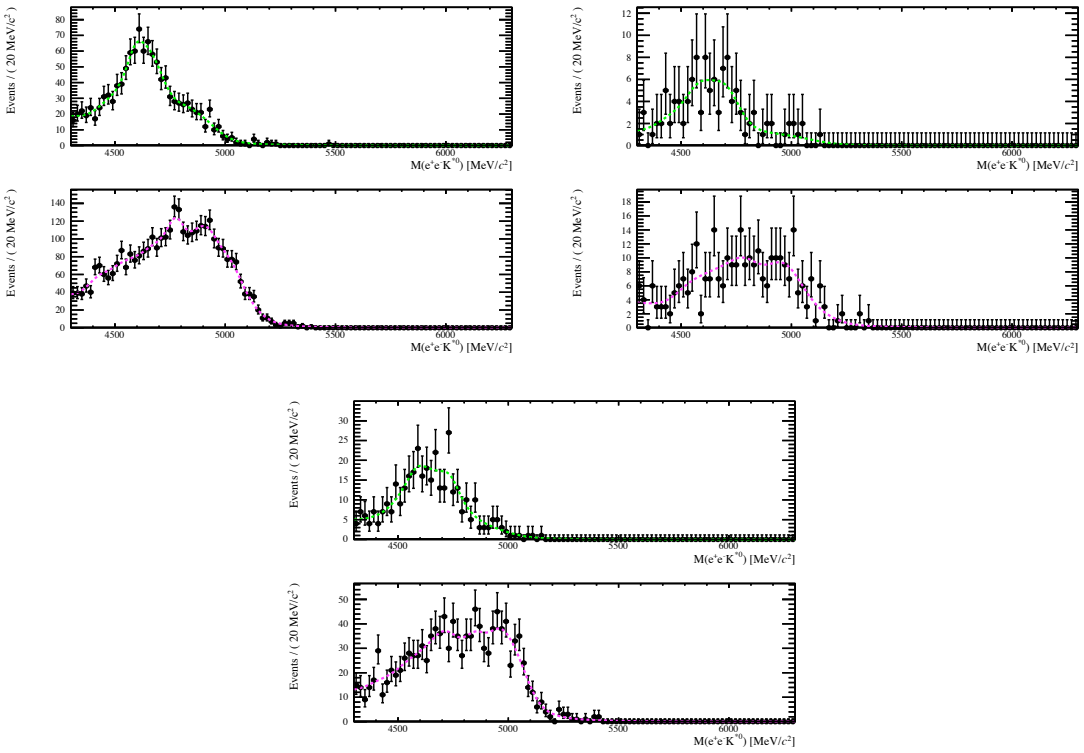

Figure 4.22: The background coming from partially reconstructed events due to missing particles from (above) the J/ψ part, and (below), hadronic part: a fit to the reconstructed B^0 mass for the three categories for the optimal BDT cut.

and the number of events with respect to the number of signal events is fixed from the ratio determined by the $B^0 \to J/\psi\, K^{*0}$ data. The ratio of partially reconstructed background to signal events is thus found to be 0.40. A verification of the amount of partially reconstructed background can be obtained by comparing this result to that obtained in the analysis of $B^0 \to K^{*0}\gamma$ [81]. Again, it is expected that the fraction of partially reconstructed background compared to the number of signal events, in the same mass range of $4.3\,\mathrm{GeV}/c^2$ to $5.3\,\mathrm{GeV}/c^2$, should be similar in both cases. In the case of $B^0 \to K^{*0}\gamma$, the partially reconstructed background is fitted assuming a mass distribution shape obtained from MC for the decay channels $B^\pm \to K^*\pi^\pm\gamma$ and $B^0 \to K^*\pi^0\gamma$. The $B^\pm \to K^*\pi^\pm\gamma$ contribution is reduced by a factor 0.6 in the $B^0 \to K^{*0}\gamma$ analysis by a rejection of extra tracks using an isolation cut. Thus the fitted result of 0.15±0.05 for the fraction should be corrected by a factor (2/1.6), yielding a prediction of 0.19±0.065. Due to the plausible presence

of more complex topology, such as $B \to K^*\pi\pi\gamma$, it is not excluded that the true number in $B^0 \to K^{*0}e^+e^-$ be larger. In any case, a factor of (1±0.5) is used as a systematical error on our $B^0 \to J/\psi\, K^{*0}$ estimate of partially reconstructed events in $B^0 \to K^{*0}e^+e^-$, as described in Section 4.11.4, thus covering the difference between the two evaluations.

There are therefore three parameters left floating in the fit to the $B^0 \to K^{*0}e^+e^-$ data: the slope of the exponential describing the combinatorial background, the number of combinatorial events, and the number of signal events.

As mentioned in Section 4.4.4, for each trigger category, the BDT and PID cuts applied were determined by optimising for the maximum $\frac{S}{\sqrt{(S+B)}}$. The value used for S was taken as the number expected in the $1\,\text{fb}^{-1}$ of data corresponding to the number of $B^0 \to K^{*0}e^+e^-$ MC found by the fit, for each PID and BDT cut, which lies within a mass window of ± 300 MeV/c^2 of the B^0 mass. As there are known discrepancies between the expected yields from MC and those measured in the data (see Section 4.9), this number is multiplied by a correction factor, determined using the ratio of $B^0 \to J/\psi\, K^{*0}$ MC to data events. The number of background is found from the combination of the combinatorial and partially reconstructed background within the same mass window as measured by the fit to the $B^0 \to K^{*0}e^+e^-$ data.

4.8.4 Fit results

The fit to the mass distributions following this procedure for the three trigger categories can be seen for the $B^0 \to K^{*0}e^+e^-$ ($B^0 \to J/\psi\, K^{*0}$) MC and data in Figures. 4.23 and 4.24 (4.25 and 4.26,) respectively.

The signal fit parameters and yields in the whole mass range are listed in Table 4.9 (4.10), and the yields in a B^0 mass window of $\pm 3\sigma$, along with the $\frac{S}{\sqrt{(S+B)}}$, are given in Table 4.11. The $\pm 3\sigma$ mass window was determined using the average resolution, as calculated from the two widths and the fraction of them in the CB, determined from the $B^0 \to K^{*0}e^+e^-$ MC, and multiplied by the MC to data μ_B scale factor. The correlation matrix for $B^0 \to K^{*0}e^+e^-$ is given in Tables 4.12-4.14.

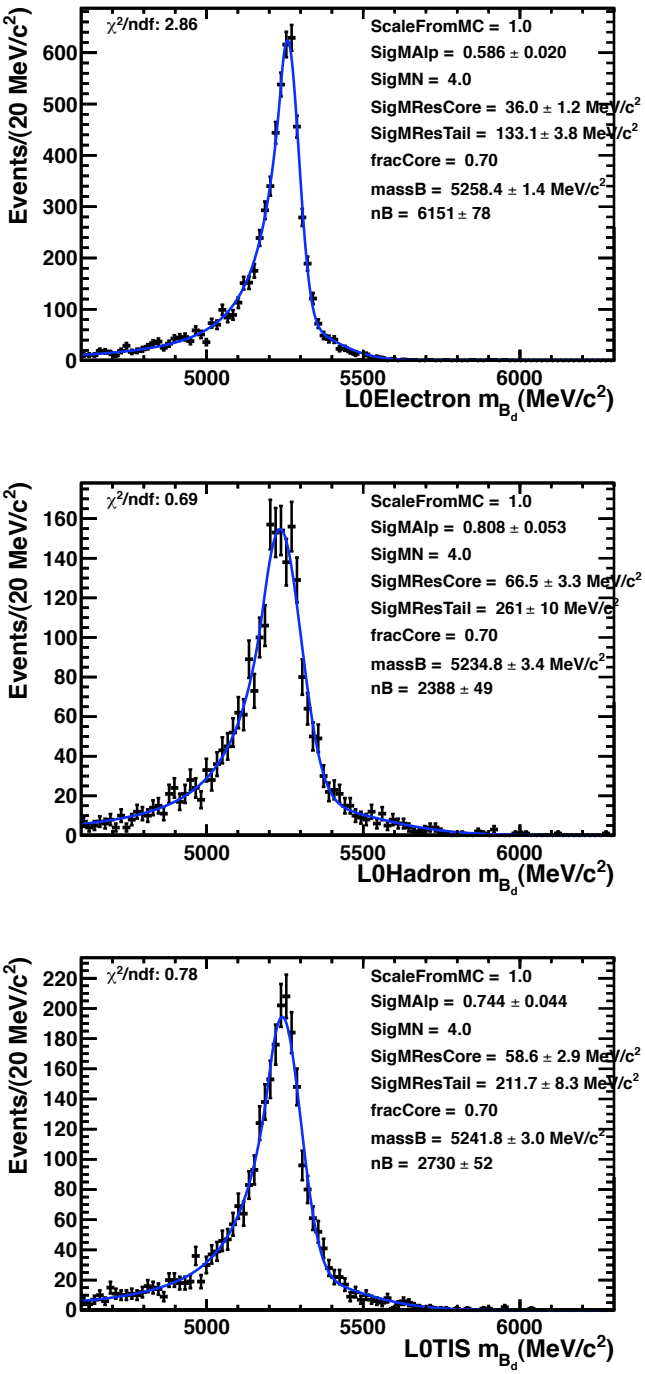

Figure 4.23: Fits to the B^0 mass passing the optimal BDT cuts for each trigger category for the $B^0 \to K^{*0} e^+ e^-$ MC sample.

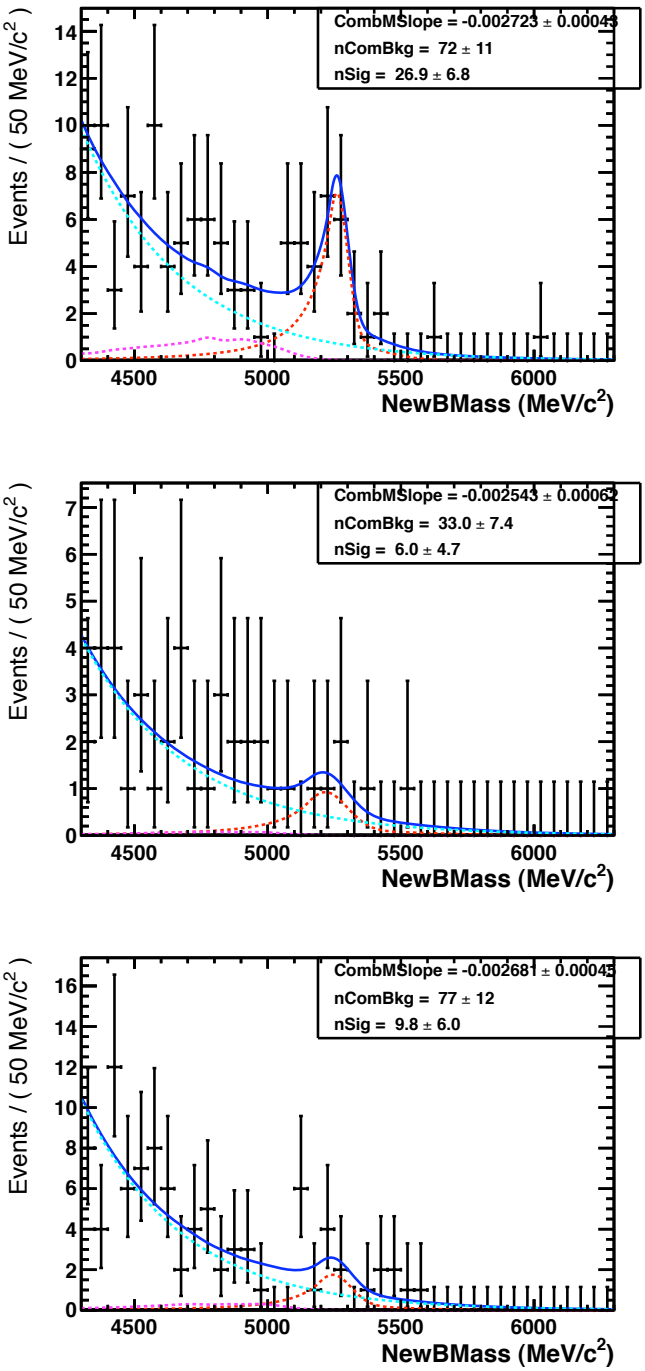

Figure 4.24: Fit to the signal data B^0 mass for each trigger category for the optimal BDT cuts.

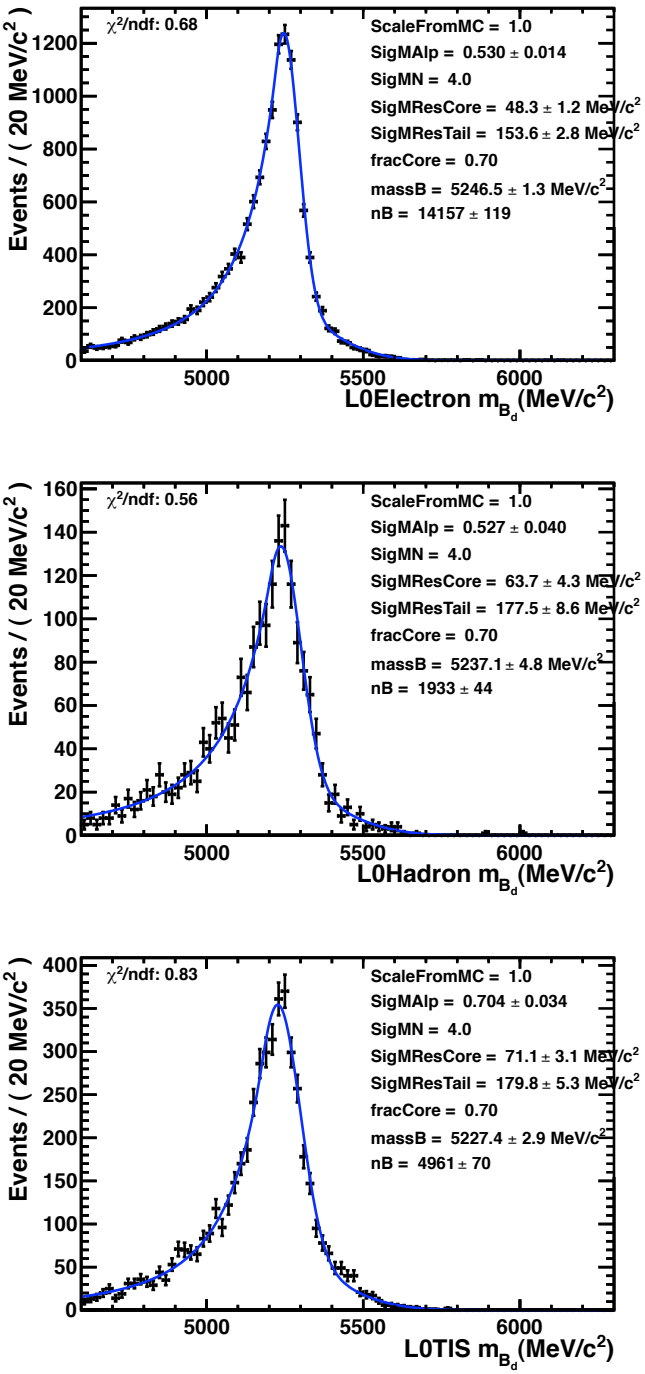

Figure 4.25: Fits to the B^0 mass passing the optimal BDT cuts for each trigger category for the $B^0 \to J/\psi(e^+e^-)K^{*0}$ MC sample.

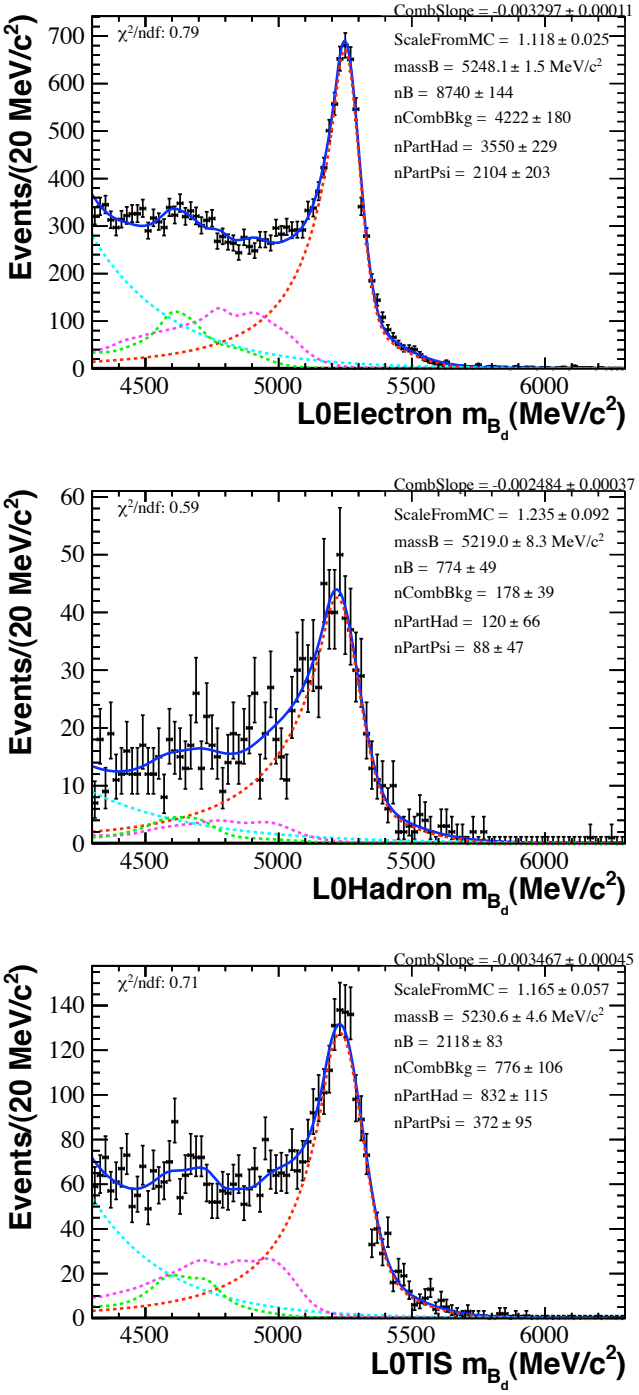

Figure 4.26: Fit to the $B^0 \to J/\psi\,(e^+e^-)K^{*0}$ data B^0 mass for each trigger category for the optimal BDT cut.

parameter	L0 Category	value	Fit status
μ_{B^0}	L0ElectronTOS	5260 ± 1.5 MeV/c^2	Fixed from $B^0 \to J/\psi(e^+e^-)K^{*0}$
	L0HadronTOS	5216.7 ± 8.3 MeV/c^2	data and shifted
	L0TIS	5245 ± 4.6 MeV/c^2	according to MC
σ_1	L0ElectronTOS	36.0 ± 1.2 MeV/c^2	Fixed from $B^0 \to K^{*0}e^+e^-$
	L0HadronTOS	66.5 ± 3.3 MeV/c^2	MC and multiplied
	L0TIS	58.6 ± 2.9 MeV/c^2	by μ_B scale factor
σ_2	L0ElectronTOS	133.1 ± 3.8 MeV/c^2	Fixed from $B^0 \to K^{*0}e^+e^-$
	L0HadronTOS	261.0 ± 10.5 MeV/c^2	MC and multiplied
	L0TIS	211.7 ± 8.3 MeV/c^2	by μ_B scale factor
μ_B scale factor	L0ElectronTOS	1.118 ± 0.025	
	L0HadronTOS	1.235 ± 0.092	Fixed from $B^0 \to J/\psi(e^+e^-)K^{*0}$
	L0TIS	1.165 ± 0.057	
fraction	L0ElectronTOS	0.7	
in CB	L0HadronTOS	0.7	Fixed
	L0TIS	0.7	
α	L0ElectronTOS	0.59 ± 0.020	
	L0HadronTOS	0.81 ± 0.053	Fixed from $B^0 \to K^{*0}e^+e^-$ MC
	L0TIS	0.74 ± 0.043	
comb slope	L0ElectronTOS	-0.002994± 0.00054	
	L0HadronTOS	-0.002593 ± 0.00079	Free
	L0TIS	-0.002700± 0.00053	
Ncomb	L0ElectronTOS	66.1± 11	
	L0HadronTOS	29.8 ± 7	Free
	L0TIS	75.5± 11	
Npart	L0ElectronTOS	11± 2	Npart+Nsig free and ratio of
	L0HadronTOS	1 ± 1	the two fixed from
	L0TIS	4± 2	$B^0 \to J/\psi(e^+e^-)K^{*0}$ data
Nsig	L0ElectronTOS	26.93 +7.10 -6.48	Npart+Nsig free and ratio of
	L0HadronTOS	6.04 +5.06 -4.26	the two fixed from
	L0TIS	9.84 +6.48 -5.54	$B^0 \to J/\psi(e^+e^-)K^{*0}$ data

Table 4.9: Summary of the fitted and fixed parameters and yields for $B^0 \to K^{*0}e^+e^-$.

parameter	L0 Category	value	Fit status
σ_1	L0ElectronTOS	48.3 ± 1.2 MeV/c^2	Fixed from $B^0 \to J/\psi K^{*0}$
	L0HadronTOS	63.7 ± 4.3 MeV/c^2	MC and multiplied
	L0TIS	71.1 ± 3.1 MeV/c^2	by μ_B scale factor
σ_2	L0ElectronTOS	153.6 ± 2.8 MeV/c^2	Fixed from $B^0 \to J/\psi K^{*0}$
	L0HadronTOS	177.5 ± 8.6 MeV/c^2	MC and multiplied
	L0TIS	180.0 ± 5.3 MeV/c^2	by μ_B scale factor
μ_B scale factor	L0ElectronTOS	1.118 ± 0.025	
	L0HadronTOS	1.235 ± 0.092	Free
	L0TIS	1.165 ± 0.057	
fraction	L0ElectronTOS	0.7	
in CB	L0HadronTOS	0.7	Fixed
	L0TIS	0.7	
α	L0ElectronTOS	0.53± 0.0137	
	L0HadronTOS	0.53 ± 0.040	Fixed from $B^0 \to J/\psi K^{*0}$ MC
	L0TIS	0.70 ± 0.034	
comb slope	L0ElectronTOS	-0.003297 ± 0.00011	
	L0HadronTOS	-0.002484 ± 0.00037	Free
	L0TIS	-0.003467 ± 0.00045	
Ncomb	L0ElectronTOS	4222± 180	
	L0HadronTOS	178 ± 39	Free
	L0TIS	776± 106	
NpartHad	L0ElectronTOS	3550± 230	Free
	L0HadronTOS	120 ± 66	
	L0TIS	832± 115	
NpartPsi	L0ElectronTOS	2104± 203	Free
	L0HadronTOS	88 ± 47	
	L0TIS	371± 95	
Nsig	L0ElectronTOS	8740± 144	Free
	L0HadronTOS	774 ± 49	
	L0TIS	2118±83	

Table 4.10: Summary of the fitted and fixed parameters and yields for $B^0 \to J/\psi\,(e^+e^-)K^{*0}$.

Trigger category	Signal yield in $\pm 3\sigma$ B^0 mass window	Combinatorics yield	Part reco yield	$S/\sqrt{(S+B)}$
L0ElectronTOS	22.4	6.9	1.1	4.06
L0HadronTOS	5.5	9.4	0.5	1.40
L0TIS	8.7	14.7	1.4	1.76

Table 4.11: $B^0 \to K^{*0}e^+e^-$ yields within the B^0 mass window.

Parameter	exponential slope	No. comb. background	No. signal
exponential slope	1	0.3258	-0.3822
No. comb. background	0.3258	1	-0.498
No. signal	-0.3822	-0.498	1

Table 4.12: The correlation matrix for the fitted parameters of $B^0 \to K^{*0}e^+e^-$ in the L0ElectronTOS category.

Parameter	exponential slope	No. comb. background	No. signal
exponential slope	1	0.3691	-0.5088
No. comb. background	0.3691	1	-0.5505
No. signal	-0.5088	-0.5505	1

Table 4.13: The correlation matrix for the fitted parameters of $B^0 \to K^{*0}e^+e^-$ in the L0HadronTOS category.

Parameter	exponential slope	No. comb. background	No. signal
exponential slope	1	0.4179	-0.5776
No. comb. background	0.4179	1	-0.5816
No. signal	-0.5776	-0.5816	1

Table 4.14: The correlation matrix for the fitted parameters of $B^0 \to K^{*0}e^+e^-$ in the L0TIS category.

4.9 Trigger independent comparison of $B^0 \to J/\psi\,(e^+e^-)K^{*0}$ and $B^0 \to J/\psi\,(\mu^+\mu^-)K^{*0}$.

Due to the low $B^0 \to K^{*0}e^+e^-$ yields, it is difficult to compare the expectations according to the MC and the observations, but there is a clear deficit between the predictions for $B^0 \to J/\psi\,(e^+e^-)K^{*0}$ (Table 4.7) and the number of events measured in the data, (Table 4.10.)

There are several factors which can lead to the MC providing an inaccurate description of the data. For example, it has been observed that the calorimeters suffer from aging effects due to running in a high occupancy environment, namely radiation damage to the scintillators and fibres, and degradation of the PMTs. This affects both the L0 trigger rates, and the energy reconstruction. This is now being monitored with calibrations applied during the current data-taking thus reducing the effects, but are not described in the MC here and can be one source of discrepancy. Furthermore, although the trigger configurations were kept relatively stable throughout the 2011 data taking period, there were still several different Trigger Configuration Keys (TCKs) used, whereas the MC is simulated using only one TCK, which uses IP information, which, as was shown in Section 4.3.1, is also known to differ from that of the data. This leads to expected differences in the trigger performance in data and MC.

It is therefore desirable to validate the yields using a method that does not rely on the MC, especially to check the electron performance, as there are few analysis containing lower p_{T} electrons carried out at LHCb. One such method is to compare the yields of $B^0 \to J/\psi\,(e^+e^-)K^{*0}$ to those of $B^0 \to J/\psi\,(\mu^+\mu^-)K^{*0}$.

4.9.1 Method

The SM predicts that events with the J/ψ decaying to e^+e^- should be equally as abundant as those decaying to $\mu^+\mu^-$. The main factor contributing to the much larger yields of the decays with muons is the trigger efficiency. The clean signature at the muon chambers means that the L0muon thresholds can be left relatively low, whereas the high occupancy at the calorimeters requires tighter L0 cuts.

By requiring that the events are TIS events, and thus triggered by a particle not forming the signal candidate, one can achieve a sample independent of the trigger

efficiency of muons vs. electrons. The correlation of the momenta of the two b quarks implies that the underlying event is not completely independent of the signal candidate, but with the similarity of the kinematics between the two decays under study, it is a good approximation.

Applying the same cuts to both trigger independent samples corresponding to data collected during the same period, one can expect to first order, to observe the same yields. The cuts shown in Table 4.15 are applied to both samples. They include those of the stripping lines used for both $B^0 \to J/\psi(\mu^+\mu^-)K^{*0}$ and $B^0 \to J/\psi(e^+e^-)K^{*0}$, with an arbitrary cut on the BDT placed at 0.95, thereby creating a suboptimal selection, but suitable for performing the comparison. The B^0 mass distributions after applying these cuts and requiring that the events are L0TIS are shown in Fig. 4.27. $B^0 \to J/\psi(\mu^+\mu^-)K^{*0}$ is fit using the same method as described in Section 4.8. $B^0 \to J/\psi(\mu^+\mu^-)K^{*0}$ is fit in a similar manner with a double CB for the signal mass distribution and an exponential for the combinatorial background, but the low mass background coming from partially reconstructed events is modeled by a RooExpAndGaus function. This models an exponential rise to a threshold, above which there is a Gaussian fall off.

There may still be a bias due to the HLT1 and HLT2 triggers, and so it is also required that the events are TIS events throughout the entire trigger chain, although this reduces the available statistics. The B^0 mass distributions which are TIS at all stages of the trigger sequence can be seen in Fig. 4.28 and the yields are summarised in Table 4.16. Due to technical reasons, the amount of collected luminosity is not exactly the same in the two samples, so the yield for the muon events requires a further correction factor of 0.95.

As can be seen, there is $\approx$ a factor 3 more muon events than electron, even with the trigger independent sample. There are, however, several other effects contributing to the loss of the electron events.

4.9.2 Effects on the electron efficiency

4.9.2.1 Effect of Bremsstrahlung radiation on the J/ψ mass

One expected loss for the decay to two electrons as compared to two muons after eliminating trigger effects comes from the efficiency of the mass cut on the J/ψ mass. The final selection cuts on the J/ψ mass window were loosened to those of

Table 4.15: Selection used for $B^0 \to J/\psi(\mu^+\mu^-)K^{*0}$ and $B^0 \to J/\psi(e^+e^-)K^{*0}$ in order to compare the yields.

Particle	Cuts for e^+e^- $\mu^+\mu^-$ comparison
B	Vertex χ^2 <30
	IP χ^2 <16
	IP <0.05 mm
	FD χ^2 >121
	FD χ^2 <100000
	θ $_{\text{flight}}$ <14 mrad
K^{*0}	Δ $m_{K^{*0}}$ 130 MeV/c^2
	Vertex χ^2 <12
	IP χ^2 >1
	FD χ^2 >9
	DIRA >-0.9
e^+e^- (J/ψ)	$m_{J/\psi}$= 2400-3400 MeV/c^2
	Vertex χ^2 <12
	FD >9
	DIRA >-0.9
K	p_{T} >400 MeV/c
	p >3000 MeV/c
	Track χ^2 <5
	IP χ^2 >9
	DLL$_{K\pi}$ >0
	CloneDist<0
π	p_{T} >300 MeV/c
	p >3000 MeV/c
	Track χ^2 <5
	IP χ^2 >9
	DLL$_{K\pi}$ <5
	CloneDist<0
e	p_{T} >300 MeV/c
	p_{T} <25000 MeV/c
	Track χ^2 <5
	IP χ^2 >9
	DLL$_{e\pi}$ >-2
	CloneDist0
	$\Sigma_{i=e^+,e^-,K,\pi}$IPS(i)>20
	BDT cut >0.95

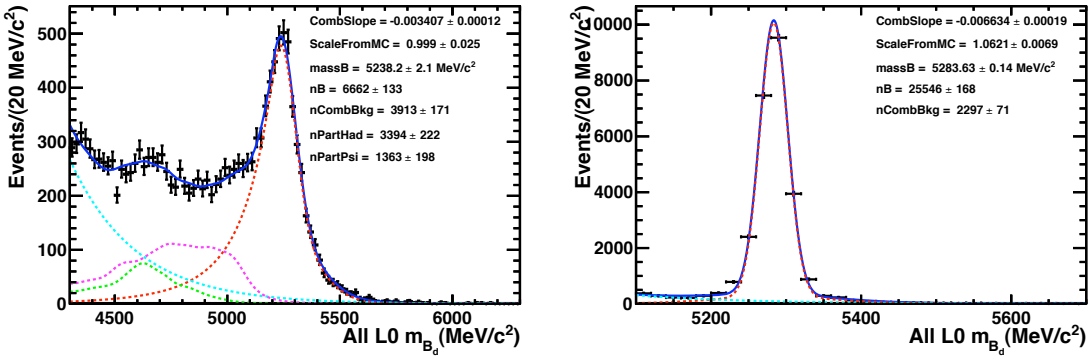

Figure 4.27: B^0 mass distribution of L0TIS $B^0 \to J/\psi\,(e^+e^-)K^{*0}$ (left) and $B^0 \to J/\psi\,(\mu^+\mu^-)K^{*0}$ (right) events.

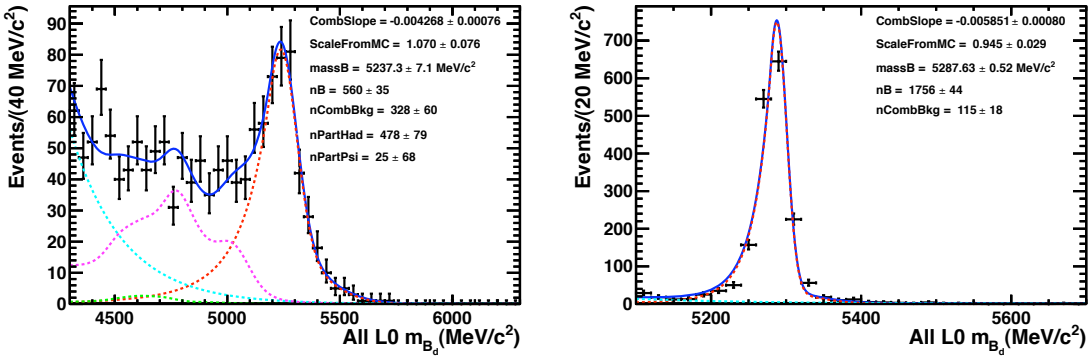

Figure 4.28: B^0 mass distribution of L0TIS*Hlt1TIS*Hlt2TIS $B^0 \to J/\psi\,(e^+e^-)K^{*0}$ (left) and $B^0 \to J/\psi\,(\mu^+\mu^-)K^{*0}$ (right) events.

the stripping cuts, and a fit was performed to the J/ψ mass distribution of both the electron and muon data, as can be seen in Fig. 4.29. The same fit was applied in both cases, using the same double CB function and fitting procedure as that for the B^0 mass, as is described in Section 4.8, with an additional double CB in the case of $B^0 \to J/\psi\,(e^+e^-)K^{*0}$ to fit the small peak from $\psi(2S)$. The stripping cut in the muon decay does not extend to the $\psi(2S)$ mass.

The much heavier mass of the muon means that uniquely the electron decay suffers from a pronounced loss of energy due to bremsstrahlung radiation, and so the chosen mass range of (2400-3400) MeV/c^2 removes 6% of the signal events in the tail, whereas the range used for the muon range at stripping level, (2800-3300)

Table 4.16: The measured yields for $B^0 \to J/\psi(e^+e^-)K^{*0}$ and $B^0 \to J/\psi(\mu^+\mu^-)K^{*0}$ for a trigger independent data sample. The yield for the muon events is corrected by a factor 0.95 to account for the difference in luminosity collected for the two samples.

Trigger category	$B^0 \to J/\psi(e^+e^-)K^{*0}$ (no. events)	$B^0 \to J/\psi(\mu^+\mu^-)K^{*0}$ (no. events) $\times$ lumi 0.95 correction factor	Ratio
L0TIS	6662 ± 133	24760 ± 184	3.72 ± 0.08
FullTIS	560 ± 35	1681 ± 44	3.0 ± 0.2

MeV/c^2 is 100% efficient on the muon decay.

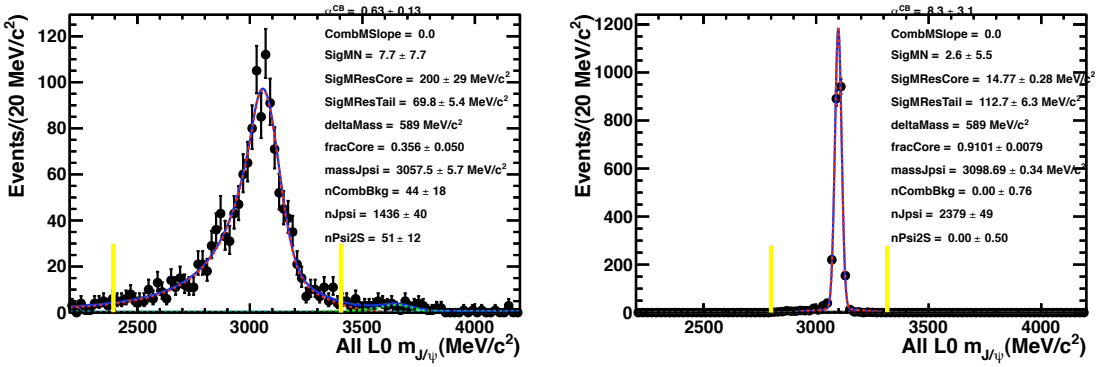

Figure 4.29: J/ψ mass distribution of L0TIS*Hlt1TIS*Hlt2TIS $B^0 \to J/\psi(e^+e^-)K^{*0}$ (left) and $B^0 \to J/\psi(\mu^+\mu^-)K^{*0}$ (right) events. The yellow lines indicate the cut values used in the selection.

4.9.2.2 Calorimeter acceptance

The main criteria used for identification of an electron comes from the measurement of its energy divided by its momentum, which requires information from the ECAL. Due to its proximity to the interaction point, the ECAL suffers from high occupancy and radiation damage, especially at low polar angles. For this reason, the sensitive region starts at from $|x|$=363.6 mm and $|y|$ = 282.6 mm, whereas the muon chambers have a larger acceptance. By extrapolating the muon tracks to the

ECAL plane, the number of events that would have been lost had the tracks required ECAL information can be calculated. These extrapolated x and y positions for the entirely TIS $B^0 \to J/\psi\,(\mu^+\mu^-)K^{*0}$ data can be seen in Fig. 4.30. 14 % of the candidates had one or both muon tracks passing through the ECAL hole, and thus wouldn't be reconstructed in the case of $B^0 \to J/\psi\,(e^+e^-)K^{*0}$.

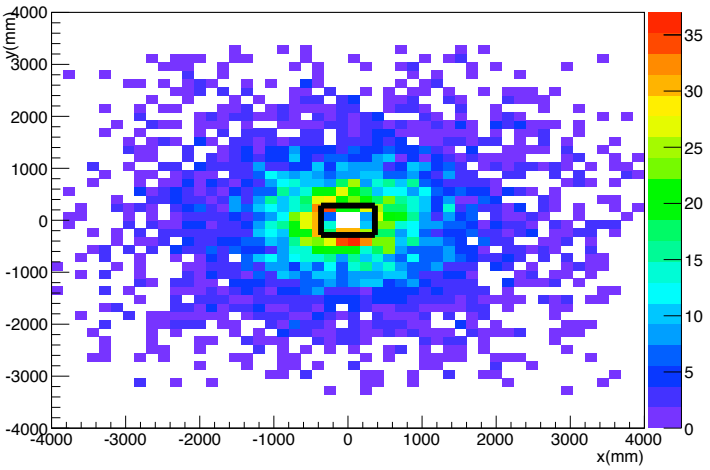

Figure 4.30: The x and y positions of the muon tracks extrapolated to the ECAL plane for the $B^0 \to J/\psi\,(\mu^+\mu^-)K^{*0}$ TIS data. The black lines mark the region of the ECAL hole.

4.9.2.3 Electron Identification

The efficiency of the electron particle identification (PID) cut for the electrons coming from $B^0 \to J/\psi\,(e^+e^-)K^{*0}$ was computed from data using the efficiency tables calculated from the 'tag and probe' method as described in Section 4.10.2.4. This efficiency as a function of p_{T} was convoluted with the p_{T} spectrum of the fully TIS $B^0 \to J/\psi\,(e^+e^-)K^{*0}$ MC electrons in order to get the overall efficiency, which was calculated to be 0.91. Assuming the muon PID cut to be 100% efficient, a further reduction factor of 0.91^2 is expected for the electron decay as compared to the muon decay.

4.9.2.4 Inherent reconstruction,tracking and selection differences

Due to the bremsstrahlung emission by the electrons, it can be expected that the tracking efficiency is not as high as for muons, for example it can be imagined that the case occurs where so much bremsstrahlung radiation is emitted, the electron no longer has enough momentum to traverse the whole detector, or p_{T} to pass the selection cut. This is checked by comparing the overall efficiency, including reconstruction, tracking and selection from MC, again using events that are TIS along the entire trigger chain to avoid trigger biases and a loose PID requirement ($\mathrm{DLL}_{e\pi}$ or $\mathrm{DLL}_{\mu\pi}$ >-2). The ratio of the number of $B^0 \to J/\psi\,(e^+e^-)K^{*0}$ events selected over the number generated to the ratio of $B^0 \to J/\psi\,(\mu^+\mu^-)K^{*0}$ events selected over the number generated is found to be 0.46. This however, includes the 6% loss on the electrons due to the J/ψ mass cut, and the 14% due to the calorimeter acceptance. Therefore, the tracking efficiency $\epsilon_{\mathrm{tracking}}$ is determined by:

$$\begin{aligned} 0.46 &= 0.94 \times 0.86 \times \epsilon_{\mathrm{tracking}} \times \epsilon_{\mathrm{tracking}} \\ \epsilon_{\mathrm{tracking}} &= 0.75 \end{aligned} \tag{4.9}$$

Therefore, according to the MC, an electron track is 75% as likely to be found as a muon track.

4.9.3 Final yield validation

Combining all the factors contributing to the loss of electron events as listed above, and also taking into account the slight difference in luminosity of the two samples, the number of $B^0 \to J/\psi\,(e^+e^-)K^{*0}$ events expected is equal to:

$$\begin{aligned} &\mathrm{Nsig}_{B^0\to J/\psi\,(\mu^+\mu^-)K^{*0}} \times \epsilon_{J/\psi\,\mathrm{mass}} \times \epsilon_{\mathrm{calo\ accept.}} \times \epsilon_{\mathrm{PIDe}} \times \epsilon_{\mathrm{tracking}} \times \frac{\mathcal{L}_{B^0\to J/\psi\,(e^+e^-)K^{*0}}}{\mathcal{L}_{B^0\to J/\psi\,(\mu^+\mu^-)K^{*0}}} \\ &= 1768 \times 0.94 \times 0.86 \times 0.91^2 \times 0.75^2 \times 0.95 \\ &= 632 \text{ events} \\ &= 1.13 \times B^0 \to J/\psi\,(e^+e^-)K^{*0} \text{ events observed} \end{aligned} \tag{4.10}$$

The statistical error on the ratio of the number of signal from the events which are completely independent of the trigger is found to be 7%. Due to technical reasons, the data sample used for the decay with electrons in the final state is not completely the same as that with muons, so the error on the luminosity measurement of 3.5% should also be taken into account. It therefore seems that within errors, the observed $B^0 \to J/\psi(e^+e^-)K^{*0}$ yield is compatible with that expected from $B^0 \to J/\psi(\mu^+\mu^-)K^{*0}$, once all trigger effects have been removed.

4.10 Extraction of the branching fraction

The ratio of the branching fractions is calculated from the ratio of the number of events as determined by the fits, normalised to the efficiency ratio:

$$\frac{\mathcal{B}(B^0 \to K^{*0}e^+e^-)^{30-1000\,\mathrm{MeV}/c^2}}{\mathcal{B}(B^0 \to J/\psi\, K^{*0})} = \frac{\mathrm{Nsig}_{B^0\to K^{*0}e^+e^-}}{\mathrm{Nsig}_{B^0\to J/\psi\, K^{*0}}} \frac{\epsilon_{B^0\to J/\psi\, K^{*0}}}{\epsilon_{B^0\to K^{*0}e^+e^-}} \tag{4.11}$$

The efficiency ratio is expected to be different for each trigger category, primarily due to the higher electron p_{T} spectrum in $B^0 \to J/\psi\, K^{*0}$, creating differences, for example, in the L0 trigger efficiency. In order to eliminate the dependence on the MC to correctly describe the relative abundance of events falling within each of the three trigger categories, it is necessary to compute the branching fraction ratio separately for each category, before combining to form an average.

4.10.1 Ratio of signal yields

The signal yields are taken from the numbers determined by the unbinned maximum likelihood fit to data as described in Section 4.8.4. However, as already noted, this includes contamination from . The fraction of the measured yield expected to arise from misidentified $B^0 \to K^{*0}\gamma$ events, for each trigger category, was determined using MC, as described in Section 4.6.1. This fraction for each trigger category is given in Table 4.17. For all categories, it is compatible with 10%, and this value is used to correct the $B^0 \to K^{*0}e^+e^-$ yields, also given in Table 4.17.

As a crosscheck that this contamination fraction can be taken from MC, the fraction of events removed from data by the $B^0 \to K^{*0}\gamma$ veto were compared to those from MC. With all cuts except the veto, the MC predicts 69 $B^0 \to K^{*0}e^+e^-$ events, and 25 $B^0 \to K^{*0}\gamma$ events. Including the veto, these numbers become 61

Trigger category	Corrected $B^0 \to K^{*0}e^+e^-$ yields	
L0ElectronTOS	9%	24.9 +6.9 -6.3
L0HadonTOS	12%	5.6 +4.4 -3.7
L0TIS	10%	9.4 +5.8 -5.0

Table 4.17: The fraction of the $B^0 \to K^{*0}\gamma$ events contributing to the $B^0 \to K^{*0}e^+e^-$ yields, as determined by MC, and the corrected yields in 1 fb^{-1}.

Trigger category	No veto	veto	ratio
L0ElectronTOS	37	27	0.73
L0HadonTOS	5	6	0.8
L0TIS	16	11	0.69

Table 4.18: The number of 'signal' events measured in each trigger category with and without the veto on $B^0 \to K^{*0}\gamma$ events, and the ratio of the two. The ratio according to MC is found to be 70%.

and 5, respectively. Thus, one expects a reduction of $\approx 30\%$ in the total number of events when applying the veto. This is in reasonable agreement with the numbers seen from data, with slight variation across the trigger cateogries, as seen in Table 4.18.

The ratios of the yields, in each trigger category, are thus found to be:

$$\frac{\text{Nsig}_{\text{ L0ElectronTOS } B^0\to K^{*0}e^+e^-}}{\text{Nsig}_{\text{ L0ElectronTOS } B^0\to J/\psi K^{*0}}} = 0.00277^{+0.00073}_{-0.00067} \tag{4.12}$$

$$\frac{\text{Nsig}_{\text{ L0HadronTOS } B^0\to K^{*0}e^+e^-}}{\text{Nsig}_{\text{ L0HadronTOS } B^0\to J/\psi K^{*0}}} = 0.00740^{+0.00623}_{-0.00525} \tag{4.13}$$

$$\frac{\text{Nsig}_{\text{ L0TIS } B^0\to K^{*0}e^+e^-}}{\text{Nsig}_{\text{ L0TIS } B^0\to J/\psi K^{*0}}} = 0.00418^{+0.00276}_{-0.00236} \tag{4.14}$$

where the error is statistical only.

4.10.2 Ratio of efficiencies

The efficiency ratio, $\frac{\epsilon_{B^0\to K^{*0}e^+e^-}}{\epsilon_{B^0\to J/\psi K^{*0}}}$ from Equation 4.11 includes contributions from the acceptance, reconstruction and preselection, trigger, PID, the BDT cut and the

efficiency of the cut on the dilepton mass window, and can be written as:

$$\frac{\epsilon_{B^0\to J/\psi K^{*0}}}{\epsilon_{B^0\to K^{*0}e^+e^-}} = \frac{\epsilon^{B^0\to J/\psi K^{*0}}_{\text{Acceptance}}}{\epsilon^{B^0\to K^{*0}e^+e^-}_{\text{Acceptance}}} \times \frac{\epsilon^{B^0\to J/\psi K^{*0}}_{\text{Reco\&Sel}}}{\epsilon^{B^0\to K^{*0}e^+e^-}_{\text{Reco\&Sel}}} \times \frac{\epsilon^{B^0\to J/\psi K^{*0}}_{\text{Trigger}}}{\epsilon^{B^0\to K^{*0}e^+e^-}_{\text{Trigger}}} \times \frac{\epsilon^{B^0\to J/\psi K^{*0}}_{\text{PID}}}{\epsilon^{B^0\to K^{*0}e^+e^-}_{\text{PID}}} \times \frac{\epsilon^{B^0\to J/\psi K^{*0}}_{\text{BDT}}}{\epsilon^{B^0\to K^{*0}e^+e^-}_{\text{BDT}}} \times \frac{\epsilon^{B^0\to J/\psi K^{*0}}_{\text{mass}}}{\epsilon^{B^0\to K^{*0}e^+e^-}_{\text{mass}}} \tag{4.15}$$

Each contribution is discussed briefly in the following.

4.10.2.1 Ratio of acceptance efficiencies

As the LHCb detector is built in the forward direction, all tracks must lie within a 400 mrad cone in order to be reconstructed. This geometrical efficiency is well described by the MC and are computed by GAUSS [82], as cuts are applied at the generator level, before reconstruction, in order to avoid the generation of events with final state particles lying outside the acceptance of LHCb. It is the sole contribution to the efficiency ratio which is independent of the trigger configuration. The relevant values are shown in Table 4.19, from which the ratio of acceptance efficiencies are calculated to be:

$$\frac{\epsilon^{B^0\to J/\psi K^{*0}}_{\text{Acceptance}}}{\epsilon^{B^0\to K^{*0}e^+e^-}_{\text{Acceptance}}} = 0.955 \pm 0.004. \tag{4.16}$$

Table 4.19: Summary of the acceptance efficiencies, as determined by simulation.

	Magnet Up(%)	Magnet Down(%)	Average(%)
$B^0 \to J/\psi K^{*0}$	14.80 ± 0.05	14.84 ± 0.05	14.82 ± 0.04
$B^0 \to K^{*0}e^+e^-$	15.51 ± 0.04	15.54 ± 0.06	15.52 ± 0.04

4.10.2.2 Reconstruction and preselection efficiencies

As described in Section 4.4, the same selection was applied to both $B^0 \to J/\psi K^{*0}$ and $B^0 \to K^{*0}e^+e^-$ apart from the invariant mass range of the e^+e^- pair, so that the selection efficiencies cancel in the ratio, as far as possible. However, due to the slightly different kinematics, the ratio is not expected to equal unity, exactly. The total selection efficiencies, including reconstruction, stripping and preselection

cuts, are determined from MC simulation. The efficiency of the PID cuts are not included in this ratio, as it is known that the PID information is not well represented in the MC, and thus they are treated separately. The reconstruction efficiency of the dilepton mass cut is also not included here, although the samples are required to have been generated within the correct mass ranges.

The combined reconstruction and stripping efficiencies, and the efficiency of each preselection cut used, applied to the stripping in each trigger category, are given for the two channels in Tables 4.20 and 4.21.It should be noted that the overall stripping efficiencies given include the effects from the HLT1 and HLT2 trigger (but the L0 trigger is treated separately). The overall ratios of reconstruction and selection efficiencies in each category not including PID, BDT, or the L0 trigger, (but including the Hlt efficiencies,) are:

$$\frac{\epsilon^{B^0\to J/\psi K^{*0}}_{\text{Reco\&Sel L0ElectronTOS}}}{\epsilon^{B^0\to K^{*0}e^+e^-}_{\text{Rec\&Sel L0ElectronTOS}}} = 1.22 \pm 0.03 \tag{4.17}$$

$$\frac{\epsilon^{B^0\to J/\psi K^{*0}}_{\text{Reco\&Sel L0HadronTOS}}}{\epsilon^{B^0\to K^{*0}e^+e^-}_{\text{Rec\&Sel L0HadronTOS}}} = 1.28 \pm 0.05 \tag{4.18}$$

$$\frac{\epsilon^{B^0\to J/\psi K^{*0}}_{\text{Reco\&Sel L0TIS}}}{\epsilon^{B^0\to K^{*0}e^+e^-}_{\text{Rec\&Sel L0TIS}}} = 1.21 \pm 0.04 \tag{4.19}$$

where the error comes from the available MC statistics.

4.10.2.3 L0 Trigger efficiencies

The L0 trigger efficiencies for each category are calculated using efficiency tables, which are described in [83]. Samples of well identified kaons and pions coming from D^0, triggered independently of the signal are collected, thus allowing for the calculation of the L0HadronTOS efficiency as a function of the transverse momentum of tracks for K^+, K^-, π^+ and π^-. A similar table was created for electrons, using $e^\pm$ from $B^0 \to J/\psi K^{*0}$ where the event had been triggered by the L0Hadron line. All selection cuts were applied to the MC samples, and the $p_{\rm T}$ spectra were used to determine the trigger efficiency for each trigger category.

The L0ElectronTOS efficiency was computed by combining the efficiencies corresponding to the $p_{\rm T}$ of each of the two electron tracks, and supposing that at least one of them triggers, *i.e*, if the efficiencies of the two electrons are $\epsilon_{\rm L0ElectronTOS}(p_1)$

Table 4.20: Efficiencies of the stripping selection, and the preselection and BDT cuts for each trigger category for $B^0 \to K^{*0} e^+ e^-$.

Particle	Selection variable	L0ElectronTOS (%)	L0HadronTOS (%)	L0TIS(%)
-	Stripping	2.54	2.43	2.41
B	Vertex χ^2	98.7	99	99.1
	IP χ^2	100	100	100
	FD χ^2	98.8	99.3	99.6
	θ flight	96.3	97.5	94.3
K^{*0}	Vertex χ^2	99.0	98.6	99.3
e	p_{T}	100	100	100
-	$\Sigma_{i=e^+,e^-,K,\pi}$IPS(i)	96.1	96.3	95.7
	e^+e^- Z error (mm)	95.6	94.1	94.1
	first z measurement (mm)	93.6	86.6	88.1
	K^* e Mass	96	98.7	99
	ϕ veto	99.2	99.5	98.9
	BDT	85.9	89.3	75.3

and $\epsilon_{\mathrm{L0ElectronTOS}}(p_2)$, the total L0ElectronTOS efficiency of an event is:

$$\epsilon_{\mathrm{L0ElectronTOS}}(p_1) \times (1 - \epsilon_{\mathrm{L0ElectronTOS}}(p_2)) + \epsilon_{\mathrm{L0ElectronTOS}}(p_2) \times (1 - \epsilon_{\mathrm{L0ElectronTOS}}(p_1)) + \epsilon_{\mathrm{L0ElectronTOS}}(p_1) \times \epsilon_{\mathrm{L0ElectronTOS}}(p_2) \tag{4.20}$$

This is calculated for each event, and then averaged to find the overall L0ElectronTOS efficiency.

The efficiency of the L0HadronTOS requirement is calculated in a similar manner, except it is also required that each event is not L0ElectronTOS.

As the L0TIS requirement means that the event was triggered by the other B meson in the event, independently of the signal, the efficiency is presumed to be equal for $B^0 \to K^{*0} e^+ e^-$ and $B^0 \to J/\psi K^{*0}$, and thus cancels out in the measurement of the ratio of branching ratios. However, as this category also explicitly requires that the event was not triggered by the signal, it is necessary to calculate the probability for each event that the signal did not trigger the L0Hadron or L0Electron lines. The ratio of trigger efficiencies for the L0TIS category is therefore the ratio of the 'not TOS' efficiency. The relevant trigger efficiencies for each category are shown in

Table 4.21: Efficiencies of the stripping selection, and the preselection and BDT cuts for each trigger category for $B^0 \to J/\psi\, K^{*0}$

Particle	Selection variable	L0ElectronTOS (%)	L0HadronTOS (%)	L0TIS (%)
-	Stripping	5.0	4.84	4.65
B	Vertex χ^2	99	98.8	99.3
	IP χ^2	100	100	100
	FD χ^2	98.6	98.6	99.5
	θ flight	97.5	98.1	95.5
K^{*0}	Vertex χ^2	98.8	98.6	99
e	p_{T}	100	100	100
-	$\Sigma_{i=e^+,e^-,K,\pi}$IPS(i)	97.1	97.1	96.7
	e^+e^- Z error (mm)	100	100	100
	first z measurement (mm)	90.1	86.6	87
	K^* e Mass	87.7	87.4	85.7
	ϕ veto	98.3	99.1	98.1
	BDT	78.9	80.5	70.3

Tables 4.22 and 4.23, which give the ratios of trigger efficiencies as,

$$\frac{\epsilon^{B^0\to J/\psi\, K^{*0}}_{\text{Trigger L0ElectronTOS}}}{\epsilon^{B^0\to K^{*0}e^+e^-}_{\text{Trigger L0ElectronTOS}}} = 1.41 \pm 0.02 \tag{4.21}$$

$$\frac{\epsilon^{B^0\to J/\psi\, K^{*0}}_{\text{Trigger L0HadronTOS}}}{\epsilon^{B^0\to K^{*0}e^+e^-}_{\text{Trigger L0HadronTOS}}} = 0.50 \pm 0.01 \tag{4.22}$$

and

$$\frac{\epsilon^{B^0\to J/\psi\, K^{*0}}_{\text{Trigger L0TIS}}}{\epsilon^{B^0\to K^{*0}e^+e^-}_{\text{Trigger L0TIS}}} = 0.89 \pm 0.01 \tag{4.23}$$

It should be noted that the sum of the efficiencies for L0ElectronTOS, L0HadronTOS and 'not TOS' is not equal to unity due to the fact that the BDT selection is dependent on the category.

As expected, the ratio is greater than 1 for the L0ElectronTOS events, as $B^0 \to J/\psi\, K^{*0}$ has electrons with higher p_{T}, and therefore a larger efficiency. Conversely, the ratio for L0HadronTOS events is less than 1 due to the higher average p_{T} of the kaon/pion for $B^0 \to K^{*0}e^+e^-$.

Table 4.22: Summary of the trigger efficiencies for $B^0 \to J/\psi K^{*0}$.

Trigger category	ϵ_{L0} (%)
L0ElectronTOS	42.1 ± 0.5
L0HadronTOS	6.0 ± 0.1
'not TOS' (for calculation of L0TIS ratio)	53.9 ± 0.5

Table 4.23: Summary of the trigger efficiencies for $B^0 \to K^{*0} e^+ e^-$.

Trigger category	ϵ_{L0} (%)
L0ElectronTOS	30.0 ± 0.4
L0HadronTOS	12.0 ± 0.1
'not TOS' (for calculation of L0TIS ratio)	60.3 ± 0.4

4.10.2.4 PID efficiencies

The efficiency of the PID cuts are calculated for the electrons using the 'tag and probe' method, described in the following. In order to produce a clean sample of $J/\psi \to e^+e^-$ from the data, a tight PID cut, $\text{DLL}_{e\pi}$ >5 is placed on one of the electrons. The efficiency for the final selection $\text{DLL}_{e\pi}$ cut of >1, can then be calculated using the other electron of the pair, as no PID cut is required to select it.

It is assumed that the efficiency of a cut on the $\text{DLL}_{e\pi}$ of a track is dependent on certain track kinematics, and so, a signal electron should have the same PID efficiency as a function of these kinematical variables as the collected calibration sample. From simulation, it has been shown the most sensitive variables are the momentum and η (pseudo-rapidity) of the track, but the available statistics of the calibration electron sample motivate the choice of binning in p_{T} alone.

In order to calculate the efficiency, for eight bins p_{T}, a requirement is placed on the 'probe' leg, of $\text{DLL}_{e\pi}$ >1, and the mass distribution is fit with one double crystal ball for the J/ψ, and another for the small $\psi(2S)$ contribution, with the difference between the two fixed to the difference calculated from the PDG values. All shape parameters are then fixed to the values determined by the fit, and the procedure is repeated with no cut on the PIDe of the 'probe' electron in order to calculate the efficiency. An example of the two fits for one p_{T} bin is shown in Fig. 4.31. The

efficiency of the selection cut, PIDe >1 as a function of p_{T} for e^- is shown in Fig. 4.32 with the corresponding values for both e^-, e^+ and the average shown in Table 4.24.

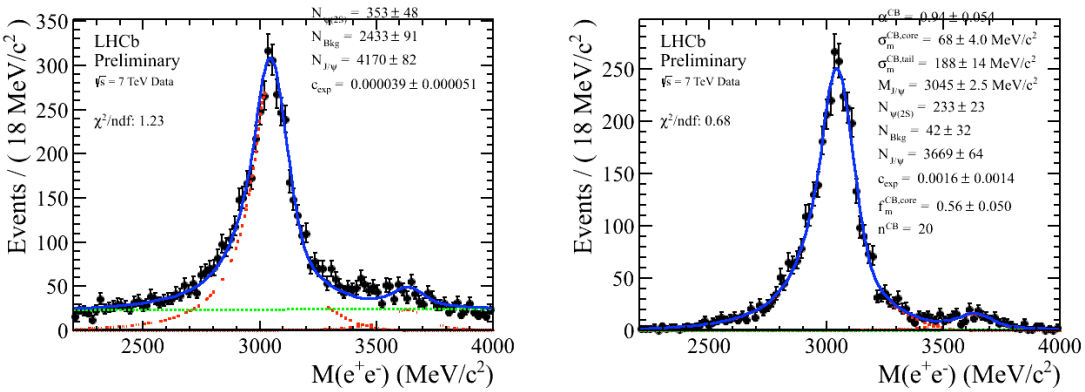

Figure 4.31: J/ψ mass distribution of $J/\psi \to e^+e^-$ with a tight PID requirement on one electron and with none on the other (left) and $\mathrm{DLL}_{e\pi}$ >1 (right) for p_{T} [1000-15000] MeV/c. The red dotted lines show the J/ψ and $\psi(2S)$ contributions, the green dotted line shows the exponential background and the solid blue line shows the total PDF.

These efficiency tables were then used in conjunction with the MC after all other cuts, for each trigger category separately, in order to determine the e^+e^- efficiency on an event by event basis according to the p_{T}. These were averaged to give the overall efficiencies, which are given for $B^0 \to J/\psi K^{*0}$ and $B^0 \to K^{*0}e^+e^-$ in Tables 4.25 and 4.26, respectively.

The PID efficiencies for the K^{*0} were similarly calculated using the standard PID Calibration Package [78]. In this case, the charm cross-section at LHCb is exploited, and large samples of $D^{*\pm} \to D^0(K^-\pi^+)\pi^\pm$, are used to provide clean samples of kaons and pions, selected by cuts on the kinematics only. The remaining residual backgrounds are removed using the splot [74] method. As no requirement is placed on the PID, these calibration samples provide the true $\mathrm{DLL}_{K\pi}$ distributions. The greater available statistics allowed for the calibration samples to be binned in both p_{T} and η. As the p_{T} and η distributions are well described by the MC, the $B^0 \to K^{*0}e^+e^-/B^0 \to J/\psi\,(e^+e^-)K^{*0}$ MC samples, after all the final cuts other than the PID requirements, were then used to re-weight the calibration kaons and pions in 25 bins in momentum and 4 bins in η. The efficiency of the $\mathrm{DLL}_{K\pi}$ <5 cut on the

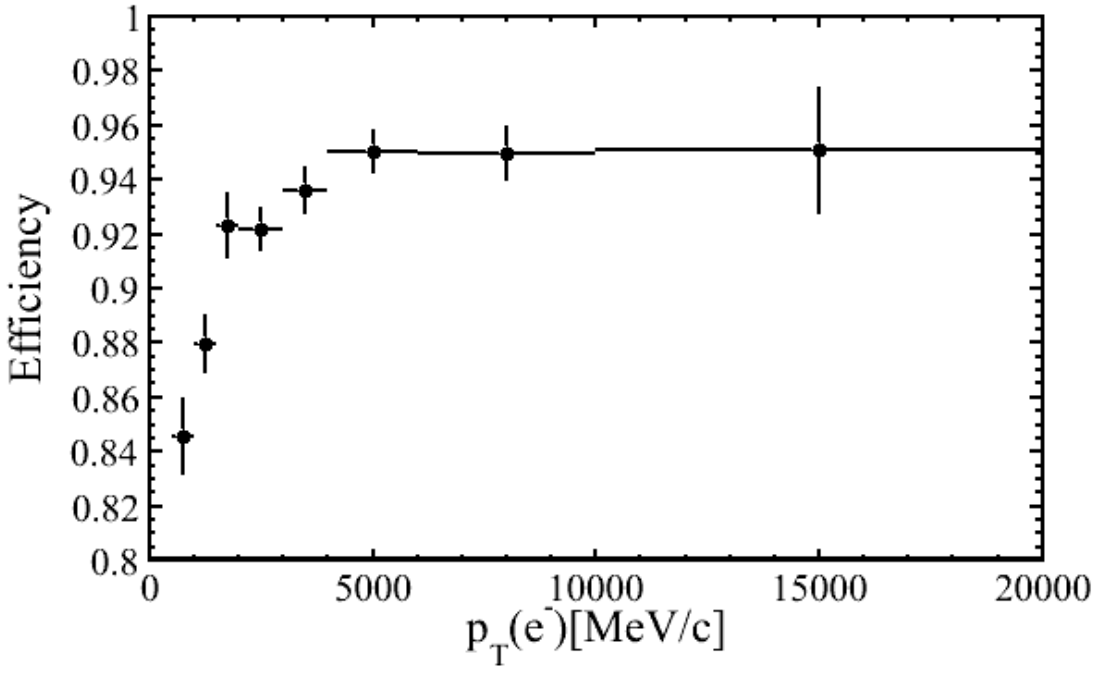

Figure 4.32: The efficiency of $\mathrm{DLL}_{e\pi}$ >1 as a function of p_{T} for the e^-.

pion, and $\mathrm{DLL}_{K\pi}$ >0 cut on the kaon can then be found on an event by event basis, and then averaged. As the performance of the RICH varies with time, 16 samples are provided from throughout the whole data taking period. The K^{*0} efficiency was determined according to each of these samples, and the weighted average of these gives the average efficiency over the whole 2011 data sample. The results are shown in Tables 4.27 and 4.28.

Due to the fact that the trigger and selection are already applied, the momenta spectra for the daughter particles are more similar for $B^0 \to K^{*0}e^+e^-$ and $B^0 \to J/\psi(e^+e^-)K^{*0}$ in this case, as shown in Figures 4.33, 4.34 and 4.35, than at generation as was shown in Fig. 4.1.

This implies that the ratio of the PID efficiencies is approximately unity for both the e^+e^-, and the K^{*0}, as indeed is measured, and can be seen in Table 4.29. These values lead to overall PID efficiency ratios of:

	$p_{\rm T}$ (MeV/c)	efficiency (%)
e^+	[500,1000]	82.82 ± 1.24
	[1000,1500]	89.79 ± 0.91
	[1500,2000]	90.92 ± 1.10
	[2000,3000]	92.47 ± 0.77
	[3000,4000]	93.45 ± 0.86
	[4000,6000]	92.24 ± 0.87
	[6000,10000]	93.72 ± 1.27
	[10000,20000]	92.76 ± 3.81
e^-	[500,1000]	84.54 ± 1.43
	[1000,1500]	87.98 ± 1.01
	[1500,2000]	92.31 ± 1.22
	[2000,3000]	92.16 ± 0.83
	[3000,4000]	93.59 ± 0.90
	[4000,6000]	95.05 ± 0.83
	[6000,10000]	94.98 ± 1.03
	[10000,20000]	95.08 ± 2.36
Average	[500,1000]	83.68 ± 0.95
	[1000,1500]	88.89 ± 0.68
	[1500,2000]	91.62 ± 0.82
	[2000,3000]	92.32 ± 0.57
	[3000,4000]	93.52 ± 0.62
	[4000,6000]	93.65 ± 0.60
	[6000,10000]	94.35 ± 0.82
	[10000,20000]	93.92 ± 2.24

Table 4.24: The efficiencies for $\mathrm{DLL}_{e\pi}$ >1 in bins of $p_{\rm T}$. The errors correspond directly to the statistical errors as determined by the fit.

Trigger category	$\epsilon_{\mathrm{PID}_{e^+e^-}}$ (%)
L0ElectronTOS	84.3 ± 1.0
L0HadronTOS	83.3 ± 1.0
L0TIS	82.6 ± 1.0

Table 4.25: Summary of the $\mathrm{DLL}_{e\pi}$ efficiencies for $B^0 \to J/\psi\, K^{*0}$.

$$\frac{\epsilon^{B^0\to J/\psi\, K^{*0}}_{\rm PID\ \ L0ElectronTOS}}{\epsilon^{B^0\to K^{*0}e^+e^-}_{\rm PID\ \ L0ElectronTOS}} = 1.02 \pm 0.02 \tag{4.24}$$

Table 4.26: Summary of the $\mathrm{DLL}_{e\pi}$ efficiencies for $B^0 \to K^{*0}e^+e^-$.

Trigger category	$\epsilon_{\mathrm{PID}_{e^+e^-}}$ (%)
L0ElectronTOS	83.6 ± 1.0
L0HadronTOS	78.6 ± 1.0
L0TIS	79.7 ± 1.0

Table 4.27: Summary of the PID efficiencies for the K^{*0} from $B^0 \to J/\psi K^{*0}$.

Trigger category	$\epsilon_{\mathrm{PID}_{K^{*0}}}$
L0ElectronTOS	90.46 ± 0.03
L0HadronTOS	87.97 ± 0.02
L0TIS	90.58 ± 0.03

$$\frac{\epsilon^{B^0\to J/\psi K^{*0}}_{\mathrm{PID\ \ L0HadronTOS}}}{\epsilon^{B^0\to K^{*0}e^+e^-}_{\mathrm{PID\ \ L0HadronTOS}}} = 1.09 \pm 0.02 \tag{4.25}$$

and

$$\frac{\epsilon^{B^0\to J/\psi K^{*0}}_{\mathrm{PID\ \ L0TIS}}}{\epsilon^{B^0\to K^{*0}e^+e^-}_{\mathrm{PID\ \ L0TIS}}} = 1.05 \pm 0.02 \tag{4.26}$$

4.10.2.5 BDT efficiency

The efficiency of the BDT cuts for each trigger category are calculated using the $B^0 \to J/\psi K^{*0}$ and $B^0 \to K^{*0}e^+e^-$ MC. The individual efficiencies are given in Tables 4.30 and 4.31, giving rise to the ratios:

$$\frac{\epsilon^{B^0\to J/\psi K^{*0}}_{\mathrm{BDT\ \ L0ElectronTOS}}}{\epsilon^{B^0\to K^{*0}e^+e^-}_{\mathrm{BDT\ \ L0ElectronTOS}}} = 0.91 \pm 0.02 \tag{4.27}$$

$$\frac{\epsilon^{B^0\to J/\psi K^{*0}}_{\mathrm{BDT\ \ L0HadronTOS}}}{\epsilon^{B^0\to K^{*0}e^+e^-}_{\mathrm{BDT\ \ L0HadronTOS}}} = 0.91 \pm 0.03 \tag{4.28}$$

$$\frac{\epsilon^{B^0\to J/\psi K^{*0}}_{\mathrm{BDT\ \ L0TIS}}}{\epsilon^{B^0\to K^{*0}e^+e^-}_{\mathrm{BDT\ \ L0TIS}}} = 0.91 \pm 0.03 \tag{4.29}$$

Table 4.28: Summary of the PID efficiencies for the K^{*0} from $B^0 \to K^{*0}e^+e^-$.

Trigger category	$\epsilon_{\mathrm{PID}_{K^{*0}}}$
L0ElectronTOS	89.80 ± 0.03
L0HadronTOS	85.75 ± 0.02
L0TIS	89.35 ± 0.03

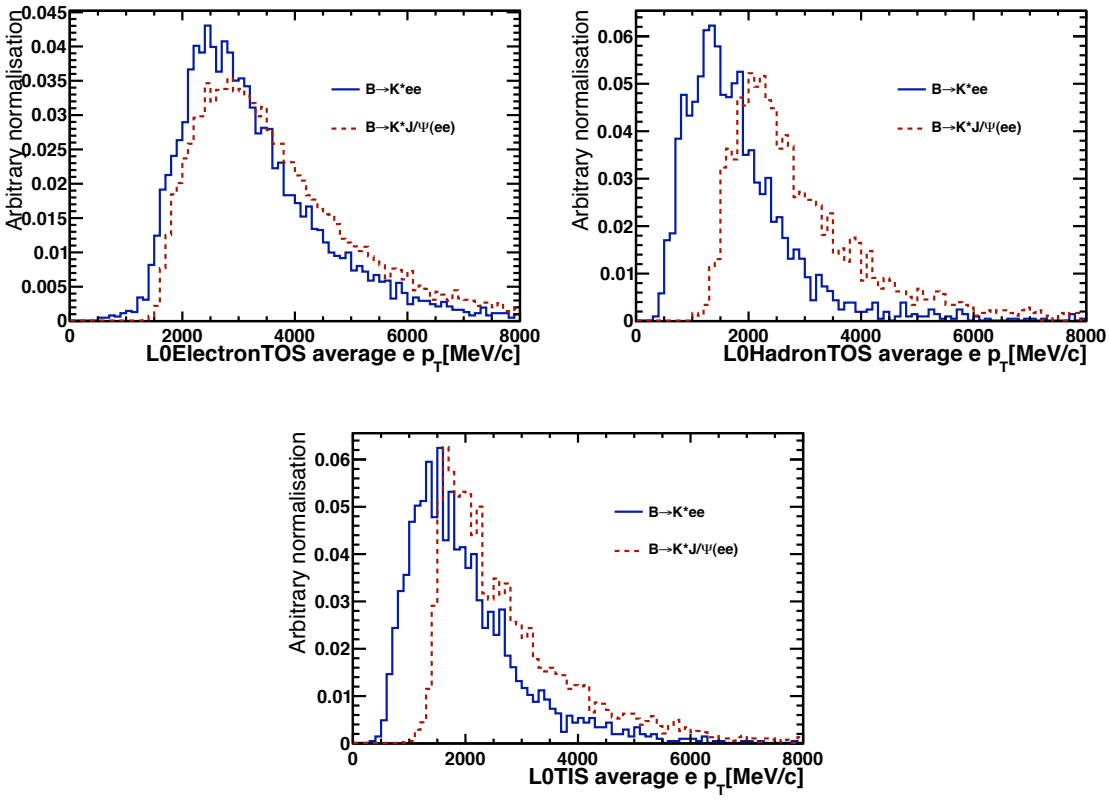

Figure 4.33: The average p_{T} of the electrons after the trigger and all cuts, except PID, for $B^0 \to K^{*0}e^+e^-$ MC, (blue solid line,) and $B^0 \to J/\psi(e^+e^-)K^{*0}$ MC, (red dotted line.)

4.10.2.6 Dilepton mass cut efficiency

As the branching fraction being measured in this analysis is of $B^0 \to K^{*0}e^+e^-$ specifically in the dilepton mass region of 30 MeV/c^2 to 1 GeV/c^2, it is important to correctly determine the selection efficiency of the mass cut. This requires knowledge of the fraction of signal with a dilepton mass truly falling in this range, but being

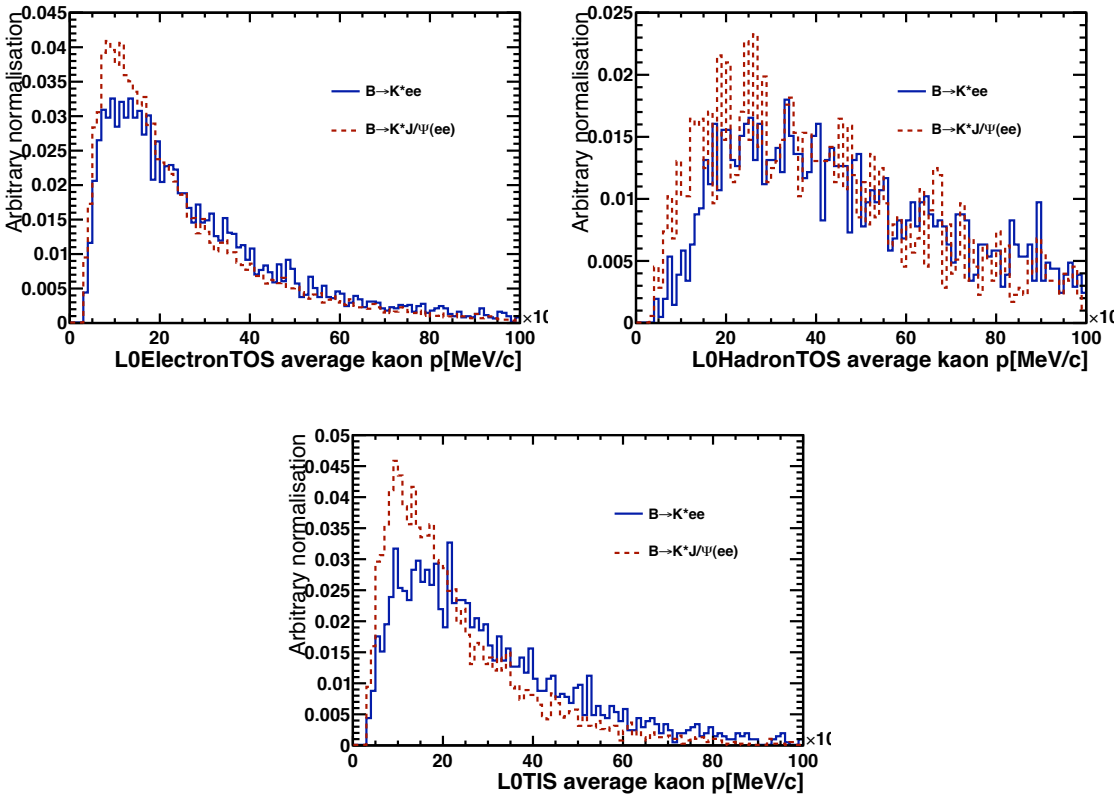

Figure 4.34: The average p of the kaon after the trigger and all cuts except PID, for $B^0 \to K^{*0}e^+e^-$ MC, (blue solid line,) and $B^0 \to J/\psi\,(e^+e^-)K^{*0}$ MC, (red dotted line.)

Table 4.29: Summary of the ratio of PID efficiencies for e^+e^- and K^{*0}.

Trigger category	$\frac{\epsilon^{B^0\to J/\psi\,K^{*0}}_{\mathrm{PID}_{e^+e^-}}}{\epsilon^{B^0\to K^{*0}e^+e^-}_{\mathrm{PID}_{e^+e^-}}}$	$\frac{\epsilon^{B^0\to J/\psi\,K^{*0}}_{\mathrm{PID}_{K^{*0}}}}{\epsilon^{B^0\to K^{*0}e^+e^-}_{\mathrm{PID}_{K^{*0}}}}$	$\frac{\epsilon^{B^0\to J/\psi\,K^{*0}}_{\mathrm{PID}_{\mathrm{Total}}}}{\epsilon^{B^0\to K^{*0}e^+e^-}_{\mathrm{PID}_{\mathrm{Total}}}}$
L0ElectronTOS	1.009 ± 0.016	1.0073 ± 0.0004	1.02 ± 0.02
L0HadronTOS	1.060 ± 0.018	1.0260 ± 0.0004	1.09 ± 0.02
L0TIS	1.036 ± 0.018	1.0138 ± 0.0004	1.05 ± 0.02

reconstructed as outside it, and also the events with a mass greater than 1 GeV or less than 30 MeV/c^2, which are reconstructed within the region of interest. In both cases, this occurs primarily due to bremsstrahlung radiation.

As the mass cuts are applied at the stripping level, and thus are present on the

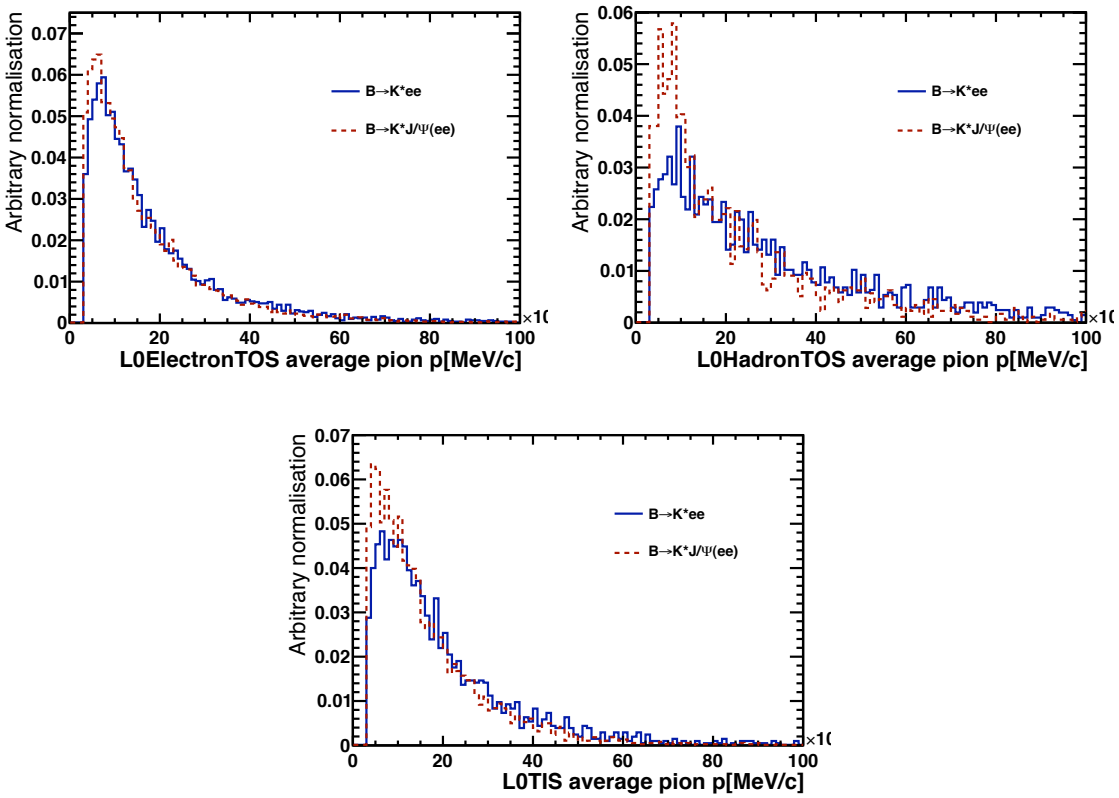

Figure 4.35: The average p of the pion after the trigger and all cuts except PID, for $B^0 \to K^{*0} e^+ e^-$ MC, (blue solid line,) and $B^0 \to J/\psi\,(e^+e^-) K^{*0}$ MC, (red dotted line.)

Table 4.30: Efficiencies of the BDT cut for $B^0 \to J/\psi\, K^{*0}$.

Trigger category	$\epsilon_{\rm L0}$ (%)
L0ElectronTOS	82 ± 1
L0HadronTOS	84 ± 2
L0TIS	73 ± 1

standard MC sample, another sample was produced with no cut on the dilepton mass range. Using this MC sample, the number of events selected with a reconstructed mass between 30 MeV/c^2 and 1 GeV/c^2 will indeed include those whose real mass is greater than 1 GeV or less than 30 MeV/c^2, as in the real data. The distribution of the generated dilepton mass after all of the cuts, including the final selection cut

Table 4.31: Efficiencies of the BDT cut for $B^0 \to K^{*0} e^+ e^-$.

Trigger category	ϵ_{L0} (%)
L0ElectronTOS	90 ± 1
L0HadronTOS	93 ± 2
L0TIS	80 ± 2

of the reconstructed dilepton, can be seen in Fig. 4.36. It has a similar shape for each of the three trigger categories, and demonstrates the fraction above 1 GeV which are reconstructed within the signal region. The first bin in this histogram is 0-30 MeV/c^2, thus it can also be seen that there is a small fraction of these events reconstructed with a mass greater than 30 MeV/c^2. This is due to multiple scattering increasing the small opening angle at this dilepton mass range. Although there is a

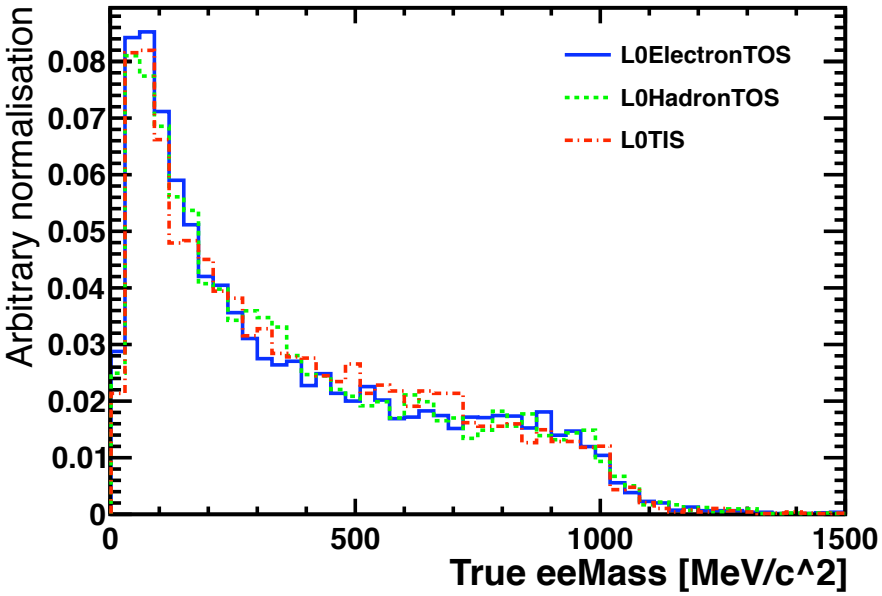

Figure 4.36: Generated dilepton mass after all final cuts for each trigger category.

huge increase in the number of events with dilepton mass <30 MeV/c^2 at generation level, these are not efficiently reconstructed, explaining why only a small fraction of events below this value are reconstructed above was a mass above it. Fig. 4.37 compares the generated dilepton mass with those where the two electrons tracks are reconstructible, meaning they are in the acceptance of the detectors needed

to be reconstructed as a long track and those where the two electron tracks are successfully reconstructed. Fig. 4.38 compared the generated and reconstructed

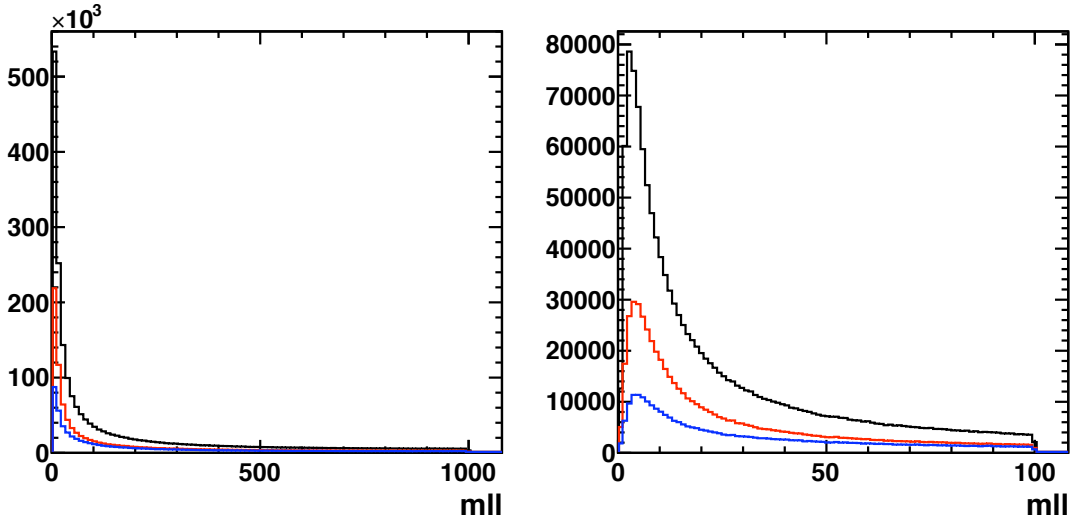

(a) (b)

Figure 4.37: Full dilepton mass range for the $B^0 \to K^{*0}e^+e^-$ MC sample at the generation level (black), for reconstructible dielectrons (red) and reconstructed dielectrons (blue). The plot on the right is a zoom of that on the left.

masses for events passing the L0ElectronTOS criteria for this $B^0 \to K^{*0}e^+e^-$ MC sample. It should be noted that the veto on $B^0 \to K^{*0}\gamma$ events also removes a significant fraction of the badly reconstructed events with true dilepton mass <30 MeV/c^2, as can be seen in Fig. 4.39, showing the same plot with these cuts removed. A table showing the relative proportion of the $B^0 \to K^{*0}e^+e^-$ MC events falling within the bins of true dilepton mass of 0-30 MeV/c^2, 30-1000 MeV/c^2 and >1000 MeV/c^2, along with how these events migrate into the same bins of reconstructed mass is shown in Fig. 4.40. The same table with the veto on $B^0 \to K^{*0}\gamma$ events removed is also given.

The ratio of the events measured with a reconstructed mass in the region of interest, with respect to those with a true mass in the correct range includes all the migration effects, and gives the correct mass efficiency to apply to the branching ratio measurement. The efficiencies are given in Tables 4.32 and 4.33. As expected, in the case of $B^0 \to J/\psi K^{*0}$, this efficiency is less than 1, due to the loss of events with a large amount of bremsstrahlung radiation. For $B^0 \to K^{*0}e^+e^-$, this number is greater than 1, as more strictly, it describes a migration rather than an efficiency,

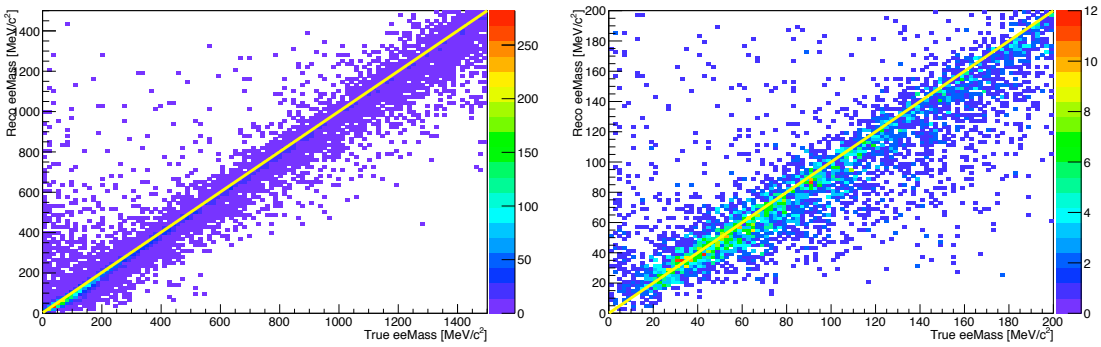

(a) (b)

Figure 4.38: Generated dilepton mass vs the reconstructed dilepton mass for the L0ElectronTOS $B^0 \to K^{*0}e^+e^-$ MC sample after all cuts other than the one on the reconstructed dilepton mass, (left) and a zoom in on the lower mass region (right). The yellow line shows where the reconstructed mass is equal to the generated mass.

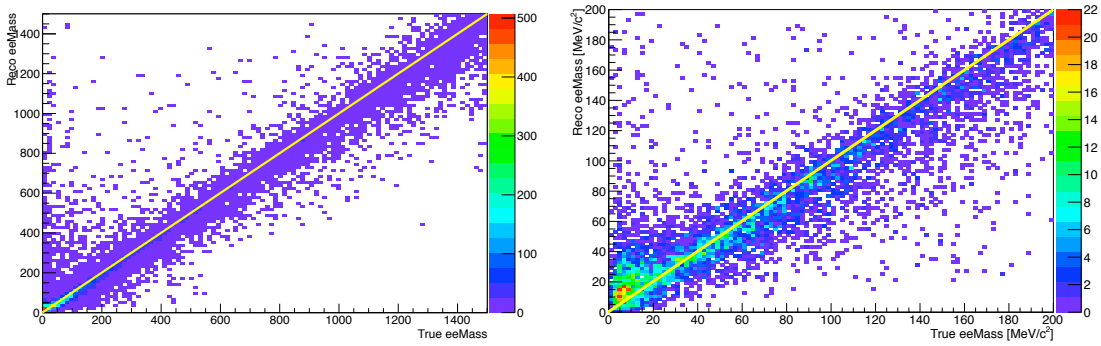

(a) (b)

Figure 4.39: Generated dilepton mass vs the reconstructed dilepton mass for the L0ElectronTOS $B^0 \to K^{*0}e^+e^-$ MC sample without the $B^0 \to K^{*0}\gamma$ veto, (left) and a zoom in on the lower mass region (right). The yellow line shows where the reconstructed mass is equal to the generated mass.

and more events fall inside the signal mass window from outside it, than vice versa. The ratio of mass efficiencies are thus measured to be:

$$\frac{\epsilon^{B^0\to J/\psi K^{*0}}_{\text{mass L0ElectronTOS}}}{\epsilon^{B^0\to K^{*0}e^+e^-}_{\text{mass L0ElectronTOS}}} = 0.95 \pm 0.02 \tag{4.30}$$

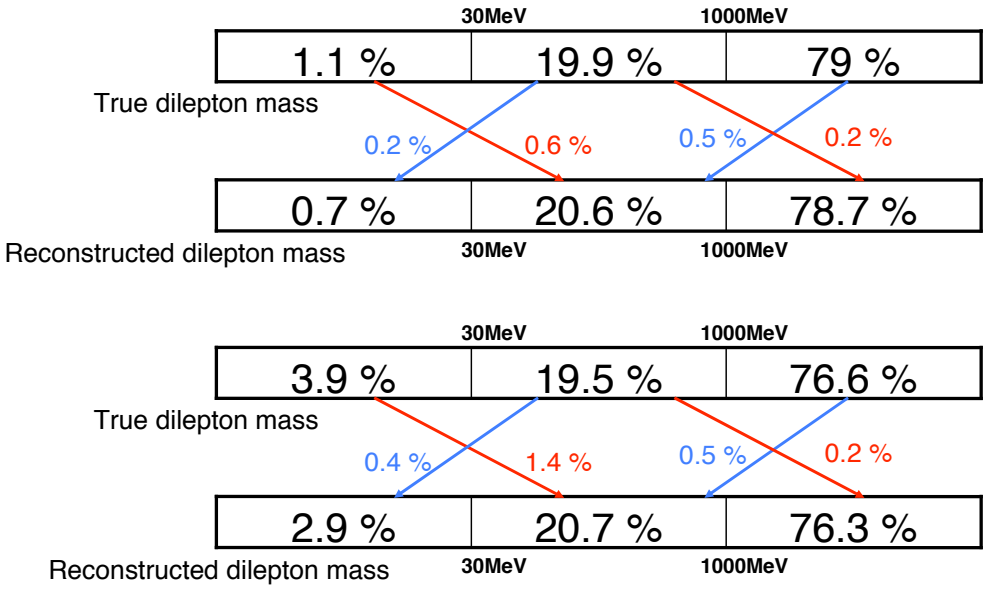

Figure 4.40: Number of events falling in different bins of the true dilepton mass, and how these events migrate to bins of reconstructed mass (above). The same table with the $B^0 \to K^{*0}\gamma$ veto removed is also given (below).

$$\frac{\epsilon^{B^0\to J/\psi\, K^{*0}}_{\text{mass L0HadronTOS}}}{\epsilon^{B^0\to K^{*0}e^+e^-}_{\text{mass L0HadronTOS}}} = 0.95 \pm 0.03 \tag{4.31}$$

$$\frac{\epsilon^{B^0\to J/\psi\, K^{*0}}_{\text{mass L0TIS}}}{\epsilon^{B^0\to K^{*0}e^+e^-}_{\text{mass L0TIS}}} = 0.97 \pm 0.03 \tag{4.32}$$

Table 4.32: Efficiencies of the dilepton mass cut for $B^0 \to J/\psi\, K^{*0}$.

Trigger category	$\epsilon_{\text{dilepton mass}}$ (%)
L0ElectronTOS	98 ± 1
L0HadronTOS	98 ± 3
L0TIS	99 ± 2

Although the overall selection and reconstruction efficiency depends on the dilepton mass, as shown in Fig. 4.41, the dilepton mass spectrum is well reproduced by the MC. Fig. 4.42 shows the MC dilepton mass distribution overlaid with the signal dilepton mass from data, with the background removed using the splot technique [74], which assumes the dilepton mass not correlated with the B mass. Thus the

Table 4.33: Efficiencies of the dilepton mass cut for $B^0 \to K^{*0} e^+ e^-$.

Trigger category	$\epsilon_{\text{dilepton mass}}$ (%)
L0ElectronTOS	103 ± 1
L0HadronTOS	103 ± 2
L0TIS	102 ± 2

average efficiency correction can be safely calculated using the MC.

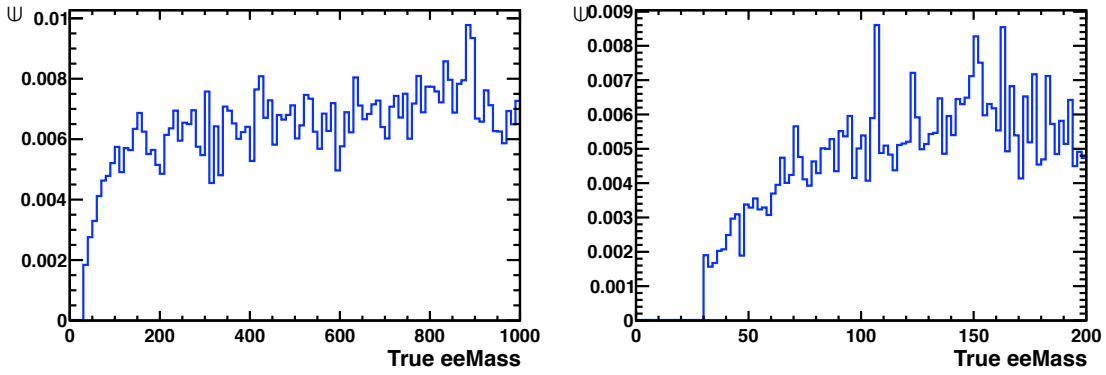

(a) (b)

Figure 4.41: The efficiency of the selection as a function of dielectron mass (left), and a zoom in on the lower mass region (right).

4.10.3 Branching fraction ratio

The various contributions to the measurement of the ratio branching fractions, as defined in equation 4.11 are summarised in Table 4.34.

Combining the yields in eqns. 4.12-4.14 with all the individual contributions to the efficiency ratio, the $B^0 \to K^{*0} e^+ e^-$ branching ratio, for each trigger category, is measured to be:

$$\mathcal{B}(B^0 \to K^{*0} e^+ e^-)^{30-1000\,\text{MeV}/c^2}_{\text{L0ElectronTOS}} = (3.17^{+0.84}_{-0.76}) \times 10^{-7} \tag{4.33}$$

$$\mathcal{B}(B^0 \to K^{*0} e^+ e^-)^{30-1000\,\text{MeV}/c^2}_{\text{L0HadronTOS}} = (3.37^{+2.83}_{-2.38}) \times 10^{-7} \tag{4.34}$$

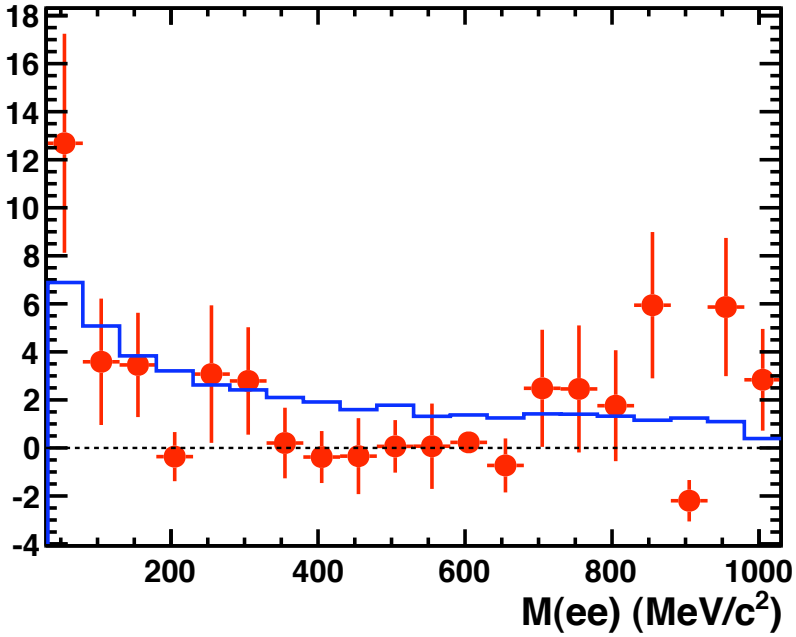

Figure 4.42: The $B^0 \to K^{*0}e^+e^-$ dielectron mass distribution after all cuts, shown for the MC and data with the background removed using sweights.

Table 4.34: Contributing factors to the measurement of the ratio of branching fractions.

	L0ElectronTOS ratio	L0HadronTOS ratio	L0TIS ratio
$\frac{\text{Nsig}_{B^0\to K^{*0}e^+e^-}}{\text{Nsig}_{B^0\to J/\psi K^{*0}}}$	$0.00277^{+0.00073}_{-0.00067}$	$0.00740^{+0.00623}_{-0.00525}$	$0.00418^{+0.00276}_{-0.00236}$
$\frac{\epsilon^{B^0\to J/\psi K^{*0}}_{\text{Acceptance}}}{\epsilon^{B^0\to K^{*0}e^+e^-}_{\text{Acceptance}}}$	0.955 ± 0.004	0.955 ± 0.004	0.955 ± 0.004
$\frac{\epsilon^{B^0\to J/\psi K^{*0}}_{\text{Reco\&Sel}}}{\epsilon^{B^0\to K^{*0}e^+e^-}_{\text{Reco\&Sel}}}$	1.22 ± 0.03	1.28 ± 0.05	1.21 ± 0.04
$\frac{\epsilon^{B^0\to J/\psi K^{*0}}_{\text{Trigger}}}{\epsilon^{B^0\to K^{*0}e^+e^-}_{\text{Trigger}}}$	1.41 ± 0.03	0.50 ± 0.05	0.89 ± 0.02
$\frac{\epsilon^{B^0\to J/\psi K^{*0}}_{\text{PID}}}{\epsilon^{B^0\to K^{*0}e^+e^-}_{\text{PID}}}$	1.02 ± 0.02	1.09 ± 0.02	1.05 ± 0.02
$\frac{\epsilon^{B^0\to J/\psi K^{*0}}_{\text{BDT}}}{\epsilon^{B^0\to K^{*0}e^+e^-}_{\text{BDT}}}$	0.91 ± 0.02	0.91 ± 0.03	0.91 ± 0.03
$\frac{\epsilon^{B^0\to J/\psi K^{*0}}_{\text{mass}}}{\epsilon^{B^0\to K^{*0}e^+e^-}_{\text{mass}}}$	0.95 ± 0.02	0.95 ± 0.02	0.97 ± 0.02

$$\mathcal{B}(B^0 \to K^{*0}e^+e^-)^{30-1000\,\text{MeV}/c^2}_{\text{L0TIS}} = (3.22^{+2.13}_{-1.82}) \times 10^{-7} \tag{4.35}$$

By assigning a statistical weight to each, the measurements for each of three

categories in this manner were combined, giving an average measurement of:

$$\mathcal{B}(B^0 \to K^{*0} e^+ e^-)^{30-1000\,\mathrm{MeV}/c^2} = (3.19^{+0.75}_{-0.68}) \times 10^{-7} \tag{4.36}$$

4.11 Systematic uncertainties

Although the selection was designed with the intention of reducing systematic effects through the measurement of a ratio of branching fractions, several sources of uncertainties are studied.

4.11.1 Ratio of selection, BDT cut and mass cut

The ratio of BDT, Reconstruction & Selection, and mass efficiencies are obtained from the same MC samples, and the uncertainty arising from the available statistics is propagated to a systematic error on the $B^0 \to K^{*0} e^+ e^-$ branching fraction. The combined value of their ratios, and their uncertainties are given in Table 4.35.

Table 4.35: Combined selection, BDT and mass efficiency ratio.

Trigger category	ϵ
L0ElectronTOS	1.05 ± 0.01
L0HadronTOS	1.10 ± 0.03
L0TIS	1.06 ± 0.03

4.11.2 Ratio of trigger efficiencies

As the trigger efficiencies are calculated using data samples covering the whole year of data taking, and thus include the change in performance over time, only the error coming from the available statistics in each bin used to create the efficiency tables, shown as the error on the ratio in Equations 4.21-4.23, are taken as systematic errors.

4.11.3 Ratio of PID efficiencies

The systematic error introduced by performing the PID as described in Section 4.10.2.4, (*e.g.* through the loss of information due to coarse binning) can be investigated using MC calibration samples. As these MC calibration samples should have the same dependency on p and η as the MC signal sample used to perform the weighting, repeating the procedure described in Sec. 4.10.2.4 to determine the ratio of PID efficiencies for the K^{*0} using the MC calibration samples instead of data, and comparing to the ratio as determined directly from the signal MC samples, a systematic error can be assigned. The ratio of efficiencies according to both the MC calibration samples, and directly from the signal MC are given in Table 4.36, and give rise to a systematic error of 1.0% for L0HadronTOS and 1.0% for L0TIS, with no significant change in the L0ElectronTOS category. Conservatively, a 1% systematic uncertainty is assigned for the three categories.

Table 4.36: Ratio of efficiencies of PID cuts on K^{*0}.

Trigger category	$\frac{\epsilon^{B^0\to J/\psi\,K^{*0}}_{\text{PID}_{K^{*0}}}}{\epsilon^{B^0\to K^{*0}e^+e^-}_{\text{PID}_{K^{*0}}}}$ MC calibration	$\frac{\epsilon^{B^0\to J/\psi\,K^{*0}}_{\text{PID}_{K^{*0}}}}{\epsilon^{B^0\to K^{*0}e^+e^-}_{\text{PID}_{K^{*0}}}}$ MC signal
L0ElectronTOS	1.006	1.006
L0HadronTOS	1.042	1.031
L0TIS	1.011	1.002

No MC calibration samples are available to perform the same test for the ratio of efficiencies of the $\text{DLL}_{e\pi}$ cut. The systematic is taken by averaging the PID across all bins, thus removing the dependence on p_{T}. The ratio of the efficiency of the $\text{DLL}_{e\pi}$ cut on $B^0 \to K^{*0}e^+e^-$ and $B^0 \to J/\psi\,K^{*0}$ is therefore one, giving rise to a systematic of 1% for L0ElectronTOS, 6% for L0HadronTOS and 3.6% for L0TIS. As for the systematic due to the trigger, the error coming from the available statistics in each bin used to create the efficiency tables, shown as the error on the ratios in Table 4.29, are also included in the final systematic error calculation.

4.11.4 Uncertainty on the fit procedure

In order to evaluate the systematics on the yields due to the fit description, toy MC samples are generated with variations from the fit model as described in 4.8.1, and then fit with the default model. For each test, 10000 toy samples have been generated using the parameters obtained on data for the yields and the slope of the exponential shape of the combinatorial background.

The pull distribution, defined as the distribution of the quantity $P_x = \frac{x_{Fit} - x_{Gen}}{\sigma_x}$ for a given parameter x, was plotted, and the bias shown by the pull distribution for the signal yield is used to calculate the corresponding systematics uncertainty.

The systematic uncertainty related to the signal shape has been evaluated by modifying the B mass and the μ_B scale factor by one standard deviation as obtained from the fit to the $B^0 \to J/\psi K^{*0}$ data. The systematic uncertainty related to the partially reconstructed background has been evaluated by varying its fraction by ± 50%. The biases are shown in Table 4.11.4.

Trigger category	sμ_B cale factor	B mass	nPartReco
L0ElectronTOS	0.04	0.01	0.11
L0HadronTOS	0.09	0.03	0.03
L0TIS	0.06	0.02	0.04

Table 4.37: Bias on the number of signal found from toy MC due to the fitting parameters. The values are expressed as a function of the statistical uncertainty.

4.11.5 Knowledge of the $B^0 \to K^{*0}\gamma$ contamination

As explained in Section 4.10.1, the fraction of contamination of the $B^0 \to K^{*0}e^+e^-$ signal yields from $B^0 \to K^{*0}\gamma$ is taken from MC and the reliability of this was checked by confirming the agreement of the fraction lost by the veto on data compared to MC. Therefore, a systematic error on this fraction, taken as 10% in all categories, is assigned by taking the statistical error on the number of events removed by the veto on the data. Due to the limited statistics available, this was done by summing over all three trigger categories. With the veto, 43.3 ± 10 events are observed, and 57 ± 13 events without. The difference is therefore 13 with a 40% error. The fraction of contamination is therefore (10 ± 4)%.

4.11.6 Summary of systematic errors

Table 4.38 shows a summary of all systematic errors.

source of error	L0 Category	systematic uncertainty on $B^0 \to K^{*0}e^+e^-$ branching ratio. ($\times 10^{-8}$)
generated MC stats	L0ElectronTOS	0.13
	L0HadronTOS	0.14
	L0TIS	0.14
MC stats after selection	L0ElectronTOS	0.30
	L0HadronTOS	0.92
	L0TIS	0.91
L0 trigger ratio stats in eff tables	L0ElectronTOS	0.45
	L0HadronTOS	0.67
	L0TIS	0.36
PID(K*) eff ratio procedure & stats in eff tables	L0ElectronTOS	0.32
	L0HadronTOS	0.33
	L0TIS	0.31
PID (e^+e^-) eff ratio procedure & stats in eff tables	L0ElectronTOS	0.59
	L0HadronTOS	1.99
	L0TIS	1.25
fit procedure	L0ElectronTOS	0.98
	L0HadronTOS	2.80
	L0TIS	1.60
knowledge of $B^0 \to K^{*0}\gamma$ contamination	L0ElectronTOS	1.41
	L0HadronTOS	1.50
	L0TIS	1.43
sum (quadrature)	L0ElectronTOS	1.9
	L0HadronTOS	3.9
	L0TIS	2.69
$B^0 \to J/\psi(e^+e^-)K^{*0}$ BR	L0ElectronTOS	1.46
	L0HadronTOS	1.55
	L0TIS	1.48

Table 4.38: Summary of the systematic uncertainties.

Combining the systematics, the branching fractions are found to be:

$$\mathcal{B}(B^0 \to K^{*0}e^+e^-)^{30-1000\,\mathrm{MeV}/c^2} = (3.17^{+0.84}_{-0.76} \pm 0.19 \pm 0.15) \times 10^{-7} \qquad (4.37)$$

$$\mathcal{B}(B^0 \to K^{*0} e^+ e^-)^{30-1000\,\mathrm{MeV}/c^2} = (3.37^{+2.83}_{-2.38} \pm 0.39 \pm 0.15) \times 10^{-7} \quad (4.38)$$

$$\mathcal{B}(B^0 \to K^{*0} e^+ e^-)^{30-1000\,\mathrm{MeV}/c^2} = (3.22^{+2.13}_{-1.82} \pm 0.27 \pm 0.15) \times 10^{-7} \quad (4.39)$$

where the first error is statistical, the second is due to systematics, and the third comes from the error on the $B^0 \to J/\psi\, K^{*0}$ branching fraction [25]. Giving each measurement a statistical weight, the branching ratios are combined, taking into account the fact the correlation of some of the systematic errors amongst the three trigger categories. (The systematic uncertainties arising from the acceptance and PID efficiency ratios, the fitting procedure, and the fraction of $B^0 \to K^{*0}\gamma$ contamination are assumed to be fully correlated.) The combined branching ratio is found to be:

$$\mathcal{B}(B^0 \to K^{*0} e^+ e^-)^{30-1000\,\mathrm{MeV}/c^2} = (3.19^{+0.75}_{-0.68} \pm 0.21 \pm 0.15) \times 10^{-7} \quad (4.40)$$

4.12 Final result

In the 1 fb^{-1} of data collected at the LHCb experiment in 2011, a sample of $\approx 40 \pm 9$ $B^0 \to K^{*0} e^+ e^-$, in the dilepton mass range $[30 - 1000]\,\mathrm{MeV}/c^2$ has been collected. This is the combination of three measurements performed in different trigger categories, with the largest sample, (those where the L0Trigger was fired by a signal electron,) observed with a $\frac{S}{\sqrt{(S+B)}} = 4.2$. The ratio of its branching fraction with respect to that of $B^0 \to J/\psi\, K^{*0}$ was measured separately in each category. Combining these and using $\mathcal{B}(B^0 \to J/\psi\, K^{*0})=(1.34 \pm 0.06)\times 10^{-3}$ and $\mathcal{B}(J/\psi \to e^+e^-)=(5.94 \pm 0.06)\%$, the $B^0 \to K^{*0} e^+ e^-$ $^{30-1000\,\mathrm{MeV}/c^2}$ branching ratio is measured to be:

$$\mathcal{B}(B^0 \to K^{*0} e^+ e^-)^{30-1000\,\mathrm{MeV}/c^2} = (3.19^{+0.75}_{-0.68} \pm 0.21 \pm 0.15) \times 10^{-7} \quad (4.41)$$

Chapter 5

Prospects and conclusions

Contents

5.1 Prospects with 3 fb^{-1}

With the data analysed here, corresponding to the $1\,\text{fb}^{-1}$ collected during in 2011, there are not enough statistics to perform the angular analysis. However, with the new running conditions during 2012, and the extended timetable to collect more proton-proton collisions, it is expected at the end of 2012, combining both datasets will provide a total integrated luminosity of around $3\,\text{fb}^{-1}$. Scaling the total yields measured in the analysis presented in this thesis, a sample of $\mathcal{O}\,(120)$ $B^0 \to K^{*0}e^+e^-$ events will be available with the whole dataset, thus allowing for the angular analysis. Using the toy MC samples, the sensitivity to $A_T^{(2)}$ and $A_T^{(Im)}$ with 120 events can be studied.

As explained in 2.4.3, when performing the fit at LHCb, the angular differential decay rate as measured at the detector will be a product of the rate according to the physics, and the detector 3D angular acceptance, $\varepsilon\,(q^2 \cos\theta_l^*, \cos\theta_K, \phi^*)$.

The LHCb acceptance functions can be obtained from the phase space MC, after all the selection cuts. The $\cos\theta_l$ acceptance curve has been fit with a $p_0(1+p_1\cos{\theta_l}^2+ p_2\cos{\theta_l}^4)$ parameterisation, and $\cos\theta_K$ by $p_0 + p_1\cos\theta_K + p_2 * \cos{\theta_K}^2 + p_3\cos{\theta_K}^3$. As a test, the ϕ^* acceptance was fit with $p_0(1 + p_1\cos(2\phi^*))$, but as p_1 was found to

be, -0.009 ± 0.015, *i.e.* compatible with zero, the efficiency was taken to be flat in the rest of the study. These efficiency curves, parameterised in this manner can be seen in Fig. 5.1. The $\cos\theta_l$ distribution is fit between -0.8 and 0.8 to ease the fitting

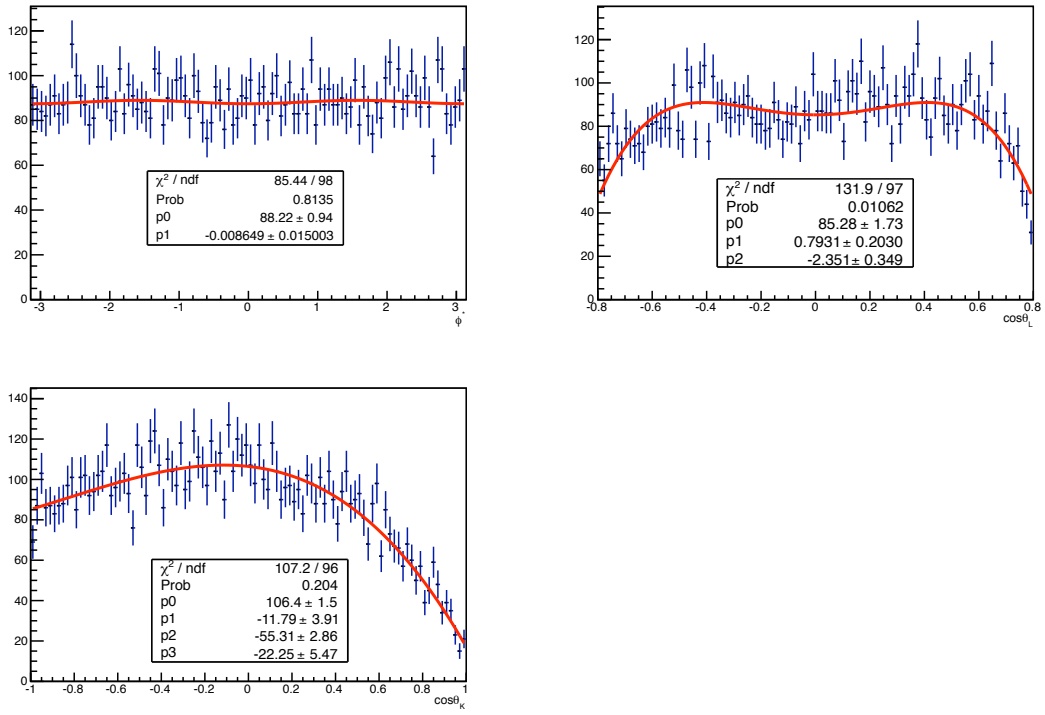

Figure 5.1: The ϕ^*, $\cos\theta_l$ and $\cos\theta_K$ acceptance curves obtained from the phase space LHCb MC, and parameterised as explained in the text. The ϕ^* distribution is consistent with being constant.

due to lack of events outside this region. This does not affect much the sensitivity to $A_T^{(2)}$, as can be inferred from Eqs. 2.21 and 2.13.

The full LHCb MC was then split into 120 toy samples, each containing 120 events. Each toy is then fit, using the knowledge of the angular acceptance obtained from the phase space MC. An example of the fit for one toy can be seen in Fig. 5.2. The distributions of the measured parameters and their uncertainties for all the toy studies are shown in Fig. 5.3 and the pull distributions in Fig. 5.4. As can be seen, the expected sensitivity on $A_T^{(2)}$, in the case where there is no background, is $\sigma(A_T^{(2)}) \approx 0.2$.

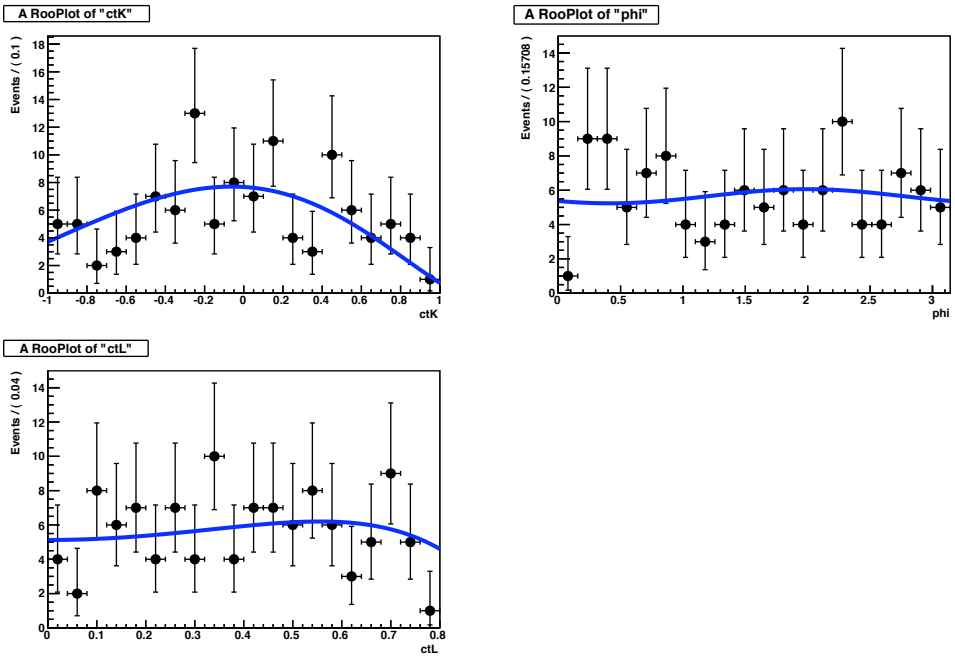

Figure 5.2: An example of the fit in one toy study containing 120 events.

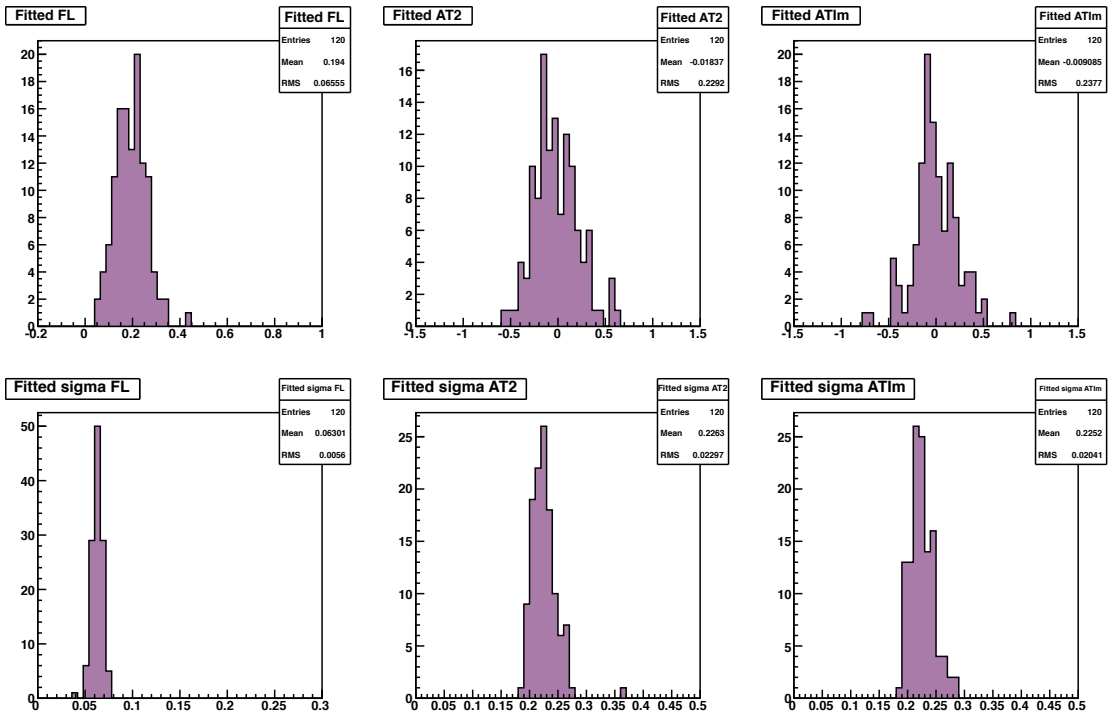

Figure 5.3: Distributions of the measured F_L, $A_T^{(2)}$, and $A_T^{(Im)}$ and their uncertainties, for toy MC samples containing 120 events distributed according to the LHCb acceptance obtained on the full MC after all cuts.

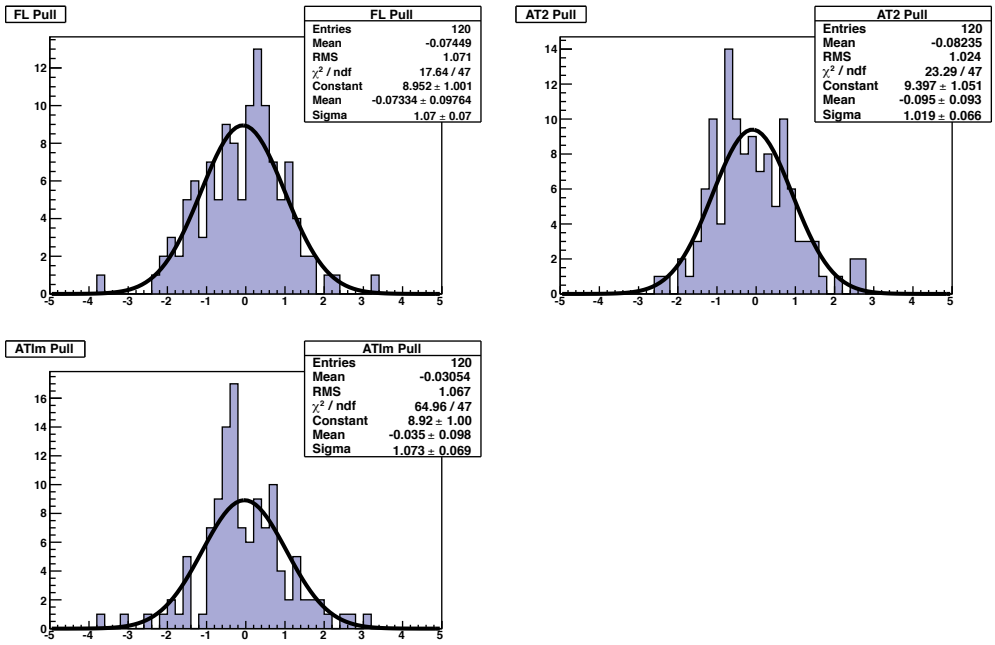

Figure 5.4: The pull distributions of the fitted F_L, $A_T^{(2)}$, and $A_T^{(Im)}$ parameters, for 120 toy MC samples containing 120 events.

5.2 Conclusions

The $b \to s\gamma$ transition is a flavour changing neutral current, and thus is useful for probing the effects of new physics by measuring details of the decay process and searching for deviations from the SM predictions. One such measurement that can be performed is of the photon polarisation, predicted to be predominantly left-handed, but can have a right handed component in certain extensions to the SM, such as the Left Right Symmetric Model. Access to the polarisation information can be gained experimentally via an angular analysis of $B^0 \to K^{*0}e^+e^-$ at low dilepton mass.

This thesis presents the first step towards the use of $B^0 \to K^{*0}e^+e^-$ in measuring the photon polarisation, by describing the measurement of the branching ratio in the dilepton mass range of interest.

The analysis is based on the data collected at the LHCb experiment during 2011. As the events can be triggered either by a signal electron, a signal hadron, or by one of the other decay products produced in the event, the samples were split into three, mutually exclusive, trigger categories. This was due to the fact that the signal shape, and the type of background varied depending on the signal category. Summing over the three categories yielded a signal sample of $\approx 40 \pm 9$ events, in the dilepton mass range $[30 - 1000]\,\mathrm{MeV}/c^2$. The branching ratio was measured for each category separately, the combination of which gives the final result:

$$\mathcal{B}(B^0 \to K^{*0}e^+e^-)^{30-1000\,\mathrm{MeV}/c^2} = (3.19^{+0.75}_{-0.68} \pm 0.21 \pm 0.15) \times 10^{-7}$$

where the first error is statistical, the second is the systematic error from LHCb, and the third is the error from the branching ratio of $B^0 \to J/\psi\,(e^+e^-)K^{*0}$. This is in good agreement with the predicted branching ratio of 2.9×10^{-7}. The analysis demonstrates, that despite the challenges of working with low p_{T} electrons in a hadronic environment, it is expected that with more data, a clean sample of $B^0 \to K^{*0}e^+e^-$ can be collected in order to perform the angular analysis. The total number of events in the 2011 data is already the largest sample available from one experiment at low q^2.

Including the data collected at 2012, increases the integrated luminosity by a factor of three. With three times the number of signal events as collected in 2011, the expected precision on $A_T^{(2)}$, in the case where there is no background, is $\sigma(A_T^{(2)}) \approx$

0.2. This corresponds to a sensitivity to the fraction of right handed polarisation of approximately 0.1.

Appendix A

Software versions used to generate the MC11 datasets.

The MC samples are generated with MC11 conditions [84], based on version 41r1 of the Gauss [82] application. The proton collisions are simulated using Pythia 6 [85] with LHCb specific conditions [86]. The decays of the produced particles are descibed by EvtGen [87] with the final state radiation handled by Photos [88]. The propagation of the particles in the detector is simulated by Geant4 [89]. Version v23r1 of the Boole application [90] is used, which simulates the digitization of the hit deposits in the detector. Moore v12r8p1 [91] is used to run the HLT on the output from Boole (and is also used to run the HLT on the real data). Finally, v41r1p1 of Brunel is used [92] to perform the reconstruction.

Appendix B

BDT Variable Distributions

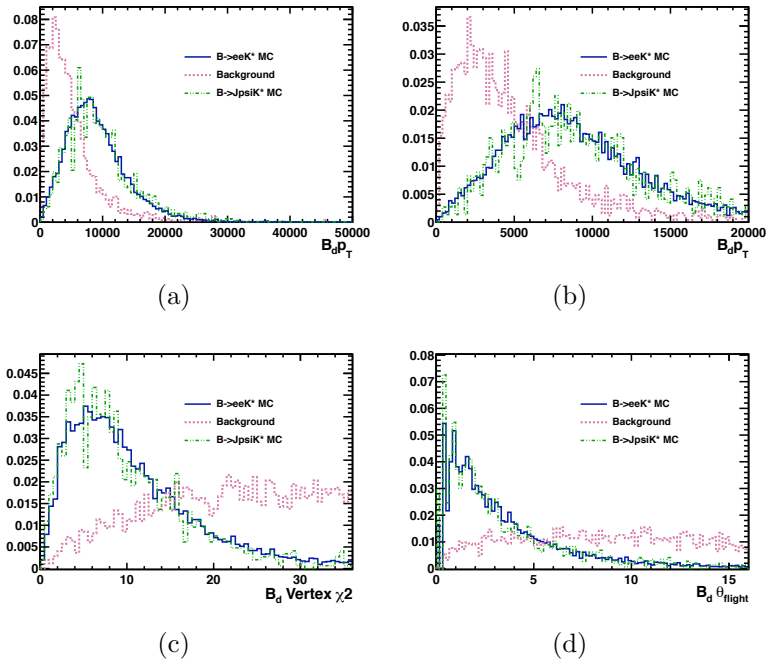

(a) (b)

(c) (d)

Figure B.1: The distributions of the variables used to train the BDT.

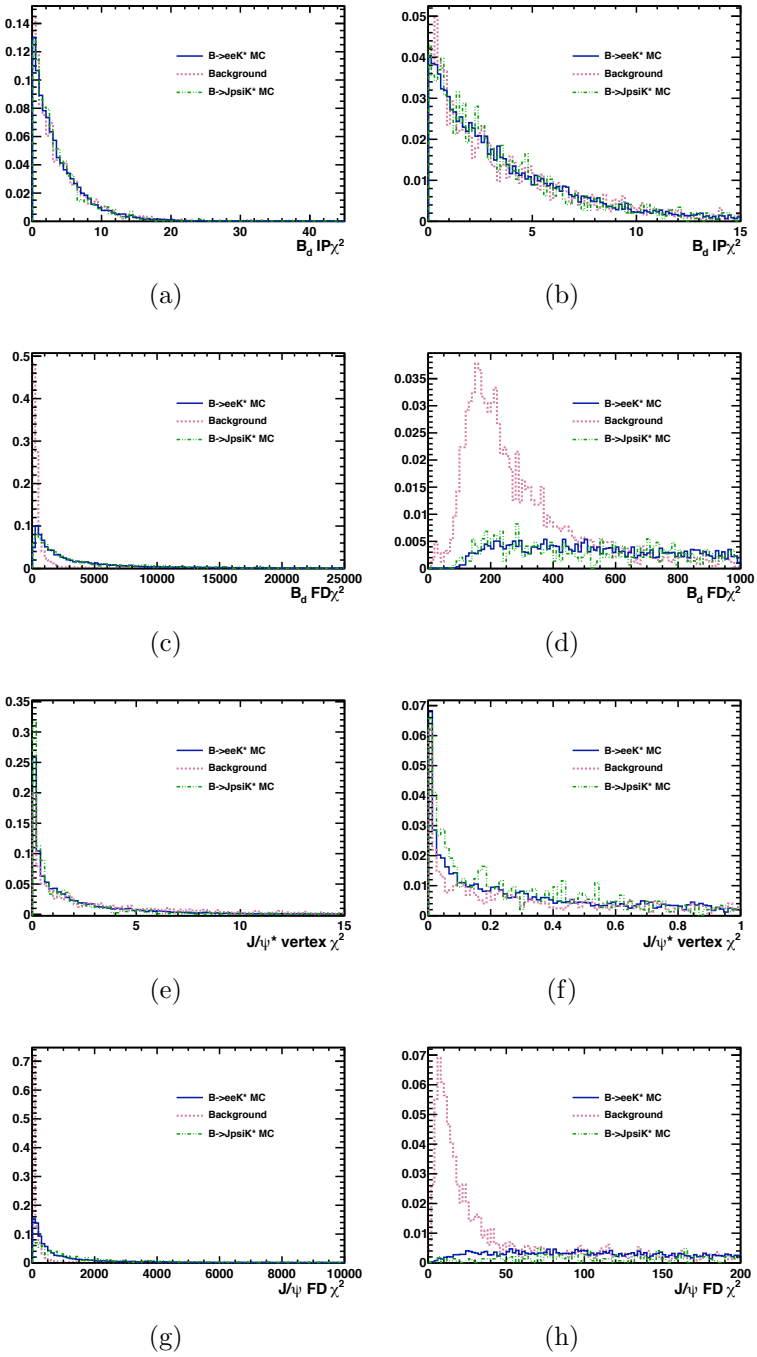

Figure B.2: The distributions of the variables used to train the BDT (cont).

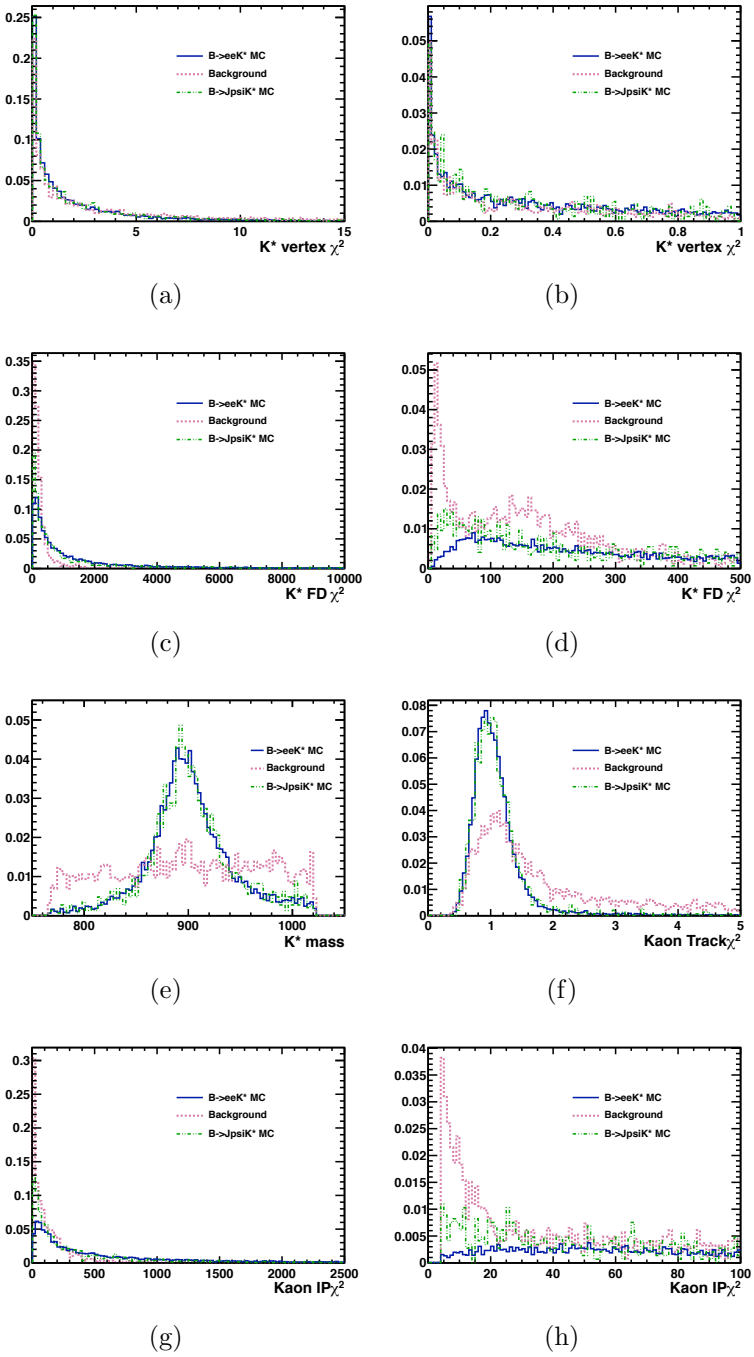

Figure B.3: The distributions of the variables used to train the BDT (cont).

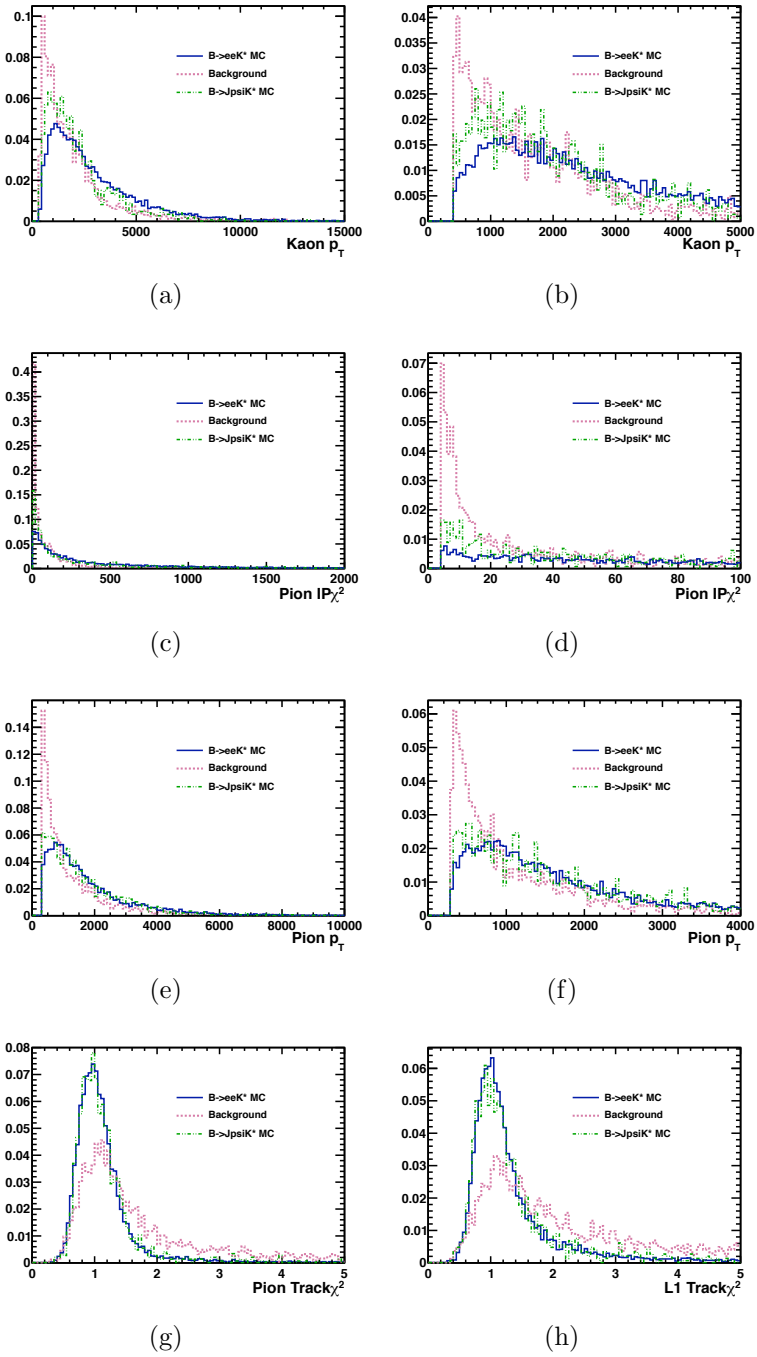

Figure B.4: The distributions of the variables used to train the BDT (cont).

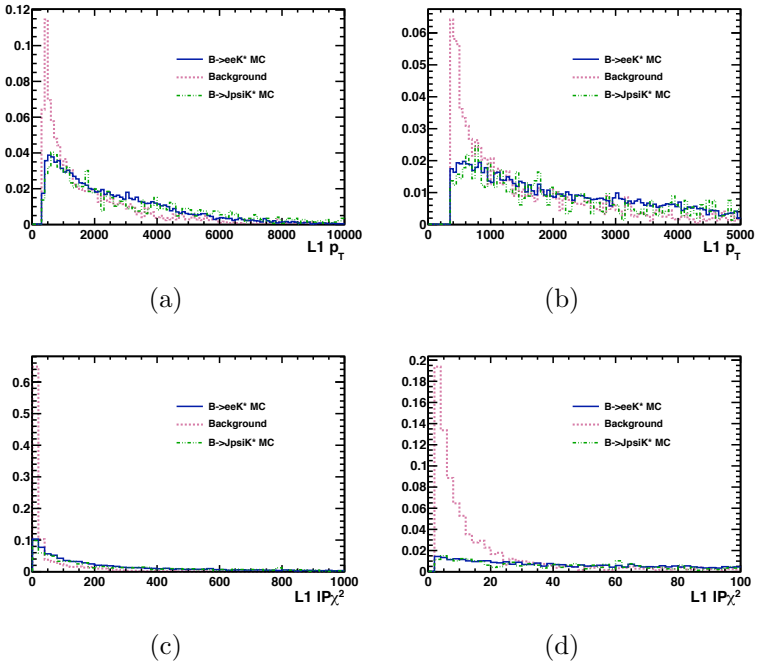

(a) (b)

(c) (d)

Figure B.5: The distributions of the variables used to train the BDT (cont).

Appendix C

Validation of the fitting procedure

In order to test the fitting procedure, toy Monte Carlo samples have been generated. The values used are based on those obtained from the fit to real data. The values are summarized in Table C. In order to check the quality of the fits, for each toy Monte Carlo sample and each fitted variable, the pull distribution of a given parameter x, defined as the distribution of the quantity $P_x = \frac{x_{Fit} - x_{Gen}}{\sigma_x}$, as well as the fitted value and its uncertainty, are plotted. A total of 10000 toy samples have been generated. For well behaved fits, one expects that the distribution of P_x (pull distribution) follows a standard Gaussian distribution.

Trigger category	Nsig	Ncomb	comb slope
L0Ele	29	66	-0.00302442
L0Had	6	33	-0.00257742
L0TIS	11	76	-0.00270401

Table C.1: The values of the parameters used to generate toy MC.

In all categories, the extracted signal yields do not show any biases (refer to Figures C.1-C.3. For the combinatorial parameters, there is an interplay between the extracted value of the slope and the combinatorial yield. Performing the same toys study with ten times more statistics, the effect disappears and is thus attributed to the low statistics regime.

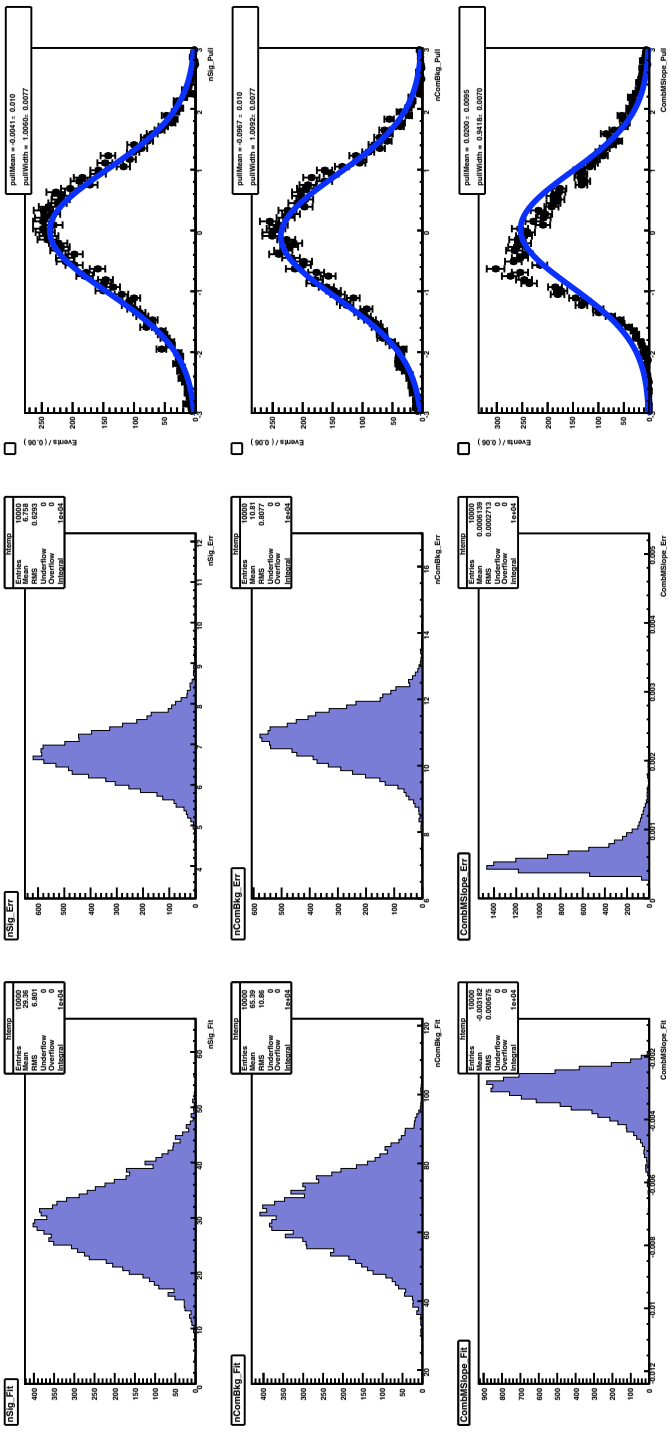

Figure C.1: Results from 10000 toy MC studies for the L0ElectronTOS category.

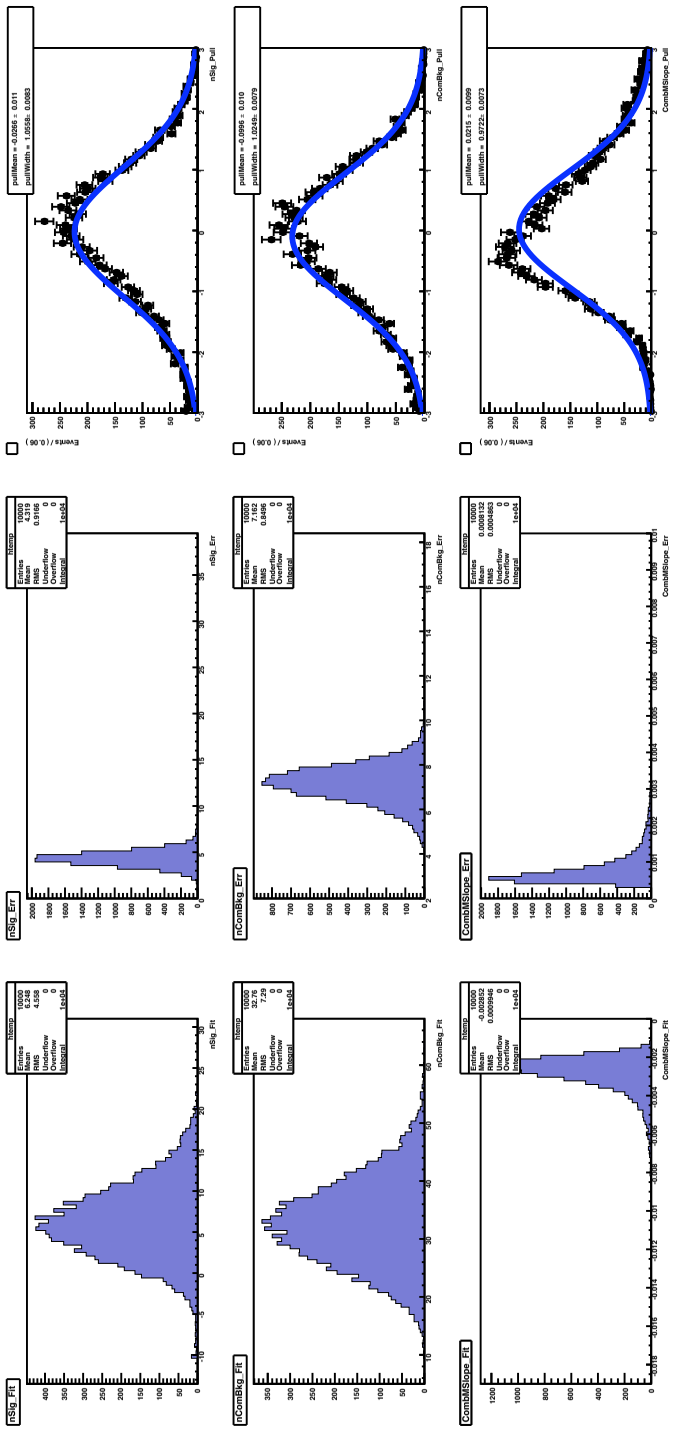

Figure C.2: Results from 10000 toy MC studies for the L0HadronTOS category.

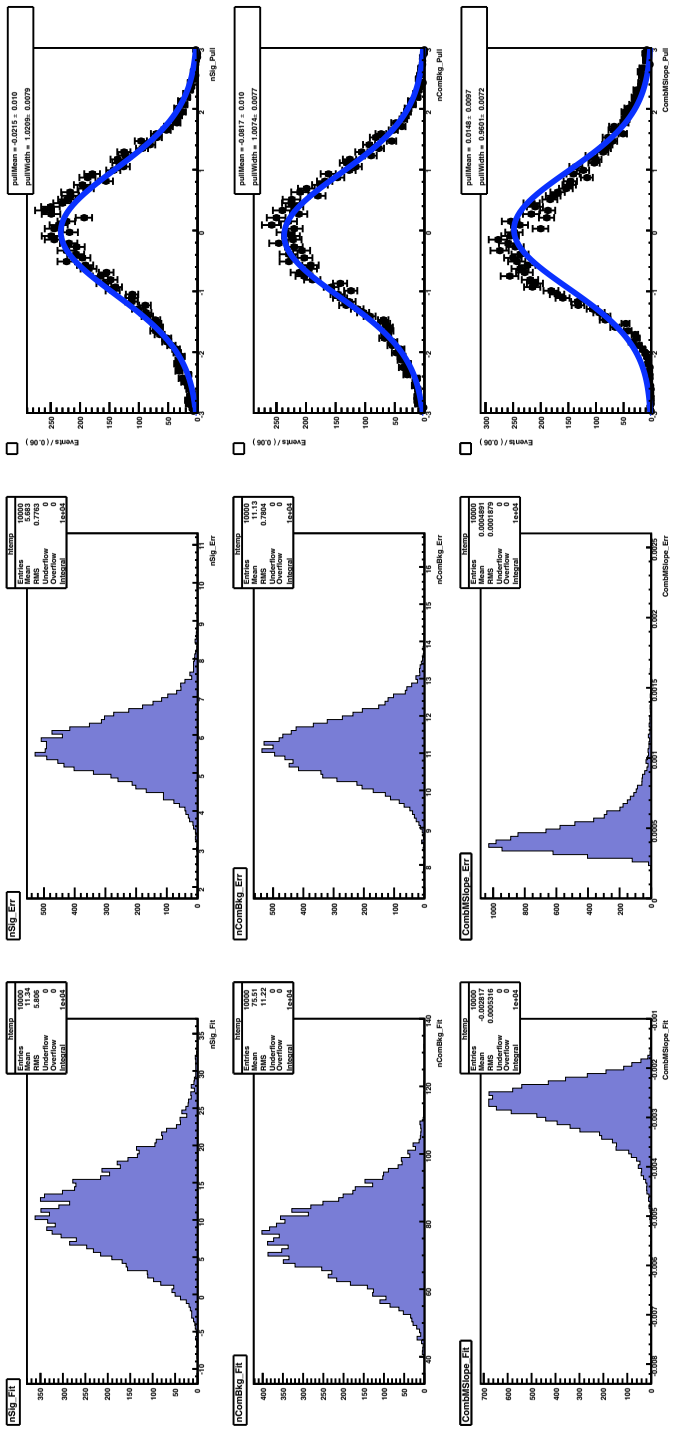

Figure C.3: Results from 10000 toy MC studies for the L0TIS category.

Bibliography

[1] A. Aaboe, *Scientific astronomy in antiquity*, Philosophical Transactions of the Royal Society of London. Series A, Mathematical and Physical Sciences **276** (1974), no. 1257 21. 23

[2] H. Flacher *et al.*, *Revisiting the Global Electroweak Fit of the Standard Model and Beyond with Gfitter*, Eur. Phys. J. **C60** (2009) 543, arXiv:0811.0009. 25

[3] ALEPH, CDF, D0, DELPHI, L3, OPAL, SLD Collaborations, the LEP Electroweak Working Group, the Tevatron Electroweak Working Group, and the SLD electroweak and heavy flavour groups, *Precision electroweak measurements and constraints on the Standard Model*, FERMILAB-TM-2480-PPD, CERN-PH-EP-2010-095, SLAC-PUB-14301. 25

[4] B. Pontecorvo, *Neutrino Experiments and the Problem of Conservation of Leptonic Charge*, Sov. Phys. JETP **26** (1968) 984. 25

[5] Super-Kamiokande Collaboration, Y. Ashie *et al.*, *Evidence for an oscillatory signature in atmospheric neutrino oscillation*, Phys. Rev. Lett. **93** (2004) 101801, arXiv:hep-ex/0404034. 25

[6] M. Y. Han and Y. Nambu, *Three-triplet model with double* SU(3) *symmetry*, Phys. Rev. **139** (1965) B1006. 26

[7] S. Glashow, J. Iliopoulos, and L. Maiani, *Weak Interactions with Lepton-Hadron Symmetry*, Phys. Rev. **D2** (1970) 1285; S. Weinberg, *A Model of Leptons*, Phys. Rev. Lett. **19** (1967) 1264. 26, 35

[8] P. W. Higgs, *Spontaneous Symmetry Breakdown without Massless Bosons*, Phys. Rev. **145** (1966) 1156. 27

[9] ATLAS Collaboration, G. Aad *et al.*, *Observation of a new particle in the search for the Standard Model Higgs boson with the ATLAS detector at the LHC*, Phys. Lett. **B716** (2012) 1, arXiv:1207.7214. 27

[10] CMS Collaboration, S. Chatrchyan *et al.*, *Observation of a new boson at a mass of 125 GeV with the CMS experiment at the LHC*, Phys. Lett. **B716** (2012) 30, arXiv:1207.7235. 27

[11] C. N. Yang and R. L. Mills, *Conservation of isotopic spin and isotopic gauge invariance*, Phys. Rev. **96** (1954) 191. 27

[12] D. Gross and F. Wilczek, *Ultraviolet Behavior of Nonabelian Gauge Theories*, Phys. Rev. Lett. **30** (1973) 1343; H. D. Politzer, *Reliable Perturbative Results for Strong Interactions?*, Phys. Rev. Lett. **30** (1973) 1346. 29

[13] F. Englert and R. Brout, *Broken Symmetry and the Mass of Gauge Vector Mesons*, Phys. Rev. Lett. **13** (1964) 321. 30

[14] P. W. Higgs, *Broken symmetries, massless particles and gauge fields*, Phys. Lett. **12** (1964) 132.

[15] P. W. Higgs, *Broken Symmetries and the Masses of Gauge Bosons*, Phys. Rev. Lett. **13** (1964) 508.

[16] G. Guralnik, C. Hagen, and T. Kibble, *Global Conservation Laws and Massless Particles*, Phys. Rev. Lett. **13** (1964) 585.

[17] T. Kibble, *Symmetry breaking in nonAbelian gauge theories*, Phys. Rev. **155** (1967) 1554. 30

[18] E. Noether, *Invariant Variation Problems*, Gott. Nachr. **1918** (1918) 235, arXiv:physics/0503066. 30

[19] LHCb Collaboration, R. Aaij *et al.*, *Measurement of the CP-violating phase ϕ_s in the decay $B_s^0 \to J/\psi\phi$*, Phys. Rev. Lett. **108** (2012) 101803, arXiv:1112.3183. 32

[20] J. Charles *et al.*, *Predictions of selected flavour observables within the Standard Model*, Phys. Rev. **D84** (2011) 033005, arXiv:1106.4041. 32

[21] N. Cabibbo, *Unitary Symmetry and Leptonic Decays*, Phys. Rev. Lett. **10** (1963) 531. 32

[22] M. Kobayashi and T. Maskawa, *CP Violation in the Renormalizable Theory of Weak Interaction*, Prog. Theor. Phys. **49** (1973) 652. 33

[23] N. Cabibbo, *Unitary Symmetry and Leptonic Decays*, Phys. Rev. Lett. **10** (1963) 531. 33

[24] L. Wolfenstein, *Parametrization of the Kobayashi-Maskawa Matrix*, Phys. Rev. Lett. **51** (1983) 1945. 33

[25] Particle Data Group, K. Nakamura *et al.*, *Review of particle physics*, J. Phys. **G37** (2010) 075021. 33, 39, 80, 95, 148

[26] LHCb Collaboration, R. Aaij *et al.*, *Evidence for CP violation in time-integrated $D^0 \to h^-h^+$ decay rates*, Phys. Rev. Lett. **108** (2012) 111602, arXiv:1112.0938. 34

[27] CKMfitter Group, J. Charles *et al.*, *CP violation and the CKM matrix: Assessing the impact of the asymmetric B factories*, Eur. Phys. J. **C41** (2005) 1, arXiv:hep-ph/0406184. 34, 35

[28] M. Ciuchini *et al.*, *2000 CKM triangle analysis: A Critical review with updated experimental inputs and theoretical parameters*, JHEP **0107** (2001) 013, arXiv:hep-ph/0012308. 34, 35

[29] *A measurement of γ from a combination of $B^\pm \to Dh^\pm$ analyses*, LHCb-CONF-2012-032. 35

[30] F. Zwicky, *On the Masses of Nebulae and of Clusters of Nebulae*, Astrophys. J. **86** (1937) 217. 36

[31] A. Sakharov, *Violation of CP Invariance, c Asymmetry, and Baryon Asymmetry of the Universe*, Pisma Zh. Eksp. Teor. Fiz. **5** (1967) 32. 37

[32] M. Misiak *et al.*, *Estimate of $BR(\bar{B} \to X_s\gamma)$ at $O(\alpha_s^2)$*, Phys. Rev. Lett. **98** (2007) 022002, arXiv:hep-ph/0609232. 39

[33] E. Lunghi and J. Matias, *Huge right-handed current effects in $B \to K^{(*)}l^+l^-$ in supersymmetry*, JHEP **0704** (2007) 058, arXiv:hep-ph/0612166. 39

[34] Y. Grossman and D. Pirjol, *Extracting and using photon polarization information in radiative B decays*, JHEP **0006** (2000) 029, arXiv:hep-ph/0005069. 40, 79

[35] A. Tayduganov, *Electroweak radiative B-decays as a test of the Standard Model and beyond*, THESIS LAL-11-181. 41

[36] A. Pich, *Effective field theory: Course*, arXiv:hep-ph/9806303. 40

[37] A. J. Buras, *Weak Hamiltonian, CP violation and rare decays*, arXiv:hep-ph/9806471. 40

[38] F. Kruger and J. Matias, *Probing new physics via the transverse amplitudes of $B \to K^{(*)} l^+ l^-$ at large recoil*, Phys. Rev. **D71** (2005) 094009, arXiv:hep-ph/0502060. 41, 42, 43, 50

[39] M. Matsumori and A. Sanda, *The Mixing-induced CP asymmetry in $B \to K * \gamma$ decays with perturbative QCD approach*, Phys. Rev. **D73** (2006) 114022, arXiv:hep-ph/0512175. 42

[40] D. Becirevic, E. Kou, A. Le Yaouanc, and A. Tayduganov, *Future prospects for the determination of the Wilson coefficient $C'_{7\gamma}$*, JHEP **1208** (2012) 090, arXiv:1206.1502. 47, 50

[41] D. Becirevic and E. Schneider, *On transverse asymmetries in $B \to K^{(*)} l^+ l^-$*, Nucl. Phys. **B854** (2012) 321, arXiv:1106.3283. 48

[42] D. Atwood, M. Gronau, and A. Soni, *Mixing induced CP asymmetries in radiative B decays in and beyond the standard model*, Phys. Rev. Lett. **79** (1997) 185, arXiv:hep-ph/9704272. 50

[43] B. Grinstein, Y. Grossman, Z. Ligeti, and D. Pirjol, *The Photon polarization in $B \to X\gamma$ in the standard model*, Phys. Rev. **D71** (2005) 011504, arXiv:hep-ph/0412019. 51

[44] P. Ball and R. Zwicky, *Time-dependent CP Asymmetry in $B \to K^*\gamma$ as a (Quasi) Null Test of the Standard Model*, Phys. Lett. **B642** (2006) 478, arXiv:hep-ph/0609037. 51, 52

[45] D. Atwood, M. Gronau, and A. Soni, *Mixing induced CP asymmetries in radiative B decays in and beyond the standard model*, Phys. Rev. Lett. **79** (1997) 185, arXiv:hep-ph/9704272. 51

[46] M. Gronau, Y. Grossman, D. Pirjol, and A. Ryd, *Measuring the photon polarization in $B \to K\, pi\pi\gamma$*, Phys. Rev. Lett. **88** (2002) 051802, arXiv:hep-ph/0107254. 51, 53

[47] E. Kou, A. Le Yaouanc, and A. Tayduganov, *Determining the photon polarization of the $B \to s\gamma$ using the $B \to K_1(1270)\gamma$ decay*, Phys. Rev. **D83** (2011) 094007, arXiv:1011.6593. 51, 53

[48] Heavy Flavor Averaging Group, Y. Amhis *et al.*, *Averages of b-hadron, c-hadron, and tau-lepton properties as of early 2012*, arXiv:1207.1158. 52

[49] P. Ball, G. W. Jones, and R. Zwicky, *$B \to V\gamma$ beyond QCD factorisation*, Phys. Rev. **D75** (2007) 054004, arXiv:hep-ph/0612081. 52

[50] B. Meadows *et al.*, *The impact of SuperB on flavour physics*, arXiv:1109.5028. 52

[51] *The road map for the radiative decays of beauty hadrons at lhcb*, LHCB-ROADMAP4-001. 53

[52] F. Soomro, *Radiative Decays of B Hadrons at LHCb*, Conf. Proc. **C0908171** (2009) 557. 53

[53] LHCb collaboration, R. Aaij *et al.*, *Measurement of $\sigma(pp \to b\bar{b}X)$ at $\sqrt{s} = 7$ TeV in the forward region*, Phys. Lett. **B694** (2010) 209, arXiv:1009.2731. 56

[54] S. Erhan, M. Medinnis, P. Schlein, and J. Zweizig, *COBEX: A Dedicated collider B experiment*, Nucl. Instrum. Meth. **A333** (1993) 101. 56

[55] Y. Lemoigne, *GAJET: A CP violation gas jet experiment for the CERN LHC*, Nucl. Instrum. Meth. **A333** (1993) 113. 56

[56] F. Costantini, *LHB: A Fixed target experiment at LHC to measure CP violation in B mesons*, Nucl. Instrum. Meth. **A333** (1993) 125. 56

[57] LHC-B Collaboration, *LHC-B: A dedicated LHC collider beauty experiment for precision measurements of CP-violation. Letter of intent*, CERN-LHCC-95-05. 56

[58] LHCb Collaboration, S. Amato *et al.*, *LHCb technical proposal*, CERN-LHCC-98-04, CERN-LHCC-P-4. 56

[59] LHCb collaboration, A. A. Alves Jr. *et al.*, *The LHCb detector at the LHC*, JINST **3** (2008) S08005. 57, 59

[60] V. Breton, N. Brun, and P. Perret, *A clustering algorithm for the LHCb electromagnetic calorimeter using a cellular automaton*, LHCb-2001-123, CERN-LHCb-2001-123. 73

[61] H. Terrier and I. Belyaev, *Particle identification with lhcb calorimeters*, Tech. Rep. LHCb-2003-092, CERN, Geneva, Sep, 2003. 73, 74

[62] E. P. Olloqui and the LHCb Collaboration, *Lhcb preshower(ps) and scintillating pad detector (spd): Commissioning, calibration, and monitoring*, Journal of Physics: Conference Series **160** (2009), no. 1 012046. 74

[63] M. Williams *et al.*, *The HLT2 topological lines*, LHCb-PUB-2011-002. 77

[64] BABAR Collaboration, J. Lees *et al.*, *Measurement of Branching Fractions and Rate Asymmetries in the Rare Decays* $B \to K^{(*)} l^+ l^-$, Phys. Rev. **D86** (2012) 032012, arXiv:1204.3933. 79

[65] BELLE Collaboration, J.-T. Wei *et al.*, *Measurement of the Differential Branching Fraction and Forward-Backward Asymmetry for* $B \to K^{(*)} l^+ l^-$, Phys. Rev. Lett. **103** (2009) 171801, arXiv:0904.0770. 79

[66] *LHCb Collaboration, The DaVinci Project*, http://lhcb-release-area.web.cern.ch/LHCb-release-area/DOC/davinci/.l. 82

[67] A. Ali, P. Ball, L. Handoko, and G. Hiller, *A Comparative study of the decays* $B \to K^{(*)} l^+ l^-$ *in standard model and supersymmetric theories*, Phys. Rev. **D61** (2000) 074024, arXiv:hep-ph/9910221. 82

[68] P. Ball and R. Zwicky, *New results on* $B \to \pi, K, \eta-$ *decay formfactors from light-cone sum rules*, Phys. Rev. **D71** (2005) 014015, arXiv:hep-ph/0406232. 82

[69] LHCb Collaboration, R. "Aaij and others", *Measurement of charged particle multiplicities in pp collisions at $\sqrt{s}$ =7TeV in the forward region*, The European Physical Journal C **72** (2012) 1. 82

[70] J. Lefrançois and M. Schune, *Measuring the photon polarization in $b \to s\gamma$ using the $B^0 \to K^{*0}e^+e^-$ decay channel*, LHCb-PUB-2009-008. 85, 89

[71] J. R. Quinlan, *Simplifying decision trees*, Int. J. Man-Mach. Stud. **27** (1987) 221. 85

[72] M. Needham, *Clone track identification using the kullback-liebler distance*, Tech. Rep. LHCb-2008-002. CERN-LHCb-2008-002. LPHE-2008-002, CERN, Geneva, Jan, 2008. 86

[73] A. Hoecker *et al.*, *TMVA: Toolkit for Multivariate Data Analysis*, PoS **ACAT** (2007) 040, arXiv:physics/0703039. 89

[74] P. M. and D. F.R., *SPlot: A statistical tool to unfold data distributions.*, Nucl. Instrum. Meth. **A555** (2005) 356. 90, 131, 141

[75] LHCb Collaboration, *LHCb technical design report: Reoptimized detector design and performance*, CERN-LHCC-2003-030. 93

[76] R. H. Dalitz, *On an alternative decay process for the neutral -meson*, Proceedings of the Physical Society. Section A **64** (1951), no. 7 667. 99

[77] O. Deschamps and A. Puig Navarro, *Measurement of the ratio of branching fractions $B(B^0 \to K^{*0}\gamma)/B(B_s^0 \to \phi\gamma)$ and direct CP violation in $B^0 \to K^{*0}\gamma$*, LHCb-CONF-2012-004. 102

[78] A. Powell, *talk at the LHCb UK meeting, Imperial College, Thursday 6th January 2011* , Internal note in preparation. 104, 131

[79] T. Skwarnicki, *A study of the radiative CASCADE transitions between the Upsilon-Prime and Upsilon resonances*, DESY-F31-86-02. 106

[80] W. Verkerke and D. P. Kirkby, *The RooFit toolkit for data modeling*, eConf **C0303241** (2003) MOLT007, arXiv:physics/0306116. 107

[81] LHCb Collaboration, R. Aaij *et al.*, *Measurement of the ratio of branching fractions $BR(B^0 \to K^{*0}\gamma)/BR(B^0_s \to \phi\gamma)$ and the direct CP asymmetry in $(B^0 \to K^{*0}\gamma$*, Nucl. Phys. **B867** (2013) 1, arXiv:1209.0313. 108

[82] M. Clemencic *et al.*, *The LHCb Simulation Application, Gauss: Design, Evolution and Experience*, J. of Phys: Conf. Ser. **331** (2011) 032023. 126, 156

[83] A. Martin Sanchez, P. Robbe, and M.-H. Schune, *Performances of the lhcb l0 calorimeter trigger*, Tech. Rep. LHCb-PUB-2011-026. CERN-LHCb-PUB-2011-026, CERN, Geneva, Jun, 2012. 127

[84] *LHCb MC11 generator and simulation statistics*, http://lhcb-release-area.web.cern.ch/LHCb-release-area/DOC/STATISTICS/MC11STAT/index.shtml. 156

[85] T. Sjöstrand, S. Mrenna, and P. Skands, *PYTHIA 6.4 Physics and manual*, JHEP **05** (2006) 026, arXiv:hep-ph/0603175. 156

[86] I. Belyaev *et al.*, *Handling of the generation of primary events in* Gauss*, the LHCb simulation framework*, Nuclear Science Symposium Conference Record (NSS/MIC) **IEEE** (2010) 1155. 156

[87] D. J. Lange, *The EvtGen particle decay simulation package*, Nucl. Instrum. Meth. **A462** (2001) 152. 156

[88] E. Barberio, B. van Eijk, and Z. Was, *PHOTOS: A Universal Monte Carlo for QED radiative corrections in decays*, Comput. Phys. Commun. **66** (1991) 115. 156

[89] GEANT4 collaboration, S. Agostinelli *et al.*, *GEANT4: A simulation toolkit*, Nucl. Instrum. Meth. **A506** (2003) 250. 156

[90] *LHCb Collaboration, The Boole Project*, http://lhcb-release-area.web.cern.ch/LHCb-release-area/DOC/boole/. 156

[91] *LHCb Collaboration, The Moore Project*, http://lhcb-release-area.web.cern.ch/LHCb-release-area/DOC/moore/. 156

[92] *LHCb Collaboration, The Brunel Project* , http://lhcb-release-area.web.cern.ch/LHCb-release-area/DOC/brunel/. 156

Acknowledgements

On arrival, three years seemed like a long time to carry out the work for a thesis, but it's flown by before I realised. It's no secret that it's not been the easiest time of my life, but the whole experience has been invaluable in growing me professionally and personally. And there are many people to thank for this.

I should start by thanking Achille Stocchi and everyone at LAL for offering me the chance to undertake my thesis here, and to the administrative staff for their patience, especially in the beginning with my bad french!

Thank you to Damir Bečirević, and Ulrik Egede for agreeing to be jury members, and to the referees, Phillip Urquijo and Olivier Deschamps, for accepting the task of reading my thesis. The extensive list of suggestions made are particularly useful in making the thesis more readable in general, but especially to someone from outside of LHCb, and I very much appreciate the effort in providing such a detailed list of comments.

Many thanks to Marie-Hélène Schune for inviting me to come for my thesis in the beginning, for her help in obtaining the grant. Over the past three years, I've seen she would have made an excellent lawyer, from the way she has argued the case for poor $B^0 \to K^{*0} e^+ e^-$, and I'm immensely grateful that in the end we could make the measurement. Thanks for your guidance and patience, especially in the last few months, which I know were not easy.

To all the LHCb group in Orsay, thank you for the pleasant working environment and lunch times (which were enjoyable despite the food!) To my fellow K*ee colleagues, Jibo and Jacques, it has been a pleasure to work with you both. Jibo, I'm not sure what I would have done without both, your insights, and technical know-how. The group will miss you! Jacques, I am very grateful to work on the same analysis as you and to have had you next door. Thank you for always being ready to discuss. I'm sure I would have said many more stupid things in my thesis and at meetings if it weren't for your careful attention and ideas. Thanks also to

Patrick Robbe for his help in reading over part of the thesis, and for the excuse to practice piano again. Many thanks to your family for inviting me into your home on several occasions, and for wonderful food and win. And to Yasmine, thanks for your encouragement (and tea and cd).

Many thanks also to the LHCb group in Glasgow, for arousing my interest in particle physics in the first place, and giving me the opportunity to go to CERN. A special thank you to Vava Gligorov, who was always ready to answer all my stupid questions but also challenged me to work things out for myself. You helped me with too many things over the years to thank you for here, but by letting me work hard in Glasgow, you made a difficult time a lot easier for me than it could have otherwise been.

To the students, past and present of building 208, thank you for the fun times, mainly around caffeine or alcohol based beverages. Aurélien, thanks for persevering in trying to talk to me, eventually we could more or less understand each others accents. Thanks for trying to teach me of french things, but even after two lessons at the blackboard, I still don't get the education system. Hope to have more beer (and dancing???) in the future. Andrey, my fellow parisian!;) Thanks for rescuing me when I was locked out of my apartment, for all the beers, and eh, carrying me home. Leonid, thanks for teaching me piano, and for staying when everyone else left! sorry to leave you now, the last of the wednesday vodka club. I'll miss your oddness. Dennis, thanks for the offer of borrowing your camp bed for the office at CERN! :P Wenbin, I miss your chinese jokes! Thanks for listening to my thesis woes, and for lunches at CERN! Nejc, thanks for the beers, the flowers, and for the times you've stayed out longer than the others! And big thanks for the help with the stupid window. I would still be freezing if it weren't for you. Alexandra, thanks for PARTY LAMP, yayitas, and reminding me where the gear stick is when necessary. Good luck for this year, remember to have a little bit of fun occasionally too. Olga, thanks for the driving stories, and congratulations on being the only person I know of that passed first time in france! Maksym, thanks for for putting up with the mess on my side of the office! Alexis, thanks for making the effort in trying to make me speak french, and for being on my list, and for being generally hilarious whether you mean to be or not. Please consider a career as a TV comedian in the UK. And to my wifey. Thanks for managing to be a proper oddball despite the environment. Politics over a bottle of wine and pizza nights made the past few months a lot better than they would have been without you. I'll reserve the roof terrace and a set of

bunny ears for you when you come to amsterdam :P And I hereby hand over the K*ee baton to you. Good luck with it.

And moving out of LAL, to my other friends in France. Big thanks to my family at Trinity and Catalyst. It's hard with such a big turn over rate, but the right people always seem to be there at the right time. You even manged to persuade me that I might want to stay in Paris at some point. Special thanks to Sandra and Jennie for a super summer with wine, broken glasses and Italians. Also, thanks to 'Mary Macleod' for being a geek and inviting me to my only french gatherings not full of physicists, (and thanks to Callum for introducing us, and being a muppet.) Diego, thanks for all the amazing memories, and making my time in France a lot happier.

Finally, huge thanks to every single person that came to visit me whilst I lived here. Your love and support (and supplies from home) have really kept me going. Prize for number one visitor goes to Suzanne (accompanied if we were lucky, by Shelby). Some of my best Paris memories are with you, including Jardin Luxembourg shenanigans, filming with Leonid and Andrey, and dancing with Aurélien. Also to Amy and Peter who joined us for Disney adventures, and brie and ham, and Ruth and Alex for general awesomeness and for not forgetting me even though I don't get to see you all as often as I would like. Also high up in the return visits list are Jenni and Struan. You two make clothes shopping fun. Miss you both a lot. And Struan, at least the time when you locked us out is now a funny story. To my old flatmates, Helen, Beth and Dish, it was lovely to see you all here too, and always a pleasure and encouragement to see you in Scotland. To the guys (and Julie!) from Glasgow University physics days. Well done for managing to be organised enough to come see me twice. Physics is definitely not as much fun without you. Halfers, thanks for passing on your form knowledge, and don't think you can disappear from my life by going off to Australia. James, thanks for being fat, and for letting me crash at your pig sty when in Glasgow. No thanks for distractions. Matt, thanks for entertaining me in Goven! I actually had fun. Jules and Dave, its long past time for some cocktails and a gossip. Special thanks to Joni. I was reading in proverbs about the type of friends good for us, and you're one of those good eggs. Despite all our nonsense, you totally inspire and encourage me. Keep wrestling. To VIG, thanks for being you. Special thanks to my sister, Elena for providing superb holiday weekends in Valencia, Meike for hosting us in Berlin, Ariana for hugs and having us this year, and of course Jeroen, for providing a home away from home and

the best meals I've ever had. I don't know how I would have got through the past three years without you. And Erwin, you've kept me smiling these last few months and gave me something to look forward to. I can't imagine how I would have coped without that, and I can't wait till next year.

And to my family, and in particular to my mother. Thanks for putting up with me and all my silly notions,(going to Cameroon, Colombia, France...) without complaint. Its only possible for me because I know I have your love and support, and you are always there, even if you moan when I call because no matter what time it is, it's in the middle of Grey's Anatomy/X Factor/America's Next Top Model etc. I don't really have the words to thank you properly, but you made me who I am today. I hope you enjoyed your party.

To those I've forgotten, woopsadaisy. You can give me a hard time later, please accept my apologies. Indeed, this thesis was supported by many people, some mentioned above, and others not. Many thanks to all of you.